Geochronology and bulk sediment geochemistry of the Late Cretaceous maar lake sedimentary fill of the Wombat kimberlite pipe, subarctic Canada

by

Serhiy Dmytrovy Buryak

A thesis submitted in partial fulfillment of the requirements for the degree of

Master of Science

Department of Earth and Atmospheric Sciences

University of Alberta

ABSTRACT

The Wombat pipe (64.918° N, 110.447° W) is a diamondiferous kimberlite in the Lac de Gras kimberlite field of Northwest Territories, Canada. Two drill cores, CH93-29 and 00-05, intersect the Wombat crater facies and include 195 m of well preserved, undisturbed lake sediment fill. Bulk sediment elemental analysis, C isotope composition, and Rock-Eval pyrolysis together with inferences from microfossils, are used to characterize conditions of sedimentation and paleoenvironmental variability in the maar lake.

Bulk sediment C/N, hydrogen index (HI), and $\delta^{13}C$ indicate material derived from C_3 land plants dominates the sedimentary organic matter, with a possible minor algal contribution. The $\delta^{13}C$ values range from -25.3 ‰ to -30.2 ‰ and C/N ratios vary between 14.6 and 38.4, recording the shifts in the proportions of land-derived material and algal organic matter as climate conditions fluctuated. Eighteen samples analyzed by Rock-Eval pyrolysis all plot in the Type III kerogen field for HI vs. Tmax, with average Tmax values ~425 °C indicative of the low thermal maturity of organic matter. Total organic carbon (TOC) averages 3.6 wt% and average total carbonate content is 14.1 wt%, indicating bottom water anoxia and substantial carbonate input from weathering of overlying carbonate cover rocks, respectively. Together with well-preserved freshwater microfossils (e.g. diatoms, chrysophytes, synurophytes), the results indicate deposition in a non-marine setting, likely during a period of regression of the Western Interior Seaway. The age of the Wombat maar lake sediments is determined using MC-LA-ICP-MS U-Pb zircon geochronology from two distal rhyolitic tephra beds found in the core 00-05, yielding a date of 82.36 ± 0.44 Ma (n = 18/34, MSWD = 1.51). This minimum age suggests that Wombat kimberlite pipe emplacement occurred during the Late Cretaceous, with sedimentation in the maar beginning shortly thereafter. The major and trace element geochemical analysis of the tephra glasses allows to make inferences about the type and the spread of the Late Cretaceous volcanism in subarctic Canada. The findings from the Wombat pipe post-eruptive maar lake sediment fill provide direct evidence for a non-marine environment in the Lac de Gras area during the Late Cretaceous. Furthermore, microfossils in the Wombat pipe sediment fill likely include the oldest-known occurrence of freshwater diatoms.

PREFACE

This thesis is a collaborative work by Serhiy Buryak and faculty at the Department of Earth and Atmospheric Sciences, University of Alberta, Canada, identified below. The Wombat core CH93-29 samples were collected by Dr. Alberto Reyes and Dr. Peter Siver at Connecticut College (New London, USA) and samples from core 00-05 were collected by Serhiy Buryak and Dr. Alberto Reyes at the Northwest Territories Geological Survey core archive (Yellowknife, Canada). The tephra geochemical data were collected together with Dr. Britta Jensen; Rock-Eval/LECO data were obtained from a commercial vendor (GeoMark Research, USA).

The rest of the data analysis, literature review, and interpretations are my original work with the guidance from Dr. Alberto Reyes and others. This thesis includes an introductory review chapter on the current state of the maar lake research, followed by a main thesis chapter which is in preparation for submission to a peer-reviewed journal.

ACKNOWLEDGEMENTS

Firstly, I would like to thank Dr. Alberto Reyes for his guidance, support and patience throughout the duration of this project. His insightful comments and suggestions were most helpful throughout the entire research period and during writing of this thesis.

Secondly, I would like to thank the faculty at the University of Alberta, Dr. Britta Jensen, Dr. Yan Luo, Dr. Long Li, Dr. Andrew DuFrane, Dr. Graham Pearson and Dr. Nicholas Harris, for insightful comments and support during difficult months of research. I also would like to extend my thanks to Dr. Peter Siver from Connecticut College, New London, USA for his vast contributions on the study of the Wombat microfossils.

Lastly, I would like to thank my family and friends for being supportive throughout my time in a graduate program.

I am also grateful to Dominion Diamond Mines ULC and Northwest Territories Geological Survey (Barrett Elliott and Scott Cairns) for access to exploration drill cores from the Wombat and other kimberlite localities.

The research was funded by an NSERC Discovery Grant and Northern Research Supplement (Reyes), the Canada Excellence Research Chairs program (Pearson), and NSF Division of Environmental Biology award 1144098 (Siver).

TABLE OF CONTENTS

LIST OF TABLES

LIST OF FIGURES

CHAPTER 1: INTRODUCTION

1.1 BACKGROUND

Since the 1991 discovery of the Lac de Gras kimberlite field on the Slave Craton of Northwest Territories, more than 270 confirmed kimberlites have been found in the region (Fig 1.1). The existing geochronology, based largely on U-Pb and Rb-Sr dating of mineral phases associated with kimberlite emplacement, indicates that most of them were emplaced in several intervals spanning a period between 75–45 Ma (Creaser et al., 2004; Sarkar et al., 2015). Though the Slave Craton is largely devoid of Phanerozoic sediment cover (Nowicki et al., 2004), abundant sedimentary xenoliths (e.g. Sweet et al., 2003) hosted in the kimberlite diatreme provide glimpses of the now eroded cratonic sedimentary cover and associated depositional environments prior to kimberlite emplacement. In rare cases, kimberlite emplacement was followed by development and sedimentary infilling of maar lakes in the kimberlite diatreme (e.g. Hamblin et al., 2003). These maar lake fills, which provide continuous, well-preserved sedimentary sequences from which paleoclimate and paleoenvironments can be inferred, are the subject of this thesis.

1.2 KIMBERLITES IN THE LAC DE GRAS REGION

The Lac de Gras kimberlite field is located in the central part of the Canadian Shield within the Archean Slave craton (Kjarsgaard, 2001) and includes more than 270 confirmed kimberlites. Kimberlites in the Lac de Gras field are characterized by a small (150–250 m diameter), steep-sided, irregularly shaped diatreme morphologies. The majority of kimberlites have surface areas < 5 Ha at the top of the diatreme, with several larger exceptions up to ca. 20 Ha (e.g. Wombat, Fox kimberlites), and can extend to great depths below the surface (400–600 m) (Pell, 1997). Periods of kimberlite magmatism in the Lac de Gras are thought to fall into five major intervals centered on 48, 54, 61, 66, and 72 Ma (Sarkar et al., 2015). Older, pre-Cenozoic kimberlites are rare in the Lac de Gras field (e.g. the Carboniferous Eddie kimberlite), but since many of the Lac de Gras kimberlites remain undated it is possible that other older pipes exist (Sarkar et al., 2015).

The suggested eruption mechanisms for kimberlite emplacement involve explosive devolatilization of CO_2-rich kimberlite magma coupled with phreatomagmatism, leading to excavation and expulsion of host rock, in turn fragmenting the magma, country rock and overlying cover in the process (Nowicki et al., 2004). The open crater then probably gets infilled directly by the deposition of the eruption column and/or resedimentation of the crater rim material. The pipe diatreme morphologies are controlled by near-surface structures (faults, joints) as well as by the thickness of the cover rocks and competence of the country rock at the time of the eruption (Field and Scott Smith, 1998; Nowicki et al., 2004).

The crater fill facies in Lac de Gras kimberlites is unique compared to counterparts in South Africa or Siberia. Lac de Gras crater fill successions are dominated by pyroclastic, volcaniclastic and resedimented volcaniclastic kimberlite rather than primary and hypabyssal volcanics (Carlson et al., 1998). In addition, the Lac de Gras kimberlite crater facies are known to include abundant sedimentary xenoliths of now-eroded cover rocks (e.g. Cookenboo et al., 1998) and contemporaneous wood megafossils entombed at time of emplacement (Wolfe et al., 2012). Rarely, Lac de Gras kimberlites may also host sediments that infilled a post-emplacement diatreme maar lake (e.g. Giraffe, Wombat kimberlites) (Nassichuk and Dyke, 1998; Hamblin et al., 2003; Sweet et al., 2003; Siver et al., 2016; Wolfe et al., 2017).

1.3 MAAR LAKES AS PALEOENVIRONMENTAL ARCHIVES

Maars are typically monogenetic volcanic craters formed by an explosive eruption that cut into the country rock and comprise the pyroclastic (tuff) rim, the crater infill sediments, the diatreme, and the feeder dyke system (Büchel, 1993). Most maars are typical collapse craters resulting from an explosive ejection of the host rock, but the exact formation mechanism may depend on the type of volcanism (e.g. caldera volcano, kimberlite) and is not universal for all localities. The maar crater usually creates a topographic depression that undercuts the groundwater level leading to the formation of a lake. The lake is then filled by marginal and profundal sediments. There are four primary sources of the infilling sediment and organic matter in maars (Büchel, 1993): marginal mass movement and flows; allochthonous deposits from discharging streams and creeks; direct atmospheric or aeolian deposition; and autochthonous production of organic matter, carbonates, and silica within the lake. Importantly, the character of the infilling sediment is strongly dependant on the paleoclimatic conditions at the time of sedimentation. Maar lakes are known to be excellent high resolution paleoenvironmental archives often due to deep water anoxia facilitating good preservation of organic matter (e.g. Herendeen and Jacobs, 2000; Pirrung et al., 2003).

Maar lake fills are thought to be rare in the Lac de Gras kimberlite field. The most prominent example is the Giraffe kimberlite diatreme, which hosted a small, low-energy maar lake deposited during the warm, temperate, humid climate of the middle Eocene (Hamblin et al., 2003; Wolfe et al., 2017). The sediment kerogen type and abundant preserved land plant detritus indicate deposition from a terrestrial environment (Hamblin et al., 2003). Studies of the >50 m-thick lake sediment succession have inferred paleoclimatic variation (temperature, precipitation, atmospheric CO_2 concentrations) during part of the early Cenozoic "greenhouse" in subarctic Canada (Wolfe et al., 2017), as well as characterization of early freshwater diatoms (e.g. Wolfe and Siver, 2009).

Some of the best-known maar localities are found in the Cenozoic Central European Volcanic Province, including the Eckfeld, Messel, and Enspel maars, providing an interpretative framework for the Lac de Gras maars (Pirrung et al., 2001). For example, the Eckfeld maar hosts ~100 m of middle Eocene lake sediment deposited in a subtropical climate and is similar in many aspects to the succession recovered from the Giraffe maar. The maar fill includes a shallowing upward succession of laminated bituminous shales and siltstones capped with a final gyttja and peat (Sabel et al., 2005). Similarly, the annually laminated oil shale from the middle Eocene (ca. 48 Ma) Messel maar provides important paleoenvironmental and paleontological data. In particular, Messel maar sediments record unique information about the early stages of mammalian evolution from exceptionally well-preserved mammal fossils, ranging from fully articulated skeletons to stomach contents (Meyer, 1994).

Numerous other examples can be drawn from other localities around the world such as the Late Cretaceous maar in Bushmanland, South Africa (Smith, 1986), the middle Eocene Mahenge kimberlite maar in Tazannia (Herendeen and Jacobs, 2000), and late Quaternary maars on the Seward Peninsula in Alaska (Colinvaux, 1964). All share the key feature of excellently persevered sedimentary and fossil records, due to confined catchments and bottom water anoxia which result in unusually high preservation potential of the sediment organic matter.

1.4 MULTIDISCIPLINARY APPROACH TO THE CHARACTERIZATION OF MAAR LAKE SEDIMENTS

Given the strong preservation potential of sediment organic matter in maar lakes, the physical, chemical and biological characterization of lake sediments can produce highly resolved data for the interpretation of environmental change at various time scales (Frey, 1998; Williamson et al., 2009), assuming that the sediment record is constrained by reliable chronology. This can be particularly difficult for pre-Quaternary lacustrine sequences outside the limit of ^{14}C techniques (ca. 45,000 years before present). Biostratigraphy and stratigraphic palynology can be a powerful dating tools for such lacustrine sequences if age-diagnostic fossils can be found but can only provide a non-numerical age estimate. Additionally, recycling of palynomorphs, differential preservation, and misidentification can distort the record. Radiometric dating techniques (U-Pb, U-series, Ar-Ar, K-Ar etc.) can be used to achieve reliable geochronological constraints for the lake sediments. In the case of maar lakes, the lake forms shortly after the eruption, making it possible to estimate maximum ages of lacustrine fills by dating the primary volcanic rocks. However, in the case of kimberlite maars it can be problematic to obtain necessary accessory minerals (e.g. perovskite, phlogopite, rutile, baddeleyite) due to the difficulty finding primary kimberlite samples and the rarity of the suitable mineral phases.

Alternatively, distal tephra deposits can be used to determine a direct age for maar lake sediment deposition. In current usage, tephra is a distally derived mixture of volcanic glass with a minor mineral component (< 10 % of total volume), where the accessory mineral phases (e.g. zircon, apatite, sanidine, titanite) can be dated using radiometric techniques. U-Pb zircon dating provides an approximate timing for the volcanic eruption associated with a tephra deposit. However, this approach can be challenging due to uncertainty in the disparity between zircon crystallization and "true" volcanic eruption ages, as well as possibility of inheritance of older xenocrystic/antecrystic grains. Additionally, trace and major element geochemical characterization of the tephra glasses is particularly informative in identifying the sources of volcanic activity, the type and the extent of volcanism in the region and can be useful for data reduction of mineral isotope composition for radiometric dating.

Carbon isotope composition and bulk sediment geochemical parameters are widely used in a paleoenvironmental studies. Rock-Eval pyrolysis indices, such as the hydrogen index (HI) and T_{max} (the temperature of maximum hydrocarbon release during pyrolysis), provide insight into the origin and thermal maturity, respectively, of the organic matter (Talbot and

Livingstone, 1989). Ratios of sediment organic C to total N (C_{org}:N_{tot}) are a proxy for estimating the proportions of autochthonous (aquatic) and allochthonous (land-derived) material. Carbon isotopic composition, expressed as the ratio of ^{13}C to ^{12}C in the sample relative to a standard ($\delta^{13}C$), provides insight into lake productivity, carbon recycling, and variations in the watershed vegetation due to climatic shifts. For example, during periods of higher autochthonous organic matter input and increased algal productivity, HI is typically elevated while C_{org}:N_{tot} is lowered (Meyers and Ishiwatari, 1993). The isotopic composition and C_{org}:N_{tot} ratios generally reflect the type of organic matter source, but interpretation is not straightforward because these proxies can be affected by diagenetic processes. For example, under anoxic conditions denitrification and carbon cycling may lead to increased bulk sediment C_{org}:N_{tot} and lower $\delta^{13}C$ (Hollander and Smith, 2001; Whiticar, 1999; Lehman et al., 2002). Under oxic bottom water conditions, decomposition of organic matter can lead to an increase in sediment $\delta^{13}C$ due to preferential loss of the light isotope ^{12}C, but no significant changes in C_{org}:N_{tot} is usually observed (Freudenthal et al., 2001; Lehman et al., 2002). Additionally, other modifications such as bioturbation and alteration of organic matter during sinking and at the lake bottom can modify the source character of organic matter (Talbot and Livingstone, 1989). Hence, by combining multiple geochemical proxies and geochronological age model of the sediment it is possible to extract a reliable paleoenvironmental data and make inferences about environmental conditionings during the maar infilling.

1.5 THESIS OBJECTIVES

The preceding discussion highlights the importance of both solid geochronology and a multiproxy approach to characterizing maar lake sediment fills in the Lac de Gras kimberlite field. To date, only the Giraffe pipe sediment fill has received any systematic attention from a geochronological and lake sediment paleoenvironments perspective.

In this thesis I focus on the post-eruptive maar lake fill of the Wombat kimberlite in the Lac de Gras field. Though the Wombat kimberlite pipe was first drilled in 1993, its maar lake fill initially received little attention (c.f. Nassichuk and Dyke, 1998). More recently, the Wombat kimberlite maar sediments have been studied for freshwater microfossils (e.g. Siver et al., 2016). However, there is little context for the microfossil studies from either geochronology or bulk sediment analysis. The only geochronological constraint comes from an unpublished pollen biostratigraphic age determination (Hu et al., 2011).

The overall aim of this study is thus to provide information about the age and paleoenvironment of the Wombat maar lake by applying a multimethod approach including tephra zircon U-Pb geochronology, and bulk sediment geochemical analysis.

The specific goals of this thesis are:

1. Establish a minimum age for the post-eruptive Wombat maar fill in order to build a chronological framework for paleoenvironmental interpretation and microfossil studies.

2. Explore the application of bulk sediment geochemical parameters as tools for the reconstruction of the depositional environment, organic matter characteristics, and paleogeography of the study area.

The results obtained through addressing these first two objectives led to two secondary objectives:

3. Investigate the application of the trace and major element geochemical characteristics of the tephra glass to provide an insight on the extend and type of the Late Cretaceous volcanism in subarctic Canada.
4. Broaden our knowledge of the paleogeography of the Western Interior Seaway in the Slave craton during the Late Cretaceous and propose an inferred stratigraphy for the Lac de Gras area during the Cretaceous and Paleogene.

The main body of the thesis is organized as a single manuscript intended for submission to a peer-reviewed journal. Detailed descriptions of methods and full tables of analytical results are presented in appendices.

1.6 CHAPTER 1 FIGURES

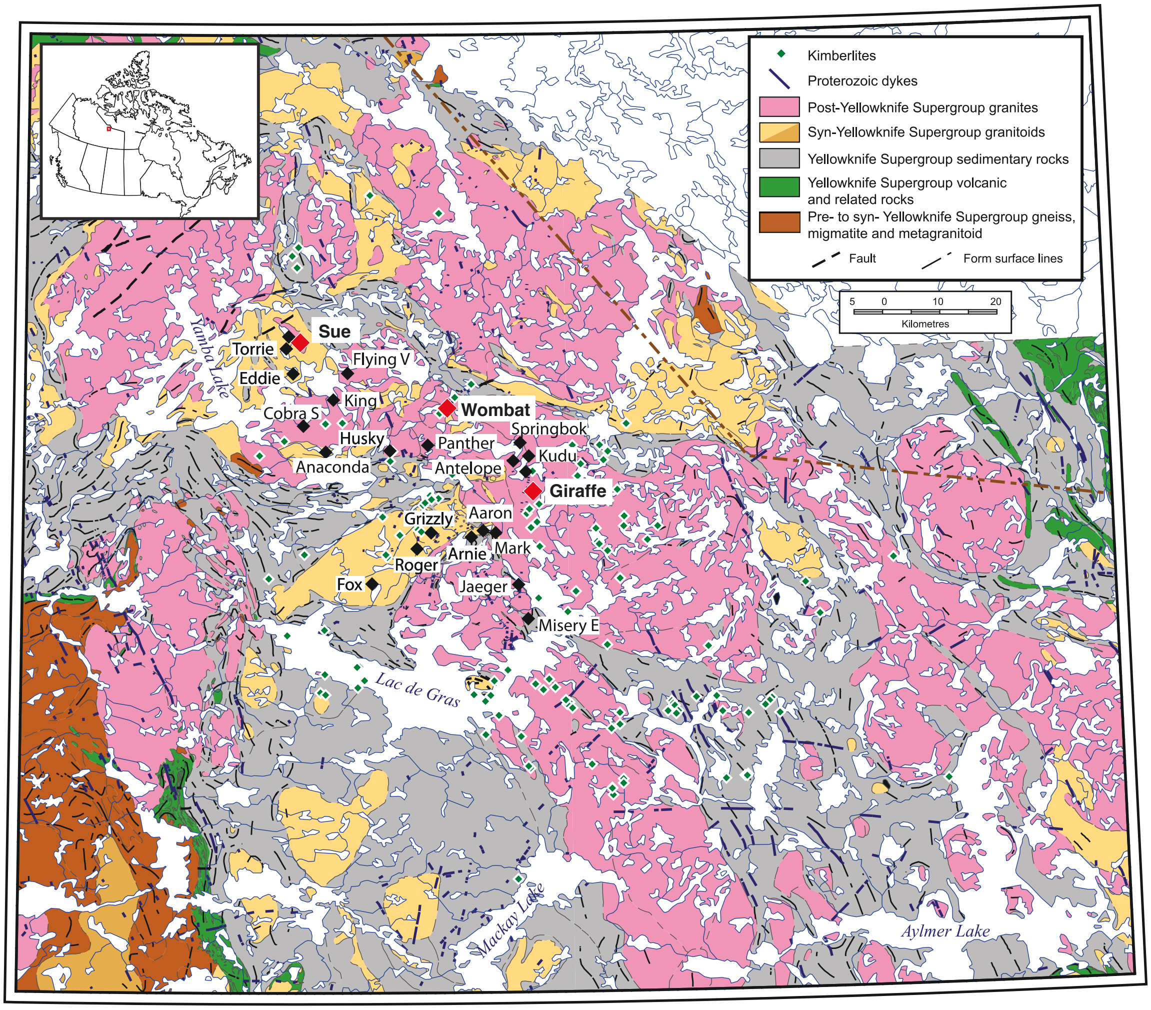

Figure 1.1 Generalized geological map and location of kimberlites in the Lac de Gras region (modified from Sarkar et al., 2015; Kjarsgaard et al., 2002).

CHAPTER 2. GEOCHEMISTRY, GEOCHRONOLOGY, AND PALEOENVIRONMENTS OF THE LATE CRETACEOUS MAAR LAKE SEDIMENTARY FILL OF THE WOMBAT KIMBERLITE PIPE

2.1 INTRODUCTION

Kimberlites are ultramafic volcanic rocks sourced from the mantle that are widely exploited for diamond mining (e.g. Bryan and Bonner, 2003) and the study of deep mantle processes (e.g. Davies et al., 2004). The 1991 discovery of kimberlites on the Slave craton, in subarctic central Canada, led to rapid diamond exploration and identification of over 270 kimberlite pipes in what came to be termed the Lac de Gras kimberlite field. Reports during exploration drilling and open-pit mining highlighted the presence of exceptionally well-preserved plant fossils (e.g. Nassichuk and McIntyre, 1996; Sweet et al., 2003) in association with the Lac de Gras kimberlites. Because most of the kimberlites in the region were emplaced during the Paleocene and Eocene "greenhouse" interval, when atmospheric CO_2 was higher than present (e.g. Wolfe et al., 2017) and there was likely no perennial cryosphere at high latitudes (e.g. Sluijs et al., 2006), the well-preserved organics associated with Lac de Gras kimberlites have considerable potential as paleoclimate and paleoenvironmental archives.

As kimberlite erupts a highly volatile phreatomagmatic explosion leads to a formation of a broadening diatreme and, under exceptional circumstances, to the formation of a post-eruptive crater and maar lake. Maar lakes are known as an excellent source of high resolution paleoenvironmental information. In a small, but relatively deep kimberlitic maar lake, anoxic conditions at the bottom water often facilitate an exceptional preservation of fossil remains and sedimentary organic matter. Despite this potential these deposits have received relatively little attention. Until now only Giraffe kimberlite post-eruptive lake fill was systematically studied as being a source of paleoenvironmental, paleogeographic and paleontological significance. Exceptionally well-preserved Middle-Eocene Giraffe maar sedimentary fill provided an insight on the paleoclimatic conditions during Cenozoic "greenhouse" in a subarctic Canada and hosts a suite of well-preserved microfossils (e.g. early diatoms) and abundant land plant detritus (Wolfe et al., 2017). Additionally, abundant sedimentary xenoliths recovered from the crater fills from Lac de Gras kimberlites were extensively studied as the source of paleogeographic and paleoenvironmental significance providing information about the now eroded cratonic sedimentary cover in Lac de Gras (e.g. Sweet et al., 2003). However, the geological record of cratonic sedimentary cover and associated depositional environments remains sparse in Lac de Gras and requires a much-needed revision taking into consideration kimberlitic maar lake fills as a potential targets for this future studies.

Sediments from one such kimberlite diatreme maar lake are present in the "Wombat" pipe, one of the largest identified kimberlite pipes in the Lac de Gras kimberlite field. The Wombat pipe post-eruptive sedimentary fill is unusually thick and homogenous; as defined in three exploration drill cores that intersect the pipe, over 195 m vertical-equivalent (VE) meters of undisturbed, laminated lacustrine sediment were deposited in the diatreme maar. These sediments host exceptionally well-preserved microfossil remains, which are the only aspects of the Wombat sedimentary record that have received study (Siver et al., 2016). There are no published studies that have addressed the age and paleoenvironmental setting of the Wombat pipe post-eruptive sediments.

The aim of this study is thus to provide a geochronological and paleoenvironmental framework for Wombat maar lake sediments, using a multidisciplinary approach that includes zircon U-Pb geochronology of distal tephra, bulk sediment geochemical analyses, and inferences from microfossil assemblages (Siver et al., 2016). I will demonstrate that the Wombat maar lake sediments were deposited during the late Cretaceous, and likely represent the only preserved remains of strata of this age on the Slave craton. The inferred timing of kimberlite emplacement extends the temporal window of diamondiferous kimberlites in the Lac de Gras field to include the late Cretaceous, and geochemical analysis of the Wombat tephra beds provides insight into the extent and sourcing of volcanism in the region at that time. Finally, the results of this study yield new context on the paleogeography of the Western Interior Seaway in the region during the early Campanian and have important implications for evolution of freshwater diatoms.

2.2 GEOLOGICAL SETTING AND SAMPLES

The Wombat kimberlite maar (64.92° N, 110.45° W; paleolatitude ~63°N, Wolfe et al., 2017) is situated in the Slave craton within the Lac de Gras kimberlite field of Northwest Territories, Canada (Fig. 2.1). The Slave craton is an Archean granite-greenstone terrane of Neoarchean metaturbidites with syn- to post-tectonic granite, tonalite and granodiorite plutons (ca. 2.63 to 2.58 Ga) (Bowring and Williams, 1999; Nowicki et al., 2004). In addition, five major mafic dyke swarms, ranging from ca. 2.23 to 1.27 Ga, and numerous kimberlites of Neoproterozoic, Cambrian, Siluro-Ordovician, Permian, Jurassic, Cretaceous, and Eocene age, intruded the Slave craton (LeCheminant and van Breemen, 1994; Creaser et al., 2004; Heaman et al., 2004; Kjarsgaard, 2001; Sarkar et al., 2015). Studies of sedimentary xenoliths within kimberlite crater fills suggests that the region at various times has been covered by middle Devonian and Cretaceous-Paleogene marine shales and mudstones (Cookenboo et al., 1998; Nassichuk and McIntyre, 1996; Sweet et al., 2003). Notably, xenoliths of Cretaceous marine and Paleogene terrestrial sedimentary cover rocks, together with Paleogene post-eruptive maar lake sediments in the Lac de Gras kimberlite field, suggest a post-100 Ma transition from a marine to terrestrial environment on the Slave craton (Ault et al., 2013; Stasiuk et al., 2002; Stasiuk et al., 2006; Sweet et al., 2003).

At present, the Slave craton is largely devoid of Phanerozoic sedimentary cover rocks. The nearest Phanerozoic cover strata are found in the Brackett Basin ~650 km WNW of the Lac de Gras region (Stasiuk et al., 2006). During the Quaternary the Slave craton was subjected to multiple periods of glaciation. The till blanketing Lac de Gras is mostly 2–5 m thick and is often found capping the surface kimberlite diatremes. The glaciofluvial deposits are also prominent, connecting into an extensive network of sinuous eskers. The modern landscape is dominated by sediments and landforms attributed to advance and retreat of the Laurentide Ice Sheet during the last glaciation (ca. 18, 000 years) (Dredge et al., 1994).

The Wombat kimberlite pipe was initially characterized by horizontal-loop electromagnetic (HLEM) geophysical surveys that defined a quasi-elliptical anomaly (long axis ~475 m; short axis ~250 m) (Fig. 2.2) (Counts, 1996). Diamond exploration efforts resulted in recovery of three drill cores—CH93-29, 00-05, and 05-11—by BHP Billiton Diamonds Inc. in 1993, 2000, and 2005, respectively. Most of core CH93-29 is archived at Connecticut College (New London, USA); core 00-05 is deposited with Northwest Territories Geological Survey core archive in Yellowknife, Canada.

A total of ~195 m (VE) of crater lake facies was intersected by two BHP Billiton Diamonds Inc. exploration drill cores CH93-29 and 00-05 drilled at angles of 45° and 60° respectively (Fig 2.3). The upper ˜180 m (VE) of the crater fill comprises dark poorly consolidated clay-rich laminites with rare lithic and country rock fragments (Fig. 2.4). The lower ˜15 m (VE) of the crater fill comprises grey laminated to massive siltstone with common flattened clay lenses, land plant detritus and fully articulated fish fossil remains (Fig. 2.4; Fig. 2.5). Vivianite and siderite-goethite nodules are unevenly present throughout the lake facies steadily increasing in abundance and size towards the top of the sequence. Two tephra layers were found and sampled from each core at approximately the same depth intervals near the bottom of the lake sequence indicating a potential region of stratigraphic overlap between the two cores two tephra layers from core 00-05 were assigned University of Alberta tephra collection identification codes: UA3134 and UA3135. The cores were further continuously sampled (every ~75 cm of the core length) and each sample identified with the three number code: the first represents the core box number, the second the channel in the box (4 channels in the box, each contains 1.5 m of the core) and the third the depth of the sample in the channel. The detailed sedimentological descriptions for Wombat drill cores 00-05 and CH93-29 are provided in Appendix B tables B.11 and B.12.

The Wombat maar sedimentary fill is nested within the surrounding post-Yellowknife Supergroup Granites (ca. 2.599 – 2.582 Ga) (Kjarsgaard et al., 2002). The age of kimberlite emplacement remains uncertain, with unpublished phlogopite Rb-Sr model ages of ca. 1.8 – 2.5 Ga indicating contamination from local country rock or detrital sourcing (R. Creaser, pers. comm., cited in Siver et al., 2016). Siver et al., (2016), citing unpublished work by Hu et al., (2011), suggest that at least part of the Wombat lacustrine fill is Paleocene in age on the basis of pollen biostratigraphy. This determination was based on the apparent absence of the Late Cretaceous taxa *Aquilapollenites* and *Wodehouseia,* the presence of *Ericaceiopollenites* and *Alnipollenites*, and the absence of *Platycarya*, an Eocene indicator taxon (Hu et al., 2011).

2.3 METHODS

2.3.1 *Carbon isotope and C:N analyses*

Subsamples of Wombat pipe core sediment were ground and weighed prior to treatment with 1 N HCl to remove carbonate. The decalcified samples were rinsed, freeze-dried, weighted (2-5 mg) and loaded into tin capsules. The capsules were then combusted using a FLASH HT Plus Elemental Analyzer with residual nitrous oxides reduced by reaction with Cu. Total organic carbon (C_{org}) and total nitrogen (N_{tot}) were determined with a Thermal Conductivity

Detector (TCD) in the elemental analyzer; carbon isotope ratios were measured with a Thermo Fisher Delta V Plus isotope-ratio mass spectrometer. The carbon isotope ratios are given in standard delta-notation ($\delta^{13}C$) relative to the Vienna Pee Dee Belemnite (VPDB) standard (Craig, 1957). The analytical reproducibility of 0.2 ‰ (2σ) for $\delta^{13}C$ is based on 38 replicate analyses of IRMS soil standards. Carbon isotope and C:N analyses were carried out at the University of Alberta Stable Isotope Geochemistry Laboratory.

2.3.2 Rock-Eval pyrolysis and LECO total carbon determination

Pyrolysis and total organic carbon (C_{org}) analyses of Wombat pipe sediments were carried out using Rock-Eval II and LECO C230 instruments, respectively, at the GeoMark Research analytical services facility. For pyrolysis, ~100 mg of ground sediment was gradually heated in a helium atmosphere to induce the release of hydrocarbons and CO_2. The Hydrogen Index (HI) was calculated by normalizing the released amount of hydrocarbons (HC) between 300-550 °C (S_2) to C_{org} (mg HC/g C_{org}). Similarly, the oxygen index (OI) was calculated by normalizing the released amount of CO_2 during pyrolysis of kerogen (S_3) to C_{org} (mg CO_2/g C_{org}), though due to potential interference of carbonate minerals the OI parameter was not considered further. The organic matter maturation parameter T_{max} is the pyrolysis temperature yielding the maximum hydrocarbon release from cracking of kerogen and is based on the temperature at the time S_2 peak is recorded. Pyrolysis results with S_2 values less than 0.50 mg HC/g rock and less than 0.2 wt% C_{org} were not used, because samples with very low C_{org} usually give erroneous results (Peters, 1986).

LECO analysis of ground, weighed, and decalcified samples was used to measure C_{org} by heating the sample to 1200 °C, measuring the generated CO_2, and comparing the amount to that of a calibration standard. Carbonate percentage (C_{inorg}) was determined by taking the sample weight difference before and after HCl decalcification.

2.3.3 Tephra glass trace and major element geochemistry

Tephra samples from Wombat pipe cores were treated with diluted H_2O_2 to remove organic matter and wet sieved into multiple size fractions, with the 149–75 µm size fraction was retained for analysis. A hand magnet was used to remove magnetite and the remainder was run three times through a Frantz magnetic separator (model LB-1) to remove Fe-rich minerals at 0.2, 0.4, and 0.6 A current settings. The non-magnetic portion was further separated into glass and two mineral fractions using the heavy liquids tetrabromoethane at a density of 2.8 g/cm^3 and methylene iodide at a density of 3.3 g/cm^3. The light, glass-rich fraction was then epoxy mounted in an acrylic puck, polished, and carbon coated.

Single shard glass major-element geochemistry was determined by wavelength dispersive spectrometry on a JEOL 8900 electron microprobe at University of Alberta using 15 keV accelerating voltage, 6 nA beam current, and 10 µm beam diameter. Two secondary standard reference materials, Lipari obsidian (ID 3506) and Old Crow tephra glass (Kuehn et al., 2011), were run concurrently with all samples to assure proper calibration. All data were normalized to 100% on a water-free basis.

Trace-element composition was determined by laser ablation inductively coupled plasma mass spectrometry (LA-ICP-MS) using a RESOlution ArF 193 nm excimer laser ablation system coupled with the Thermo Scientific Element XR Sector Field (SF)-ICP-MS at University of Alberta Arctic Resources Geochemistry Laboratory. Individual glass shards were analyzed with a 23 μm diameter beam at 2.8 J/cm^2 energy density, 5 Hz repetition rate and 20 s ablation time. ^{29}Si was used as an internal standard and the instrument was calibrated against NIST SRM 612. NIST SRM 610 and ATHO-G were analyzed as secondary standards to monitor accuracy and analytical reproducibility.

2.3.4 U-Pb zircon geochronology

Individual zircon grains were handpicked under a binocular microscope from the >3.3 g/cm^3 mineral fraction, mounted in a standard 1” epoxy puck and polished to expose zircon internal surfaces and to remove adhered glass. Cathodoluminescence (CL) and backscattered electron (BSE) imaging of the zircon grains was done using a Zeiss EVO LS15 EP-SEM at University of Alberta. Analysis of individual zircon grains was performed by NewWave 213 nm laser system coupled with a NuPlasma I multi-collector ICP-MS (MC-ICP-MS) at University of Alberta. The analytical procedure involved using a 30 μm beam diameter, 4 Hz repetition rate, ~3 J/cm^2 energy density, and 30 s ablation time. Analytical reproducibility, U-Pb fractionation, and instrument drift were monitored using GJ-1(Jackson et., 2004) primary standard reference zircon grains along with Plešovice (Sláma et al., 2008) and 94-35 (Klepeis et al., 1998) as a secondary zircon standard (Appendix A; Table B.1). Common Pb correction was applied using the ^{207}Pb method (Williams, 1998) with initial Pb composition estimated from Stacey and Kramers (1975) Pb evolution model. Zircon ages are based on $^{206}Pb/^{238}U$ ages with 2σ analytical reproducibility estimated to be 1.9 % based on GJ-1 primary zircon standard results. The weighted mean was used to visualize the crystallization age of the youngest, most coherent zircon group overlapping within 2σ analytical uncertainty using IsoplotR software (Vermeesch, 2018; R Core Team, 2013).

2.4 RESULTS AND DISCUSSION

2.4.1 Tephra glass characterization

The two dated tephra beds were collected from core 00-05. Sample UA3135 (7 cm thick; core depth 270.1 m; VE depth 233.9 m) is ~3 m stratigraphically above sample UA3134 (4 cm thick; core depth 273.43 m; VE depth 236.8 m) (Fig. 2.3; Fig. 2.4). Both tephra beds were light grey and finely laminated, with rare dark interlaminae. Sample UA3134 was dominated by well-preserved glass in the form of tricuspate and platy glass shards with rare partially altered glassy-clay aggregates. UA3135 was more mixed, with partially altered glass pseudomorphs, glassy-clay aggregates, and unaltered glass shards with generally platy morphologies.

2.4.2 Major and trace-element glass geochemistry

The glass major element composition of UA3134 is variable (Figs. 2.6, 2.7; Table B.5), with wt.% of 73.10 – 75.33 SiO_2, 0.25 – 0.49 TiO_2, 12.58 – 14.32 Al_2O_3, 2.17 – 2.78 FeOt, 0.18 – 0.44 MgO, 1.18 – 1.89 CaO, 1.66 – 4.28 Na_2O, and 2.80 – 6.35 K_2O. Notably, K_2O increases with increasing SiO_2, while Na_2O decreases. No significant variability is observed in the range of trace element concentrations, with 92.9 ± 2.3 ppm Rb, 106.9 ± 2.5 ppm Sr, 22.6 ± 0.8 ppm Y, 125.8 ± 2.8 ppm Zr, 3.7 ± 0.4 ppm Nb, 1048.2 ± 23.9 ppm Ba, and 13.8 ± 0.5 ppm La. Light rare earth elements (LREE) are enriched relative to heavy rare earth elements (HREE), with $(La/Yb)_N = 3.5 \pm 0.7$), and there is a negative europium anomaly ($Eu/Eu^*_N = 0.62$) (Fig. 2.8).

Glass shards from UA3135 have greater major element variability than the overlying UA3134 tephra, particularly in SiO_2 (72.9–76.4 wt.%), CaO (0.56–1.88 wt.%), and MgO (0.25 – 0.73 wt.%). Trace element concentrations are largely homogeneous (95.0 ± 5.2 ppm Rb, 109.2 ± 2.2 ppm Sr, 23.0 ± 0.9 ppm Y, 126.7 ± 5.2 ppm Zr, 3.8 ± 0.4 ppm Nb, 1041.8 ± 36.4 ppm Ba and 14.8 ± 0.5 ppm La), with similar LREE enrichment $(La/Yb)_N = 3.9 \pm 0.3$) and negative Eu anomaly ($Eu/Eu^*_N = 0.77$) to sample UA3134 (Fig 2.8).

2.4.3 Glass geochemistry discussion

The trace element geochemistry of the two Wombat tephra beds is practically indistinguishable, suggesting that they probably originate from the same or similar tectonomagmatic environment. The greater variability in major element composition as compared to trace element composition indicates the effects of post-depositional alteration, making them less suitable for tephra characterization (e.g. for classical tephrostratigraphic correlation). Total alkali content ($Na_2O + K_2O$) and SiO_2 were used to characterize tephra glass on a non-genetic basis (LeBas et al., 1986). On this basis, both UA3134 and UA3135 glasses are classified as low-silica rhyolites ($SiO_2 < 75$ wt.%) (Fig. 2.7).

The Nb - Y and Rb - (Y + Nb) tectonomagmatic discrimination diagrams were used to constrain the tectonic setting of the parent volcanism. This classification scheme is based on the trace element compositions of unaltered granitoid rocks from different tectonic settings, e.g. ocean ridge, volcanic arc, intraplate, and collisional settings (Pearce et al., 1984). The trace element compositions for UA3134 and UA3135 glasses plot as volcanic arc granites (Fig. 2.9) and thus probably originated from a continental magmatic arc setting, which is coincident with LREE enrichment and relatively high Ba and Rb concentrations (Fig. 2.8). Additionally, low Ta and Nb contents (Ta 0.2 ± 0.1 wt.%; Nb 3.7 ± 0.4 wt%) and consequently negative Nb-Ta anomalies in glasses from both tephra samples also suggest resemblance to volcanic arc granites (Harris et al., 1986) Similarly, using Th/Hf vs. Ta/Hf tectonomagmatic discrimination diagrams from Schandl and Gorton (2002), the tephra samples plot in the active continental margin field (Fig 2.10). The geochemical composition of the volcanic glass and small grain size of the samples strongly suggest distal origin of the tephra deposits possibly form a volcanic arc system and not the more proximal kimberlitic volcanism as the source.

Post-depositional weathering and alteration of tephra can result in the depletion or enrichment of elements in volcanic glass. In glass from UA3135, and to a lesser degree UA3134, glasses alkali and alkali earth elements (Na, K, Ca) are mostly variable indicating their mobility. The effects of alteration are also evident in TAS and bivariate plots vs. TiO_2 (Fig. 2.6). Na and K are the most variable, K is slightly enriched in both samples compared to Na. Si, Al, Fe and Ti show the least variation, suggesting that they are relatively immobile. The Chemical Index of Alteration (CIA) of the samples average at 62.6 for the UA3134 and 68.3 for the UA3135, suggesting low to intermediate chemical weathering of the glass. Trace element concentrations are more consistent than those of major elements, indicating little mobility during diagenetic alteration of the glasses. However, some variation in Th/U can be attributed to relative post-depositional mobility of U. The tephra glasses also do not show a negative Ce anomaly, which would be expected in the case of low-temperature alteration by oxic sea water (Piper, 1974).

2.4.4 U-Pb zircon dating

A total of 34 zircon grains from tephra sample UA3135 and 3 zircon grains from tephra sample UA3134 were analyzed using by MC-LA-ICPMS (Tables B.2, B.3). Most zircon grains were euhedral to subhedral, or partially broken fragments, with an average diameter less than 60 μm. The CL imaging in both samples shows that oscillatory zoning is the predominant type of internal texture, though some grains exhibit no visible zoning. Several grains had partially weathered from the sample UA3135 had adhered glass rims, suggesting that they have a magmatic rather than a xenocrystic origin.

The common Pb corrected ^{206}Pb/^{238}U dates from UA3134 were not coherent. Two zircon grains gave ages of ca. 190 Ma and one grain dated to ca. 1370 Ma. These are not known ages of magmatism on the Slave craton, thus suggesting contamination by xenocrysts or antecrysts during the eruption from volcanic and/or crustal sources.

In contrast, common Pb corrected $^{206}Pb/^{238}U$ dates from UA3135 yielded a tighter age range from 72.9 to 99.1 Ma. The youngest population overlapping within uncertainty yields a weighted mean $^{206}Pb/^{238}U$ date of 82.36 ± 0.44 Ma (n = 18, MSWD = 1.51) (Fig. 2.11). The MSWD of this dataset is on the high side of the recommended range (0.445-1.776) for a single population (Mahon, 1996). The high MSWD likely results from underestimation of analytical uncertainty or internal zircon heterogeneity and compositional complexities. The weighted mean of these 18 grains likely represents the crystallization date of a single population. Considering that zircon may reside in the magma chamber for an unspecified period of time ranging from 10s to 100s of thousands of years before the eruption occurs (Costa, 2008), the crystallization age is thus a maximum age for tephra deposition. Fifteen older zircon grains in UA3135 indicate contamination by xenocrysts and antecrysts during the eruption, rather than admixing of detrital material, since the sampled tephra bed had no indication of post-depositional reworking. One zircon grain dated to 72.9 ± 1.5 Ma and is far younger than the main population; the outlier probably resulted from postcrystallization loss of radiogenic Pb from zircon (Fig. 2.12). This interpretation is further supported by observation of continuous decrease in $^{206}Pb/^{238}U$ as a function of increasing depth in the ablation pit. The high surface area to volume ratio of the small grain (~ 35 μm) also makes it more prone to Pb loss (Silver and Deutsch, 1963).

2.4.5 Timing of the Wombat maar sedimentation and kimberlite magmatism

We interpret the UA3135 zircon U-Pb weighted mean age of 82.36 ± 0.44 Ma to be a close minimum age estimate for the onset of Wombat maar sedimentation. On this basis, we place the start of the lake infilling around the early Campanian age during the Late Cretaceous. This radiometric age constraint is inconsistent with the Paleocene age previously determined using stratigraphic palynology (Hu et al., 2011) from a limited number of samples from the Wombat pipe lacustrine sediments. The Late Cretaceous index taxa *Aquilapollenites* Rouse and *Wodehouseia* Stanley are absent from the pollen assemblage, as is the Eocene marker taxon *Platycarya*. Pollen of the Neogene taxa *Ericaceiopollenites* and *Alnipollenites* is abundant. Hu et al., (2011) thus suggested a Paleocene age for the maar sediments. It is possible that several eruptions may have occurred during the sedimentation of the crater re-ejecting the fill and modifying pipe morphology leading to distortion of the pollen record, but more evidence is required to validate the occurrence of additional eruptions. Resolution of the discrepancy between the radiometric tephra ages and the pollen biostratigraphy awaits new pollen analysis of a series of samples spanning the entire Wombat lacustrine fill sequence, which is currently in process with Eva Koppelhus (University of Alberta).

The Wombat kimberlite does not have an established emplacement age, with previous attempts using phlogopite Rb-Sr model ages (R. Creaser, pers. comm., cited in Siver et al., 2016) and U-Pb rutile (S. Buryak and C. Sarkar, unpublished data) yielding inconclusive data. However, comparison of the Wombat tephra zircon ages to the known radiometric emplacement ages from the Lac de Gras and Alberta kimberlite clusters shows that there is a consistent temporal correlation. The oldest Cretaceous kimberlites with known emplacement ages in Lac de Gras include the Kudu (73.7 ± 7.4 Ma), C13 (73.9 ± 2.6), Jaeger (71.4 ± 7.8 Ma), and Hardy Lake kimberlites (71 – 73 Ma), which are younger than the Wombat maar sediment age (Heaman et al., 2004; Sarkar et al., 2015). In Alberta, Maastrichtian – Santonian kimberlites are present in the Birch Mountains (70 -78 Ma) and Buffalo Head Hills (81 – 88 Ma) (Heaman et al., 2004; Eccles, 2011). If the Wombat sedimentation began shortly after kimberlite emplacement, it is plausible that the Wombat kimberlite eruption occurred during the early Campanian which coincides well with a temporal pattern of Cretaceous kimberlite magmatism in the western North America.

2.4.6 Results and interpretation Rock-Eval Pyrolysis and LECO C_{org}

The results of Rock-Eval pyrolysis indicate low thermal maturity of organic matter, with T_{max} values ~425 °C. The HI values are low, between 18.1 and 185.9 mg HC/g C_{org}, suggesting a high contribution of humic material from land plants. The HI vs. T_{max} diagram shows that all of the Wombat maar samples plot in Type III kerogen field (Fig. 2.13), which is characteristic of terrestrial vascular plant material (Espitalié et al., 1984; Talbot and Livingstone, 1989). Result from LECO analysis (Table B.9) indicate variable carbonate content (C_{inorg} = 5.3 – 39.1 wt.%) that generally decreases upcore, and total organic carbon contents that are generally high (C_{org} = 1.7 – 10.3 wt.%).

Typically, HI < 200 HC/g C_{org} indicates abundance of woody, oxidized or carbonized plant material, but it can also reflect increasingly oxidizing conditions during subaerial exposure of lacustrine sediment (Talbot and Livingstone, 1989). Decrease in both HI and C_{org} values can occur as an effect of oxidation and bacterial respiration during subaerial exposure or low water level conditions in the lake. It is plausible that some of the very low HI (< 50 HC/g C_{org}) and C_{org} values can be associated with a low water conditions, however no obvious subaerial surfaces have been identified in the Wombat cores.

2.4.7 Results and interpretation of $\delta^{13}C$, C_{org} and atomic $C_{org}:N_{tot}$

Sedimentary organic matter $\delta^{13}C$, C_{org}, and atomic $C_{org}:N_{tot}$ display marked variability over the ~ 195 m (VE) of sampled core from the Wombat maar (Fig 2.14). The elemental analyzer C_{org} concentrations are variable but generally high, between 1.1–8.8 wt.%. High C_{org} content can be attributed to good preservation of organic matter under reducing conditions below the oxic-anoxic interface. The C_{org} and N_{tot} have a strong positive correlation ($r^2 = 0.82$), although the regression line intercept suggests a small contribution of inorganically bound nitrogen in excess of that associated with organic matter (Fig 2.15). The atomic $C_{org}:N_{tot}$ ratios ($C_{org}:N_{tot}$ mass ratio multiplied by atomic weights of nitrogen and carbon) are used in this study because they reflect biochemical stoichiometry (Talbot, 2001). The atomic $C_{org}:N_{tot}$ varies between 14.6 and 38.4 with a mean value of 24.1, with intervals of relatively high and consistent values (~25-30) at 222.4 - 178.8 m and 125 - 66.4 m VE depth. The $\delta^{13}C$ varies between - 30.2 ‰ and -25.3 ‰ with a mean value of -26.6 ‰ and with intervals of relatively uniform values between -26 ‰ to -27 ‰ at 222.4 - 178.8 m and 125 - 66.4 m VE depth (Fig. 2.14).

The $\delta^{13}C$ and C_{org}:N_{tot} ratios can be used to discriminate the type of the organic matter source (terrestrial vs. aquatic). Plants using the C_3 photosynthetic pathway have $\delta^{13}C$ values between about -20 ‰ to 30 ‰, compared to values of ~ -10 to -15 for C_4 plants (Tieszen et al., 1979; Meyers, 1994). C_3 terrestrial plants are isotopically indistinguishable from C_3 algae but have a higher C_{org}:N_{tot} ratios ≥ ~ 20. Thus, $\delta^{13}C$ and C_{org}:N_{tot} of the sediments from the Wombat maar indicate predominance of organic matter derived from C_3 terrestrial plants (Fig. 2.16). These results are in agreement with low HI values suggesting high contribution of land plant material to the lake sediment organic matter (Type III kerogen).

C_{org} concentrations change with depth and record fluctuations in organic matter delivery rates and preservation. Based on the C_{org}:N_{tot} ratio depth profile, values ≥ 20 reflect high contributions of land-derived plant organic matter, which also corresponds to elevated C_{org} concentrations. Intervals of C_{org}:N_{tot} ≤ 20 correspond broadly to lower and more variable C_{org} values; this probably indicates increased contribution of algal organic matter to the sediment, reflecting the shift in proportions of allochthonous and autochthonous organic material (Meyers and Ishiwatari, 1993). The variation in C_{org} can also reflect a lower preservation potential of algal organic matter as compared to that from vascular terrestrial plants.

Carbon cycling and post-burial diagenetic processes (i.e. denitrification) within the lake can alter sediment isotopic composition and C_{org}:N_{tot}, and must be taken into consideration when interpreting those data. Sediment $\delta^{13}C$ values can become more negative in response to carbon cycling under anoxic conditions through production and deposition of ^{13}C-depleted biomass via activity of anaerobic bacteria in and above the anoxic zone (Hollander and

Smith, 2001; Whiticar, 1999). Furthermore, under anoxic or dysoxic conditions denitrification can lead to a significant loss of nitrogen through microbial conversion of NO_3^- and nitrogen in organic matter to gaseous N_2, causing an increase in C_{org}:N_{tot} ratios (Deines, 1980; Van Mooy et al., 2002). Bioturbation is another process that can add to degradation of organic matter through activity of benthic fauna. The presence of frequently laminated lake sediment in the Wombat maar indicate little to no biological mixing or resuspension and the absence of significant bioturbation zone (Meyers and Ishiwatari, 1993).

2.5 PALEOENVIROMENT AND PALEOGEOGRAPHY

2.5.1 The Wombat maar paleoenvironment

The results of this study indicate that the Wombat maar was a small lake with at least semi-permanent bottom water anoxia formed during the earliest Campanian. The combination of excellent preservation of the fossil remains and plant detritus, absence of bioturbation zones, and abundant vivianite nodules collectively suggest that anoxic conditions were common at the bottom of the Wombat lake. Vivianite [$(Fe_3(PO_4)_2 \cdot 8H_2O)$] is commonly observed forming under reducing conditions in slightly alkaline (pH 7-8), non-sulfidic, iron-dominated lakes (O'Connell et al., 2015). Though the processes associated with vivianite formation are poorly understood, its abundance in the Wombat lake sediments suggests presence of reducing conditions.

Based on mean sedimentation rates for Cenozoic maar lakes in subarctic Canada and Central European Volcanic Province, and the minimum ~195 m of lacustrine sediment present in the

Wombat maar, the lake likely persisted for at least ~100 000 years. Bulk sediment geochemical parameters ($\delta^{13}C$, C_{org}, atomic C_{org}:N_{tot}, HI) indicate a dominance of a terrestrial organic material derived primarily from C_3 land plant, interspersed with periods of increased autochthonous organic matter production. Based on this, the presence of fossil angiosperm plant foliage, and woody plant detritus in the sediment, the Wombat maar lake was unambiguously nested in a terrestrial environment. The climate during the Late Cretaceous in Arctic regions was significantly warmer than present, with a high in Turonian and declining by the Campanian (Barron, 1983, Amiot et al., 2004).

2.5.2 Early freshwater diatom occurrence

The zircon U-Pb geochronology for the Wombat maar sediments provides substantial new insight into the evolutionary origin of freshwater diatoms. Diatoms are unicellular, photosynthetic organisms with opaline silica cell walls that are present in numerous aquatic habitats worldwide. The fossil record suggests that marine diatoms radiated extensively during the Early Cretaceous (Siver et al., 2018), but there is little record to constrain the timing of their expansion into freshwater habitats (Harwood et al., 2007). The most recent work on the early freshwater diatom fossil record suggests that diatoms colonized freshwater systems sometime during the Late Cretaceous but did not become prominent until the middle to late Eocene (Siver et al., 2010; Benson and Kociolek, 2012). Carbonaceous cherts from the Late Cretaceous Tarahumara Formation in Mexico (ca. 70 Ma) contain one of the oldest known freshwater diatom occurrences (Chacón-Baca et al., 2002). However, the uncertainty in the conditions of the habitat and absence of a positive taxonomic assignment have led to questions whether diatoms indeed inhabited a freshwater environment (Sims et al., 2006). Latest Cretaceous (ca. 65 Ma) occurrences of the freshwater diatom taxon *Aulacoseira* are known from the Deccan Intertrappean beds (Singh et al., 2006). More recently, freshwater diatoms were reported from the Battle Formation (ca. 66.5 Ma) in western Canada, including *Aulacoseira* and seven other pennate morphotypes (Siver et al., 2018).

The Wombat maar sediment have already yielded a diverse and well-preserved siliceous microfossil assemblage (Siver et al., 2016). The microfossil assemblage includes the new centric freshwater diatom genus *Fideliacyclus wombatiensis*, and abundant remains of chryophyte cysts, synurophyte and chrysophyte scales, heliozoans, and other diatoms. The U-Pb zircon age of ca. 83 Ma reported here for the Wombat maar sediment fill suggests that this locality is a strong candidate for the world's oldest freshwater diatom occurrence. Considering that Western Interior Seaway extended over the Lac de Gras region at some point during the Cretaceous (Sweet et al., 2003) (Fig 2.17), it is plausible that marine diatom species colonized freshwater environments in the region during the early Campanian seaway regression, in turn acquiring complex cell wall morphologies as they adapted to this new environment.

2.5.3 Paleogeography of the Western Interior Seaway

During most of the Cretaceous, the Western Interior Seaway (WIS) covered a vast portion of North America spanning more than 6000 km from the Gulf of Mexico to the Arctic Ocean with a width of more than 1600 km at the maximum extent (Leckie et al., 1991; Hay, 1995).

The WIS first linked the Gulf of Mexico and the Arctic Ocean during late Albanian, with permanent connectivity established during the Cenomanian and persisting at least until the early Maastrichtian (Slattery et al., 2015). At broad spatial scales, paleogeographic changes of the WIS are characterized by a periodic transgressive-regressive cycle as a response to global and regional climatic fluctuations. The reconstruction of the WIS involves a multitude of data sets, from outcrops and hydrocarbon wells spanning a large area, that are nevertheless commonly limited by hiatuses in the stratigraphic record or patchy spatial coverage of outcrops. In particular, broad swaths of subarctic Canada, such as the Lac de Gras region, are devoid of known Phanerozoic sedimentary rocks, making it difficult to infer WIS paleogeography in those areas.

In this context, the Wombat maar lake sequence represent the only intact early Campanian sediment record in the Lac de Gras region. Combined with insight from xenoliths in Lac de Gras kimberlite facies, these records provide an important glimpse into depositional conditions during a period that is otherwise unrepresented in the rock record of that region. Organic geochemistry, palynology, and petrophysical analysis allow us to determine the age and the depositional environment of the Tertiary and Cretaceous sedimentary cover during and before kimberlite emplacement. The (U-Th)/He apatite (AHe) thermochronometry, combined with vitrinite reflectance data from sedimentary xenoliths, also yields estimates for the approximate burial depth of the strata. Here I synthesize results from sedimentary xenoliths from eight volcanoclastic kimberlite fills (DO18, EG130-1, T14, AB2, Scorpion, Panda, Hawk and Hardy Lake) and four kimberlitic maar sedimentary fills (Giraffe, Sue, Wombat, KBS-3).

The vitrinite reflectance and AHe thermochronometry data suggest that the Lac de Gras region was covered by Cretaceous strata ranging between 1.4 – 2.7 km, which is significantly thicker than early estimates between 100 to <300 m (Stasiuk et al., 2002; Ault et al., 2015). The palynology of sedimentary xenoliths provides further context on the inferred stratigraphic order in the region. Between ca. 90 - 105 Ma, palynomorph assemblages and kerogen types in kimberlite sedimentary xenoliths indicate a marine or marginal marine depositional environment, suggesting that the Lac de Gras area was near the sea level at this time (Nassichuk and McIntyre, 1995; McKinlay et al., 1998; Stasiuk et al., 2002; Sweet et al., 2003). Sedimentary xenoliths dating between ca. 80 – 90 Ma are only encountered in Hardy Lake kimberlites, which contain terrestrial Type III kerogen but likely with significant reworking and recycling of organic matter (Stasiuk et al., 2002). During this time, Sweet et al., suggested a significant hiatus in deposition due to absence of age indicative pollen assemblages (2003).

However, the results of this study indicate that during the early Campanian the WIS regressed and the Lac de Gras area was above sea level. Data from EG130-1 and Hardy Lake kimberlite xenoliths suggest that the WIS presumably transgressed again during the late Campanian, submerging the Lac de Gras region under full marine conditions followed by a hiatus between ca. 69 – 73 Ma (McKinlay et al., 1998; Stasiuk et al., 2002; Sweet et al., 2003). Xenoliths from kimberlites EG130-1, AB2, T14, and post-eruptive sediment fills from Giraffe, Panda, and KB-3 pipes, suggest that non-marine conditions persisted between ~ 45 - 69 Ma, with a gap in record between ca 56 - 61 Ma (McKinlay et al., 1998; Stasiuk et al., 2002; Hamblin et al., 2003; Sweet et al., 2003; Wolfe et al., 2012). At some point after ~ 45 Ma, most of the Cretaceous strata must have been eroded away by river systems or preserved only regionally as a kimberlitic maar lake fills. (Bell, 1885; Duk-Rodkin and Hughes, 1994). Hence, at Lac de Gras, at least four periods of erosion/hiatuses in deposition can be inferred: ca. 95 – 98 Ma, ca. 83 – 90 Ma, ca. 69 – 73 Ma and ca. 56 – 61 Ma, based on the absence of the palynomorphs indicative of this time periods in the sedimentary xenoliths records (Sweet et al., 2003). The exact timing of erosional events and the final complete unroofing of Lac de Gras is not clear but it probably occurred during post-100 Ma elevation gain of the Slave craton due to the effects of Cordilleran orogenesis along the western plate boundary of North America (Ault et al., 2013).

Regional correlation of marine and non-marine sedimentation between contemporaneous sequences along the Manitoba Escarpment, Brackett Basin, and Sverdrup Basin, together with inferred stratigraphy in Lac de Gras area, provides a broader perspective on WIS paleogeography (Fig 2.17). The Brackett Basin, ~650 km WNW of the Wombat locality, is the closest sedimentary sequence to the Lac de Gras area (Sweet et al., 1989). The Little Bear Formation in the Brackett Basin has been interpreted as a series of delta-front or propagating shoreface deposits, contains both marine and non-marine strata, and is roughly contemporaneous to that of the Wombat maar sedimentary fill (Dixon, 1999). The underlying and overlying Slate River/Trevor (Cenomanian–Turonian) and East Fork (Campanian–Maastrichtian) Formations are characterized as a marine deposits, suggesting a Turonian regression of the WIS and transgression sometime in the Late Campanian (Yorath and Cook, 1981).

The Manitoba Escarpment is a mostly marine Cretaceous sedimentary sequence located ~1300 km SE of the Lac de Gras region, roughly along depositional strike. The Cenomanian to Late Campanian formations in the Manitoba Escarpment were deposited in a marine setting near the eastern margin of the Western Canada Sedimentary Basin (Braman et al., 1995; Schröder-Adams et al., 2001). The late Maastrichtian to Paleocene formations (the Boissevain Court and Turtle Mountain Formations) are mainly non-marine and represent final regression of WIS in the region.

The Sverdrup Basin is a rift basin located over the Queen Elizabeth Islands and inter-island channels ~1500 km NE of the Lac de Gras region. The predominately marine Cretaceous strata of the Bastion Ridge Formation, the Kanguk Formation, and a lower section of the Eureka Sound Group combined span the Cenomanian to early-middle Paleocene suggesting the region was below sea level for the most of the Late Cretaceous (Ricketts and Stephenson, 1994; Embry and Beauchamp, 2019). By the middle-late Paleocene the area was predominately non-marine, as indicated by terrestrial plant fossils in the Iceberg Bay Formation within Eureka Sound Group on Ellesmere Island (Williams et al., 2009).

The ages and depositional environments of stratigraphic sequences in the Brackett Basin, Manitoba Escarpment, and Sverdrup Basin, together with the xenolith and kimberlite sediment records from Lac de Gras, make it possible to infer patterns of regression-transgression of the northern reaches of WIS shoreline (Fig. 2.17). Marine conditions persisted at all of the localities from Cenomanian to at least middle-Turonian time, followed by hiatuses in the Brackett Basin and Lac de Gras lasting at least until the late Santonian. An early Campanian member of the Little Bear Formation and the Wombat maar lake sequence both contain unambiguous terrestrial signatures, suggesting at least a regional narrowing of the WIS and a shift to a non-marine environment at the Lac de Gras site, while the Manitoba Escarpment likely had hiatus in deposition and Sverdrup Basin remained below the sea level. The subsequent middle – late Campanian transgression of the WIS reversed conditions back to the full/marginal marine environment in the Lac de Gras region and the Brackett Basin. The timing of final shift from marine to permanent terrestrial setting in the Lac de Gras region is unclear but probably occurred sometime in the late Maastrichtian to early Paleocene.

2.5.4 Late Cretaceous volcanism and regional correlation

Late Cretaceous silicic tephra beds are common in sedimentary strata of the Sverdrup Basin and throughout Alaska, but the two tephra deposits characterized here from the Wombat maar sediment are the first to be described from the Slave craton. Both tephra samples, UA3135 and UA3134, are very fine silica-poor rhyolites with trace element composition pointing to an origin in a continental magmatic arc (Figs. 2.9, 2.10). This magmatic affinity indicates a markedly distal origin for the Wombat tephras, with potential source regions in NE Eurasia (Okhotsk-Chukotka Volcanic Belt), NW North America (e.g., the Alaska Range-Talkeetna Mountain magmatic belt, Kluane arc, Coast arc, Idaho batholiths), and the Canadian High Arctic.

The Okhotsk-Chukotka Volcanic Belt (OCVB) is a subduction-related magmatic province in NE Eurasia, located on the western coast of the Sea of Okhotsk to the east of the Chuckhi Peninsula. The OCVB is characterized by voluminous high-silica magmatism (SiO2 ≥ 80 vol.%) that occurred in five main episodes, with the most recent at ca. 79 – 82 Ma (Tikhomirov et al., 2012; Pease et al., 2018). The zircon U-Pb ages for the rhyolitic ignimbrites of the western Okhotsk flank zone of the OCVB suggest occurrence of volcanism from the Coniacian to the Campanian – Maastrichtian boundary (ca. 70 – 83 Ma), which is contemporaneous with the Wombat tephra zircon U-Pb ages (Tikhomirov et al., 2012). The OCVB is located > 2500 km NW of the Wombat locality requiring a very intense, large scale Plinian-type volcanism in order to reach that far east. Prevailing winds would plausibly transport a tephra plume from the OVCB eastwards towards the Lac de Gras region in northern North America, consistent with the lack of OVCB tephra deposits west of the source region (Spicer and Herman, 2010).

Several regions of NW North America host ca. 60 - 80 Ma plutons and volcanic rocks with geochemical compositions typical of a continental-margin volcanic settings (Moll-Stalcup, 1994; Cecil et al/, 2011; Gaschnig et al., 2011). However, post-Cretaceous tectonic activity and erosion left only local evidence for magmatism. The evidence from preserved localities such as Coast arc, Kluane arc, and Idaho batholiths, combined with evidence from detrital zircon U-Pb dating, all suggest active arc volcanism spanning most of the Late Cretaceous (Trop et al., 2005) and thus are plausible source regions for the Wombat rhyolitic tephra beds.

The Hansen Point Volcanic Complex (HPVC) on Ellesmere Island is a less likely source for the Wombat tephra beds because most of the HPVC rocks have an intarplate geochemical signature and probably were erupted in a continental rift setting (Balkwill, 1978). The sparse radiometric age data from the HPVC suggest a broad range between ca. 75 – 95 Ma, which makes temporal correlation with the Wombat samples more difficult (Trettin and Parrish, 1987; Estrada and Henjes-Kunst, 2004, 2013; Bono et al., 2013). The geochemical affinity of the rocks and sparsity of the age data thus make the HPVC an unlikely candidate for the eruption source of the Wombat tephra beds.

Middle – late Cretaceous bentonite and tephra deposits that are potential correlatives for the Wombat tephra beds occur extensively in northern Alaska (e.g. Seabee Formation, Schrader Bluff Formation, Prince Creek Formation, Hue Shale Formation), the Mackenzie Delta (e.g. Boundary Creek Formation, Smoking Hills Formation) and the Canadian Arctic Islands (Kanguk Formation) (e.g. Molenaar et al., 1987; Bacon et al., 1990; Parsons, 1993; Kemp, 1994, Dixon, 1996; Bergman et al., 2006). Late Cretaceous rhyolitic tephra beds and bentonites were also recovered in piston cores from the Northwind Ridge, Chukchi

Borderland; however potassium – argon ages on biotite suggest that they are somewhat older (Cenomanian) than the Wombat samples (Phillips et al., 1998). It has been suggested that Cretaceous tephra deposits in northern Alaska and the Mackenzie Delta likely were derived from OCVB caldera-forming eruptions (Miller et al., 2002; Bergman et al., 2006), but absence of detailed published geochemical and age data make it difficult correlate them individually with the Wombat samples glass geochemistry.

The Upper Cretaceous tephra deposits preserved in the Kanguk Formation (Canadian Arctic Archipelago), however, have been characterized using major and trace element glass geochemistry by Kemp (1993). The age of the individual tephra deposits described by Kemp (1993) is uncertain, but SIMS and CA-ID-TIMS U-Pb ages on zircon from Kanguk Formation bentonites suggests volcanism spanning Cenomanian to early Campanian time (ca. 93 Ma – 83 Ma), with the youngest bentonites in the upper section of the Kanguk Formation dating at 83.1 +1.0/-2.1 Ma (bentonite S_PH0256) and 83.80 ± 0.21 Ma (bentonite C84) (Davis et al., 2017; Pointon et al., 2019).

The Kanguk Formation tephra beds are mostly fine-grained high-silica rhyolites that probably originated in a continental magmatic arc setting (Kemp, 1993). The trace element geochemistry broadly matches those found in the Wombat maar (eg. samples UT940, UT629), but with several major distinctions. The geochemical composition of the glass shows higher LREE and Sm, and typically lower Ba, than glasses in the Wombat maar samples. The Wombat maar tephra glasses have a high negative Eu anomaly (Eu/Eu^*_N =

0.62 - 0.77) compared to the moderate negative Eu anomaly ($Eu/Eu*_N$ = 0.24 – 0.71) for Kanguk Formation tephra.

Importantly, potential geochemical correlation of Kanguk Formation and Wombat maar tephras will require single-grain reanalysis of the trace element composition using modern instrumentation (LA-ICP-MS), since the original analyses of Kemp (1993) were conducted by older, lower sensitivity LA-ICP-MS methods and also could have been a subject to microcryst contamination. Nevertheless, the broadly similar tephra characteristics suggest that Wombat tephra deposits probably originated from a similar tectonomagmatic setting as those found in the Kanguk Formation. Based on their geochemistry, the distal nature of the glass and mineral content, and paleo-wind inferences, the most likely eruption source area for the Wombat tephra beds is the OCVB, although northern Alaska sources cannot be discounted entirely. The sparse availability of reliable geochemical and geochronological data for Late Cretaceous tephra deposits in northern North America is a major hurdle for reliable correlation of these distal tephra tephra beds, despite their potential applicability as tephrostratigraphic marker horizons.

2.6 CONCLUSION

The well preserved, post-eruptive sedimentary fill of the Wombat maar provides a unique paleoenvironmental snapshot of the Late Cretaceous in the Lac de Gras region, which is otherwise largely devoid of any Phanerozoic strata. The lacustrine sedimentary succession recorded in the two exploration drill cores examined here was deposited in a small, predominantly anoxic lake in a terrestrial setting, with substantial contribution of C_3 plant material to the organic-rich lake sediments inferred from bulk sediment geochemical parameters.

The geochronology of the Wombat maar sedimentary fill, as determined by zircon U-Pb dates from distal rhyolitic tephra bed found near the base of the lake sequence, yields a close minimum age for onset of lacustrine deposition at 82.36 ± 0.44 Ma (early Campanian). This chronology suggests that siliceous microfossils from the Wombat maar sediments represent the oldest-known occurrence of freshwater diatoms.

Trace and major element composition of rhyolitic tephra beds in the Wombat maar fill expand the currently limited knowledge on the extent of Late Cretaceous volcanism in arctic and subarctic Canada. Wombat tephra age and glass geochemistry suggest that the most probable volcanic sources for the tephra beds are the Okhotsk-Chukotka Volcanic Belt in NE Eurasia or northern Alaska sourcing. Trace element composition of the Wombat tephra yields potential correlation with distal tephra recovered from the Kanguk Formation on Ellesmere Island, but sparse geochronology for the Kanguk Formation tephra beds is a source of ambiguity.

The Wombat maar sediments are the only record of the early Campanian terrestrial strata in Lac de Gras, providing a paleoenvironmental snapshot that supplements limited information from xenoliths of now-eroded Mesozoic cover rock in Lac de Gras kimberlites. Together with stratigraphic sequences from sedimentary basins elsewhere in midcontinent Canada, the Wombat maar sediment provide new insight on Lake Cretaceous and Paleogene paleogeography of a data-poor region of the Western Interior Seaway.

2.7 CHAPTER 2 FIGURES

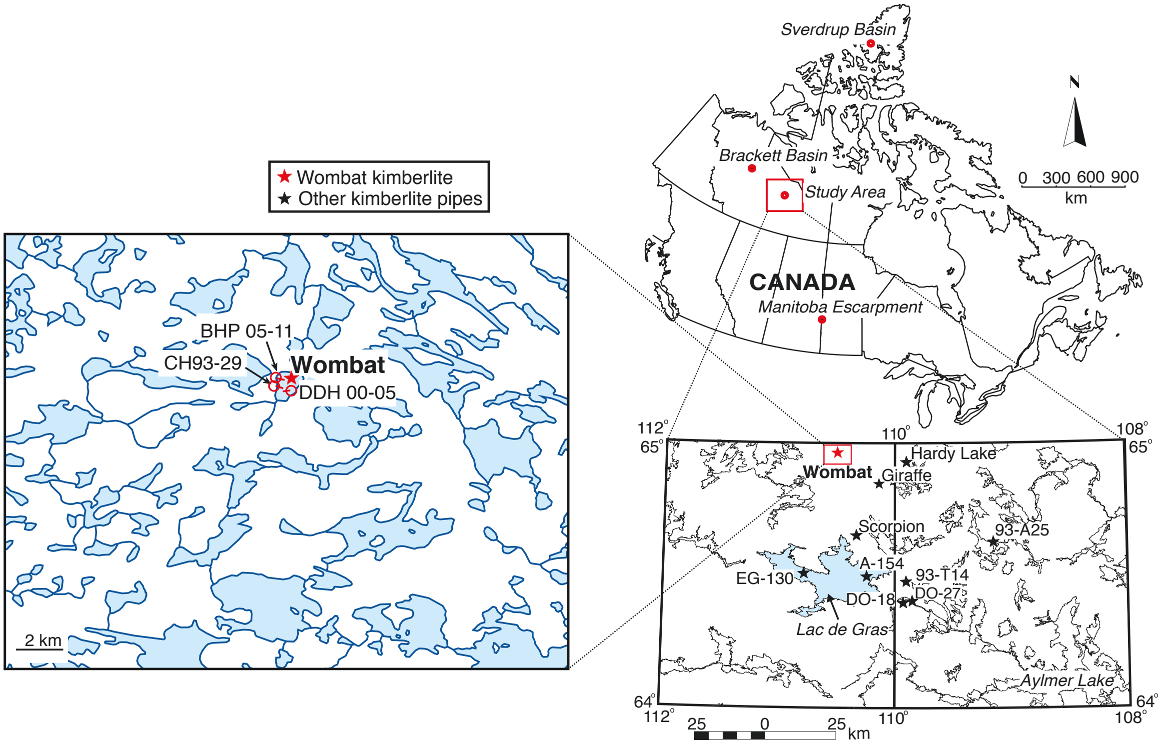

Figure 2.1. Map of the Wombat locality and locations of other kimberlite pipes in the Lac de Gras, Northwest Territories, Canada (adapted from Stasiuk et al., 2002). Azimuths for the Wombat pipe exploration drill cores are indicated by short dashes on the red location symbols.

.

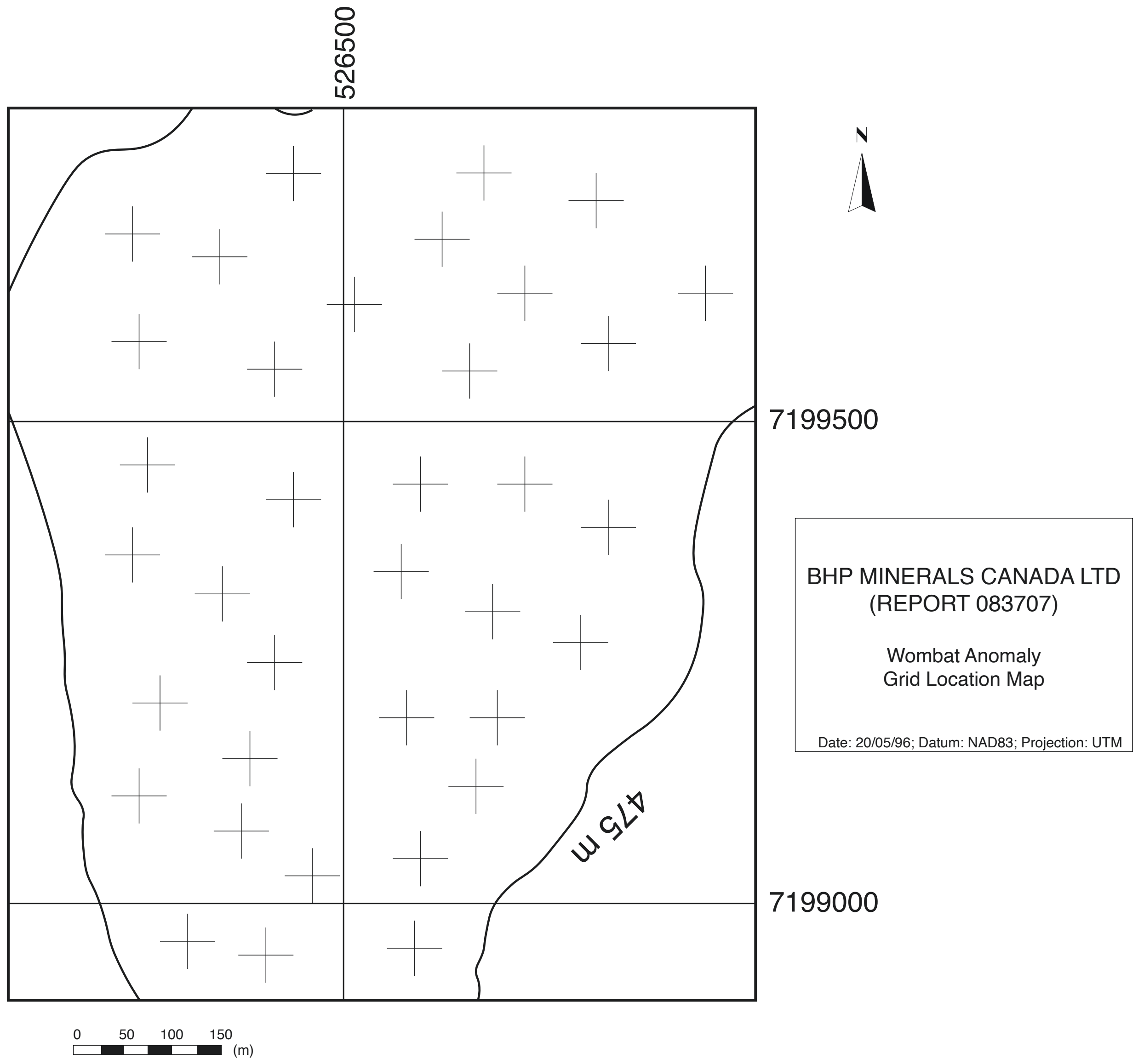

Figure 2.2. Location map of the Wombat gravity anomaly; map coordinates are for UTM zone 13. The 475 m elevation contour is an approximation for the kimberlite anomaly dimensions (after Counts, 1996).

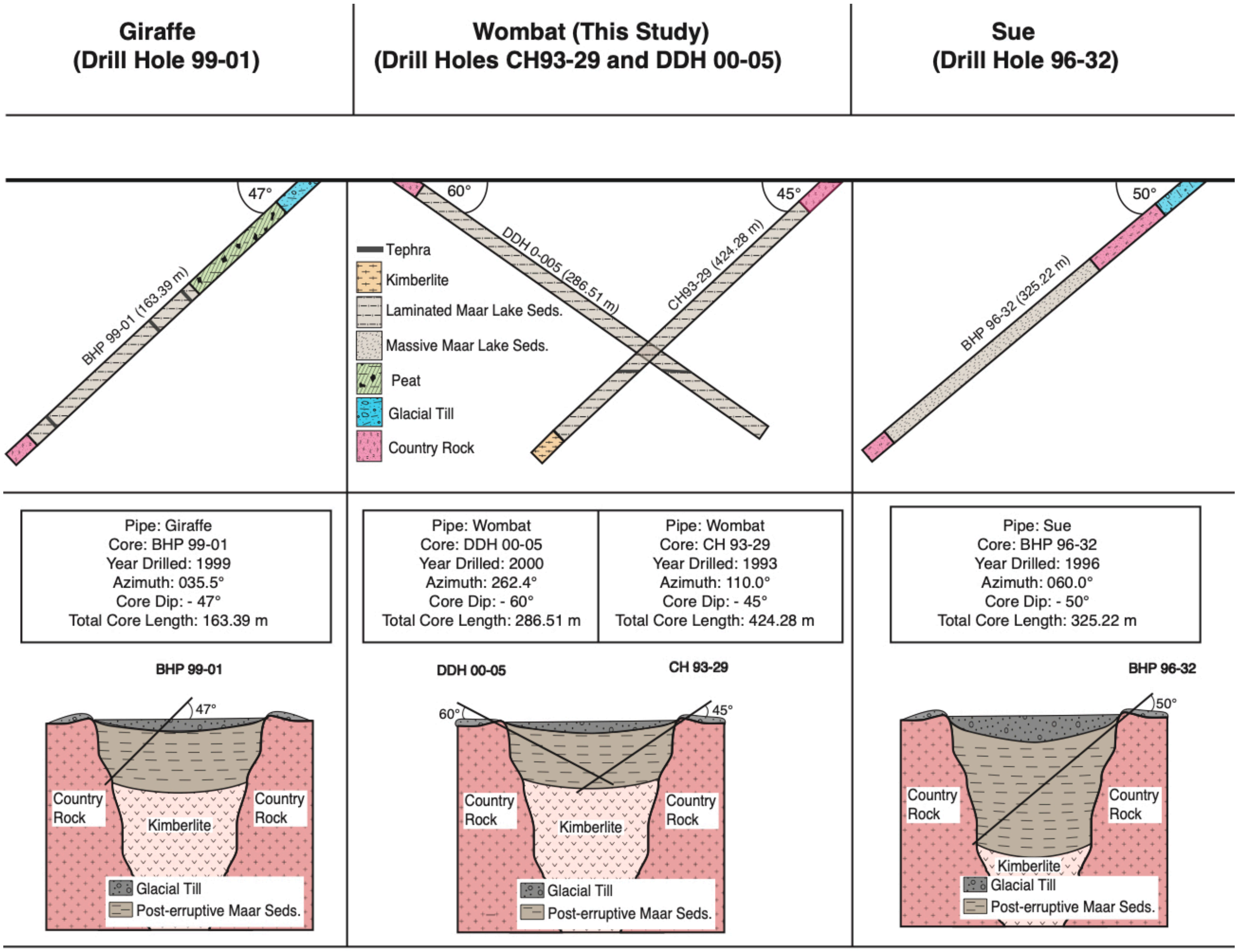

Pipe: Giraffe
Core: BHP 99-01
Year Drilled: 1999
Azimuth: 035.5°
Core Dip: - 47°
Total Core Length: 163.39 m

Pipe: Wombat
Core: DDH 00-05
Year Drilled: 2000
Azimuth: 262.4°
Core Dip: - 60°
Total Core Length: 286.51 m

Pipe: Wombat
Core: CH 93-29
Year Drilled: 1993
Azimuth: 110.0°
Core Dip: - 45°
Total Core Length: 424.28 m

Pipe: Sue
Core: BHP 96-32
Year Drilled: 1996
Azimuth: 060.0°
Core Dip: - 50°
Total Core Length: 325.22 m

Figure 2.3. The schematic representation of stratigraphy and coring details for the Giraffe (BHP 99-01), Wombat (CH93-29 and 00-05) and Sue (96-32) kimberlite bore holes. Kimberlite diatreme diagrams are modified from Hamblin, (2015).

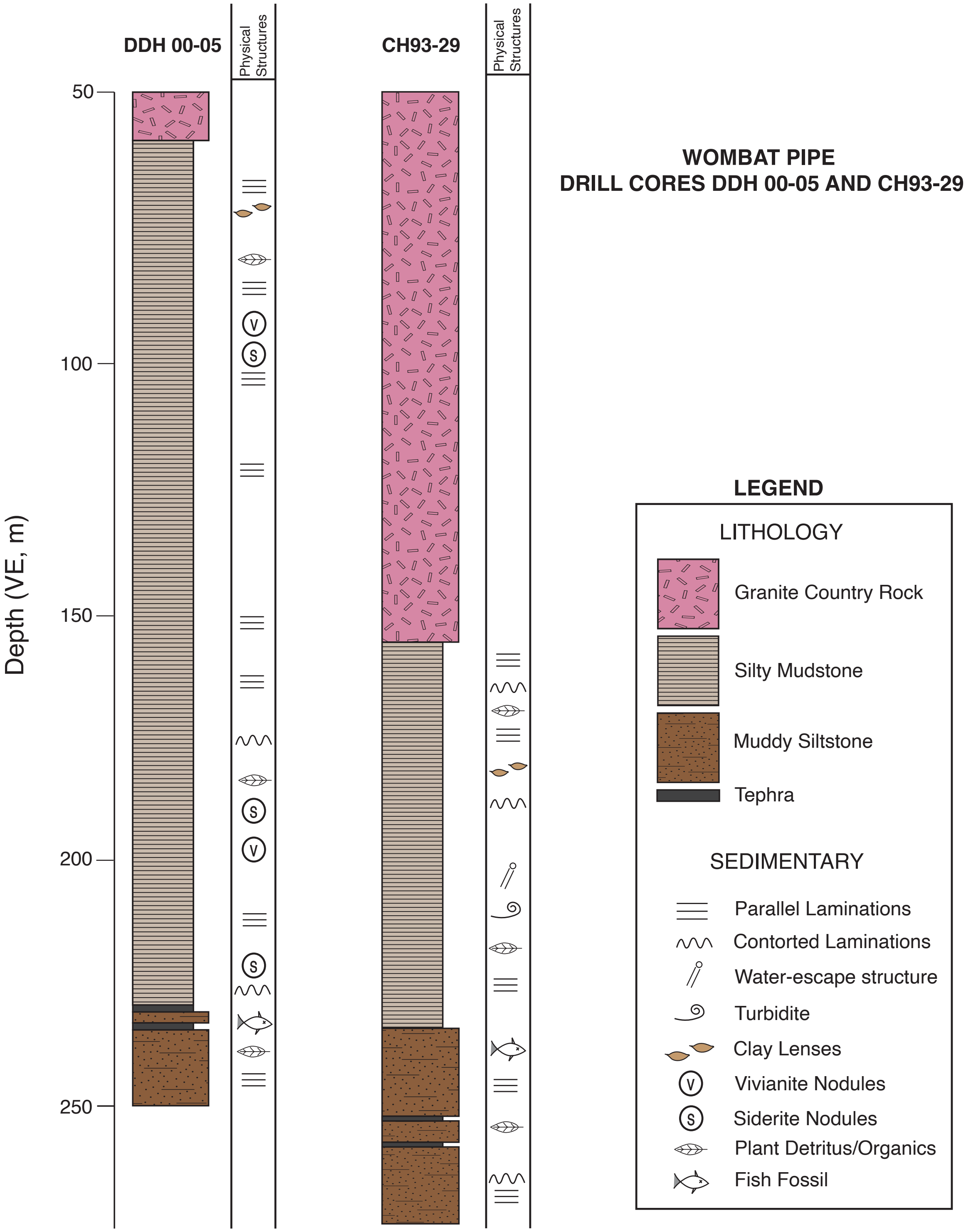

Figure 2.4. Summary stratigraphic logs of the Wombat drill cores DDH 00-05 and CH93-29. Depth in the dipping cores is expressed as vertical equivalent (VE) depth with respect to the surface.

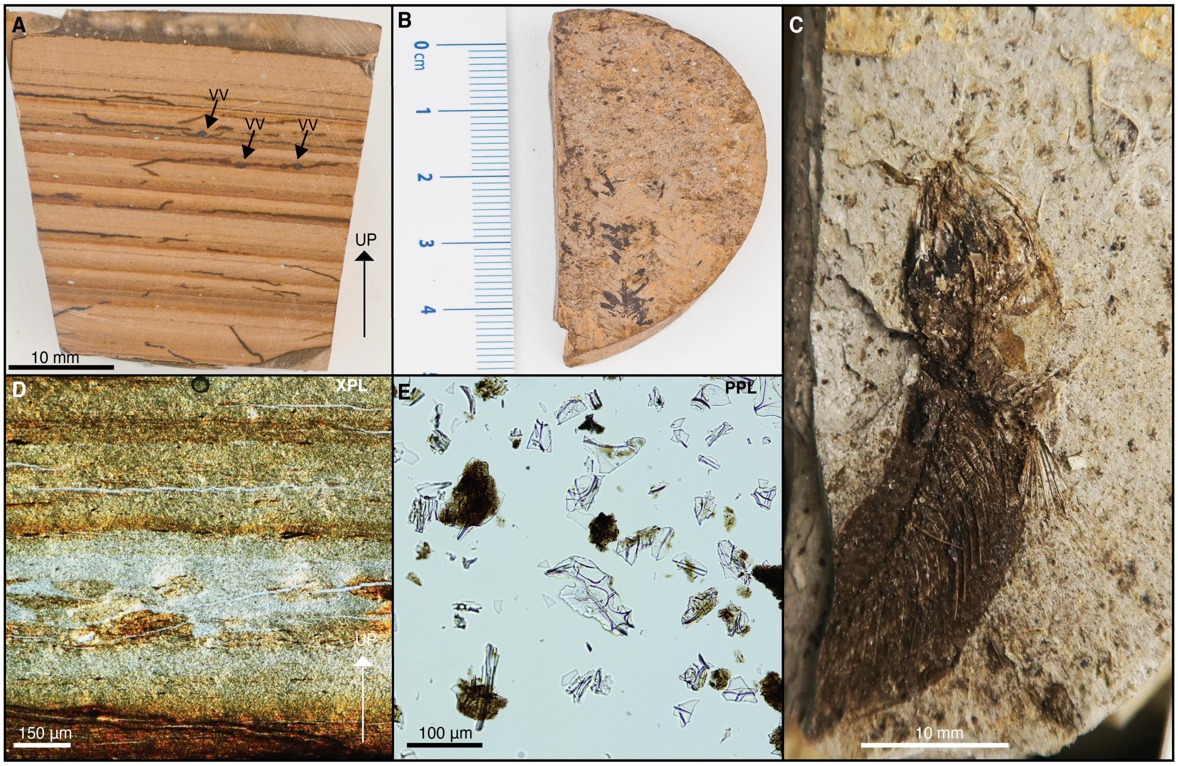

Figure 2.5. Feature of the Wombat pipe maar sediments. A. Representative image of rhythmically laminated sediment from sample 27-1-34 (core depth 207.48 m; V.E. depth 179.7 m; core CH93-29). Arrows indicate vivianite (VV) inclusions and UP arrow indicates younging direction in the core. B. Partially preserved angiosperm leaf fossil from samples 40-3-30 (core depth 274.22 m; V.E. depth 237.5 m; core 00-05). C. Well preserved fish fossil found in core 00-05, box 40 (Photo credit: Dr. Alberto Reyes). D. Cross polarized light (XPL) image of sample 26-1-120 (core depth 201.4 m; V.E. depth174.4 m; core 00-05) indicating heterogeneous nature of lamination within varved sediment. E. Plane polarized light (PPL) image of well-preserved volcanic glass shards from the tephra sample 40-2-110 (core depth 273.43 m; V.E. depth 236.8 m; core 00-05).

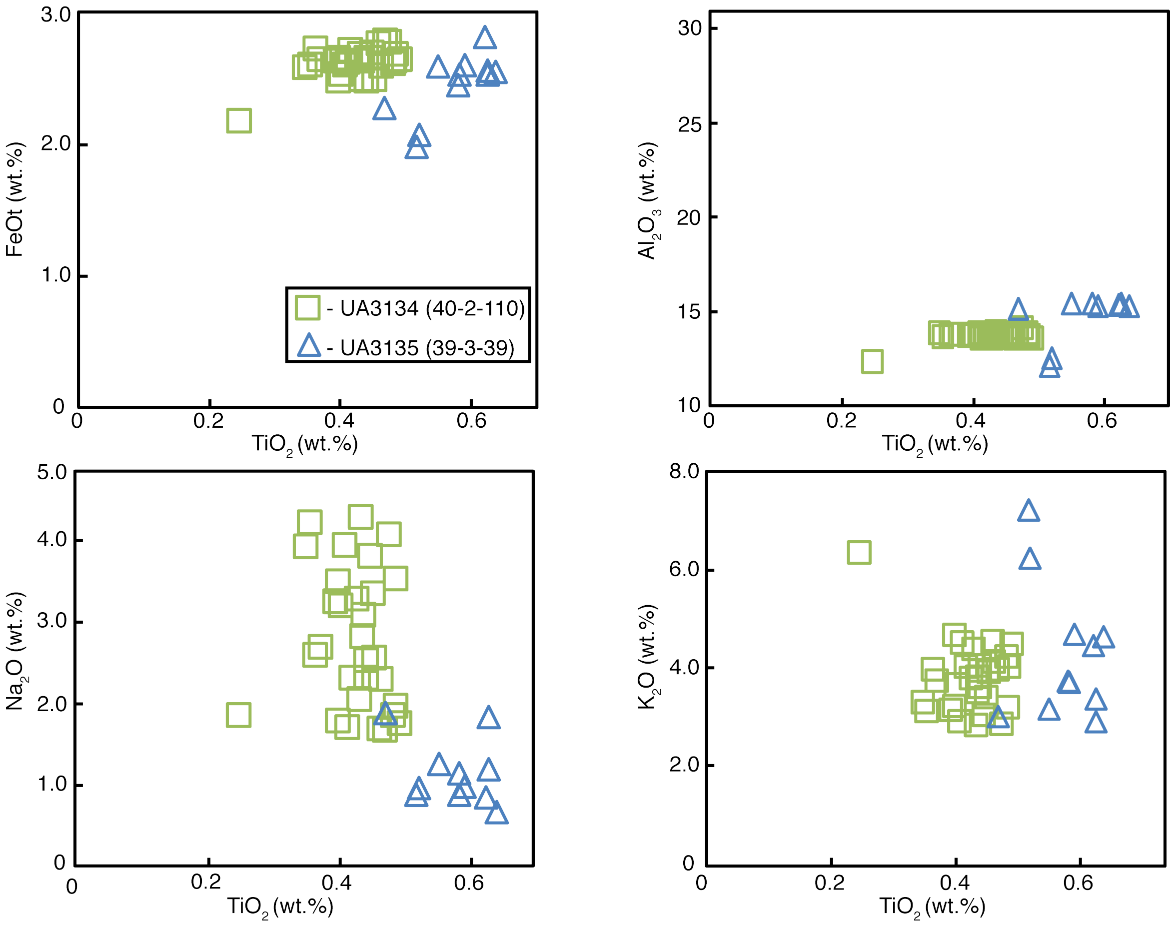

Figure 2.6. Wombat tephra glass major element bivariate plots vs. TiO_2.

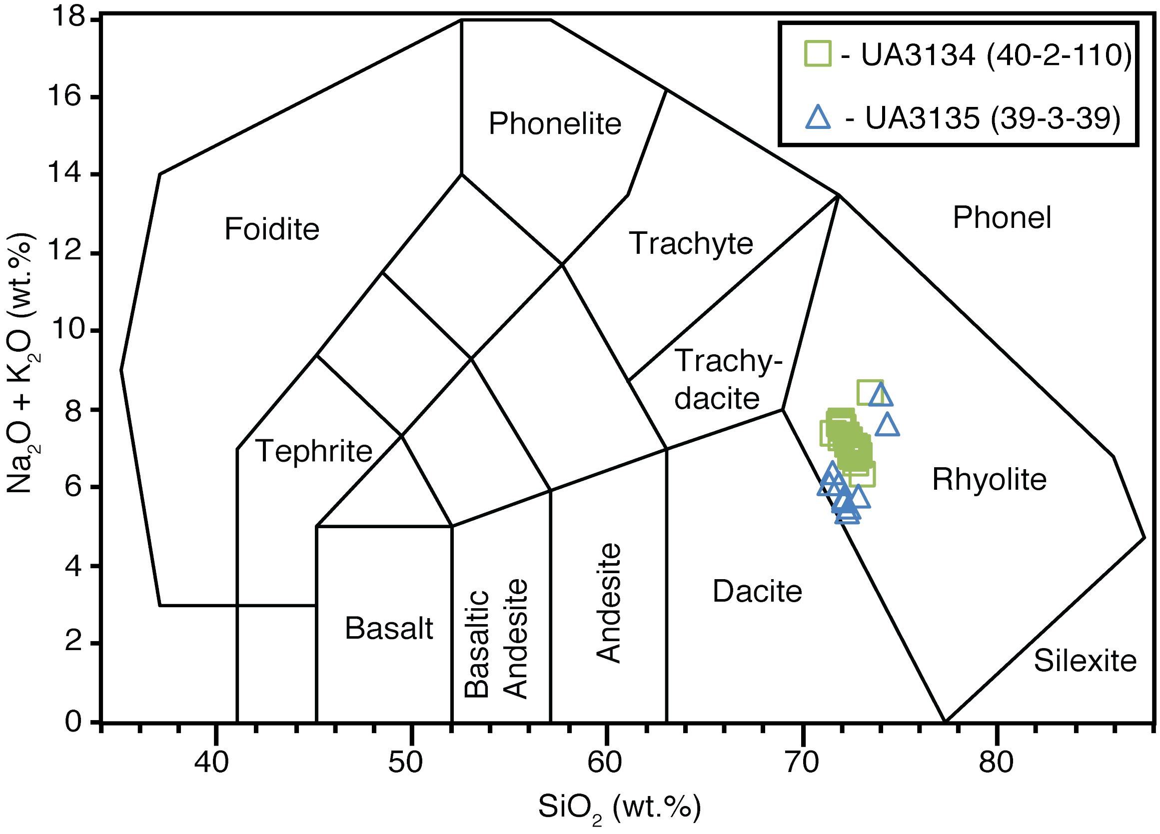

Figure 2.7. Total alkali vs. silica plot, after LeBas et al., (1986), for Wombat pipe tephra glass analyses by electron microprobe.

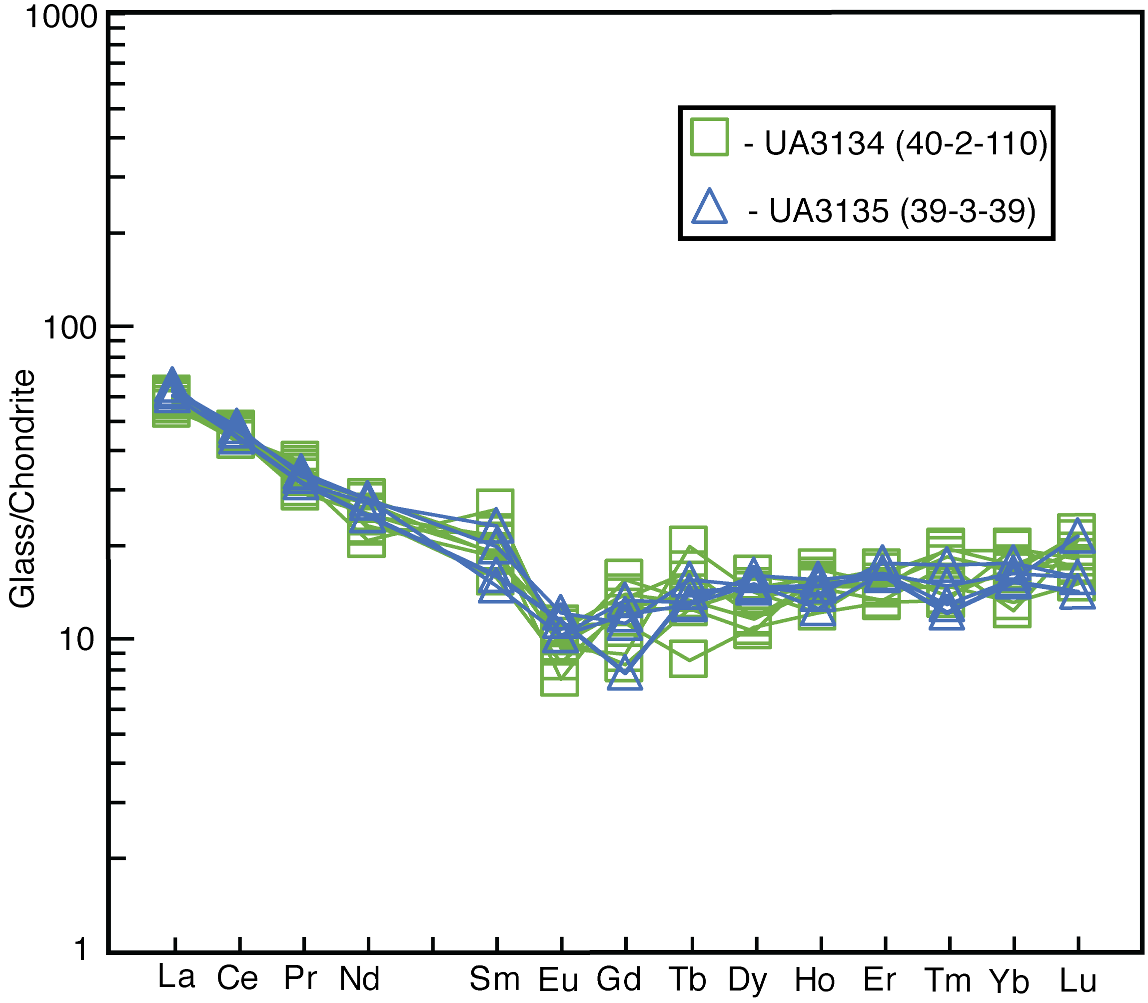

Figure 2.8. Chondrite normalized REE spider diagram of LA-ICP-MS results from Wombat pipe tephra glass, following Sun and McDonough (1989).

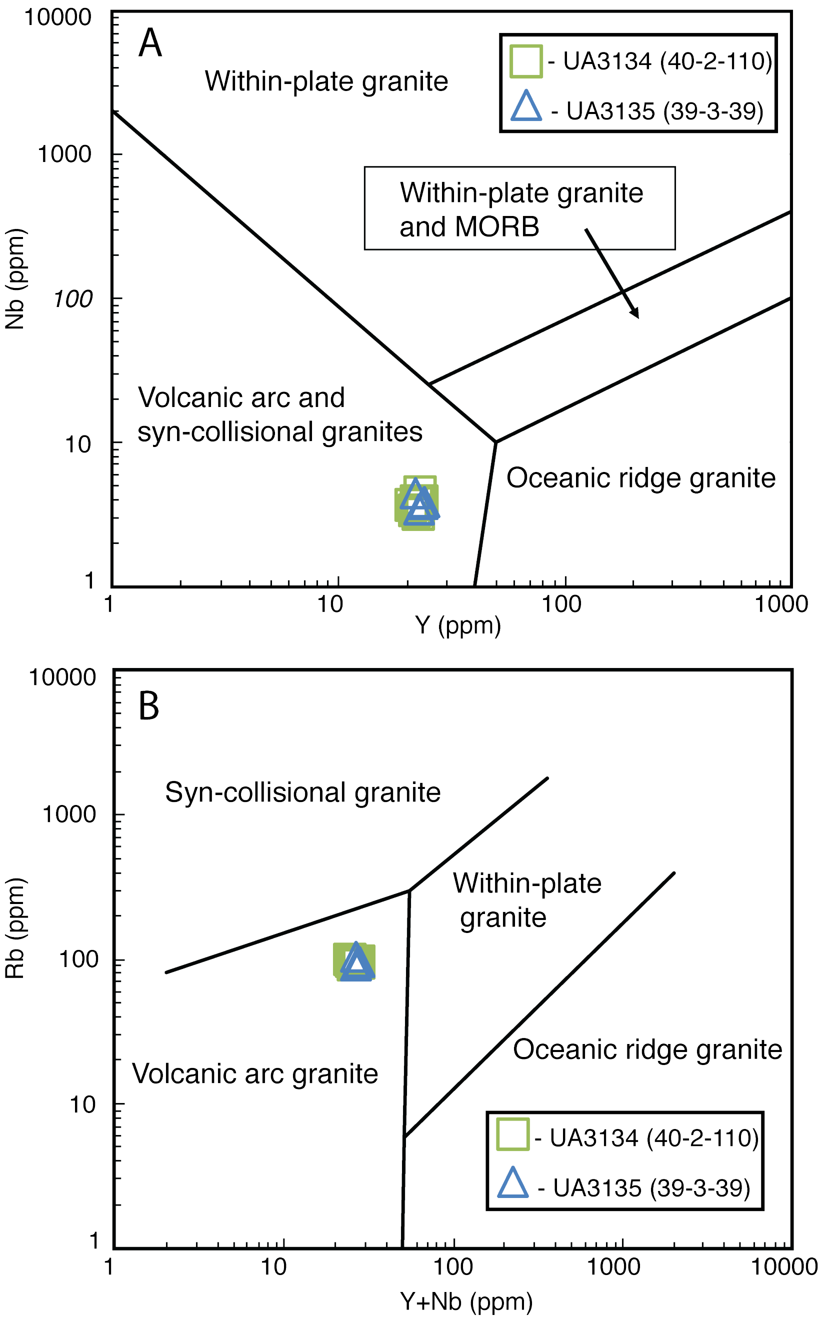

Figure 2.9. Tectnomagmatic discrimination diagrams after Pearce et al., 1984. A) Nb vs. Y diagram with the Wombat samples plotting in the volcanic arc and syn-collisional granites fields. B) Rb vs. Y+Nb diagram depicting a volcanic arc granites trace element signature.

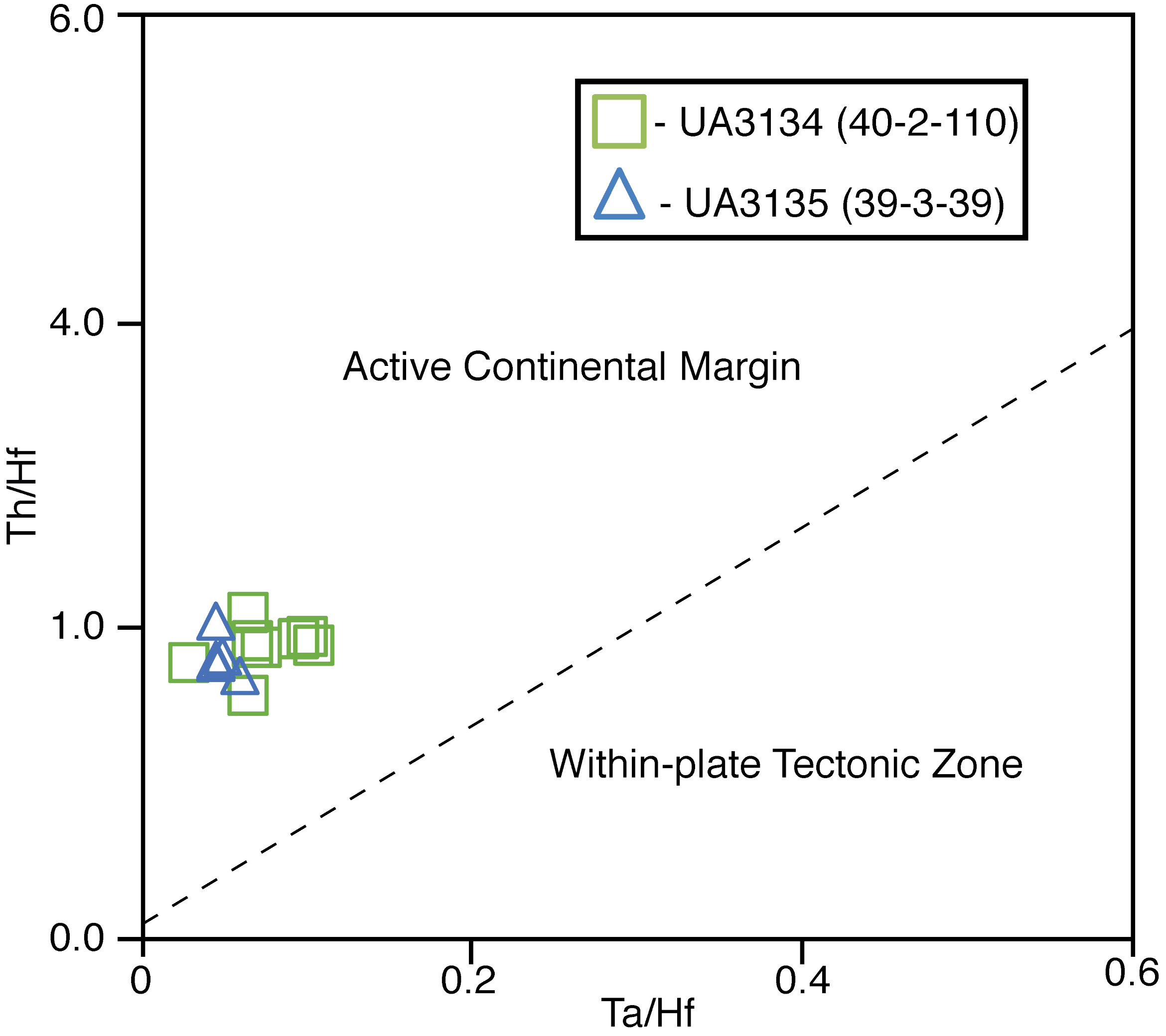

Figure 2.10. Ta/Hf vs Th/Hf tectonic discrimination diagram after Schandl and Gorton (2002), showing the Wombat tephra glasses plotting in the active continental margin field

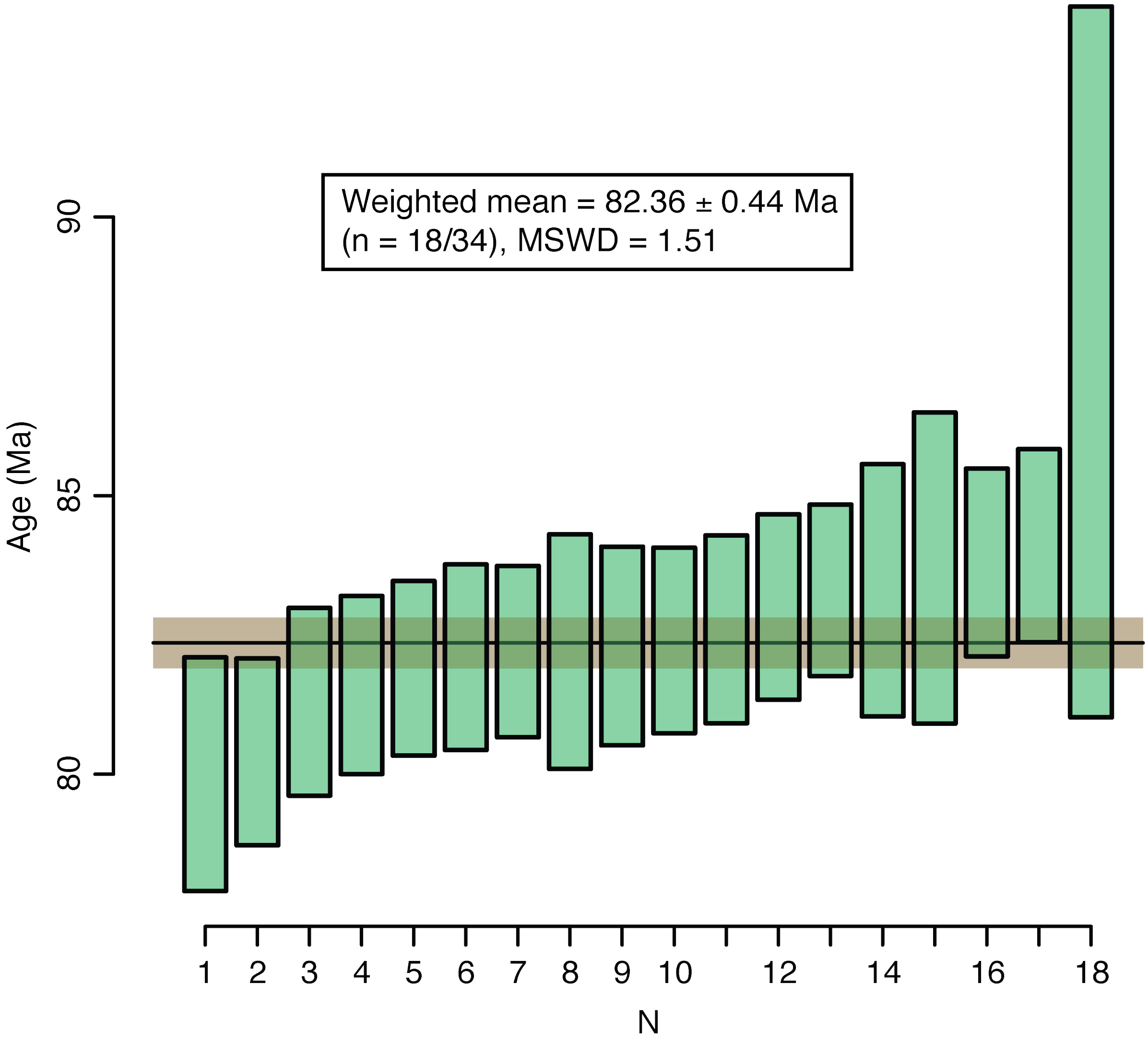

Figure 2.11 Weighted mean plot of $^{206}Pb/^{238}U$ zircon dates for sample UA3135 (39-3-39).

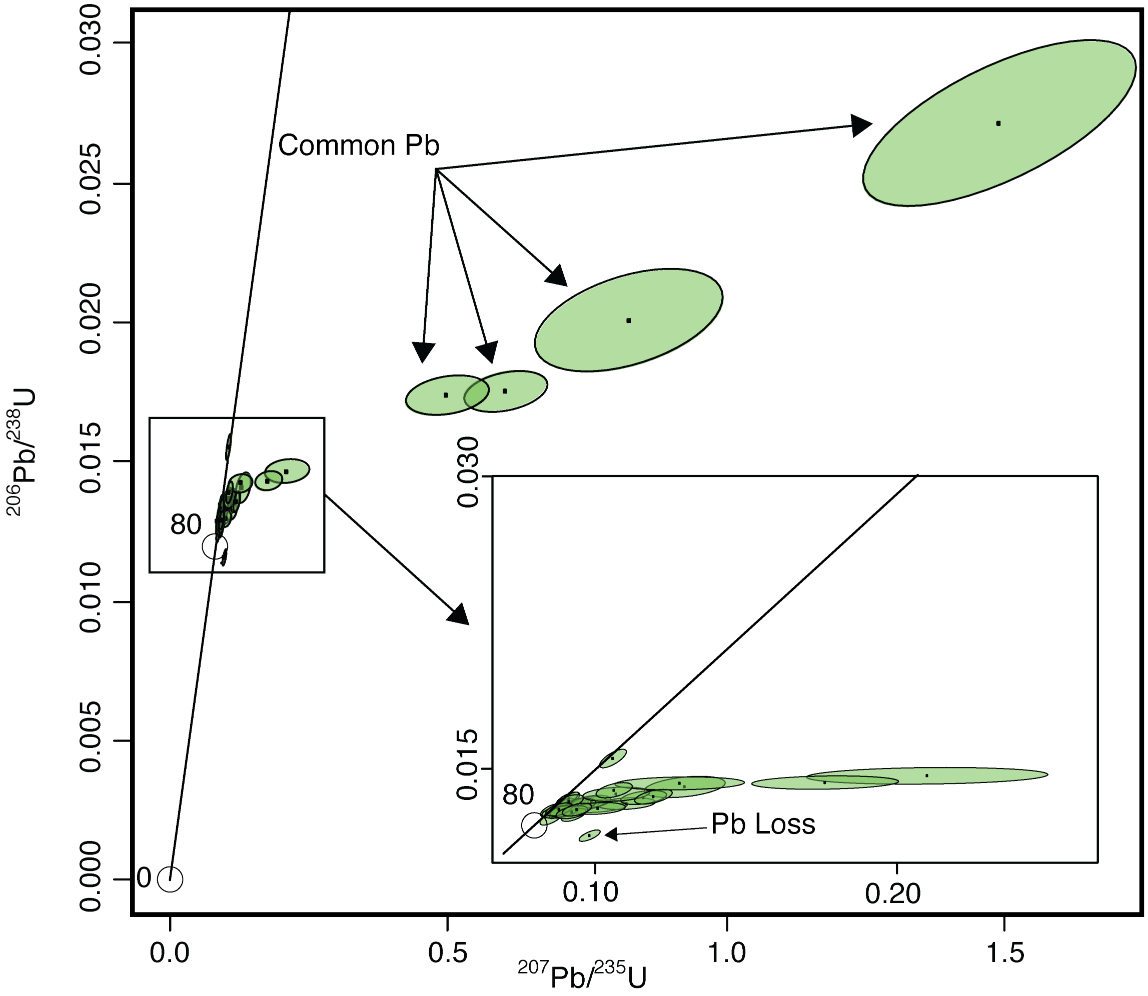

Figure 2.12. Wetherill plot (Wetherill, 1956) of zircon U-Pb results for tephra sample UA3135.

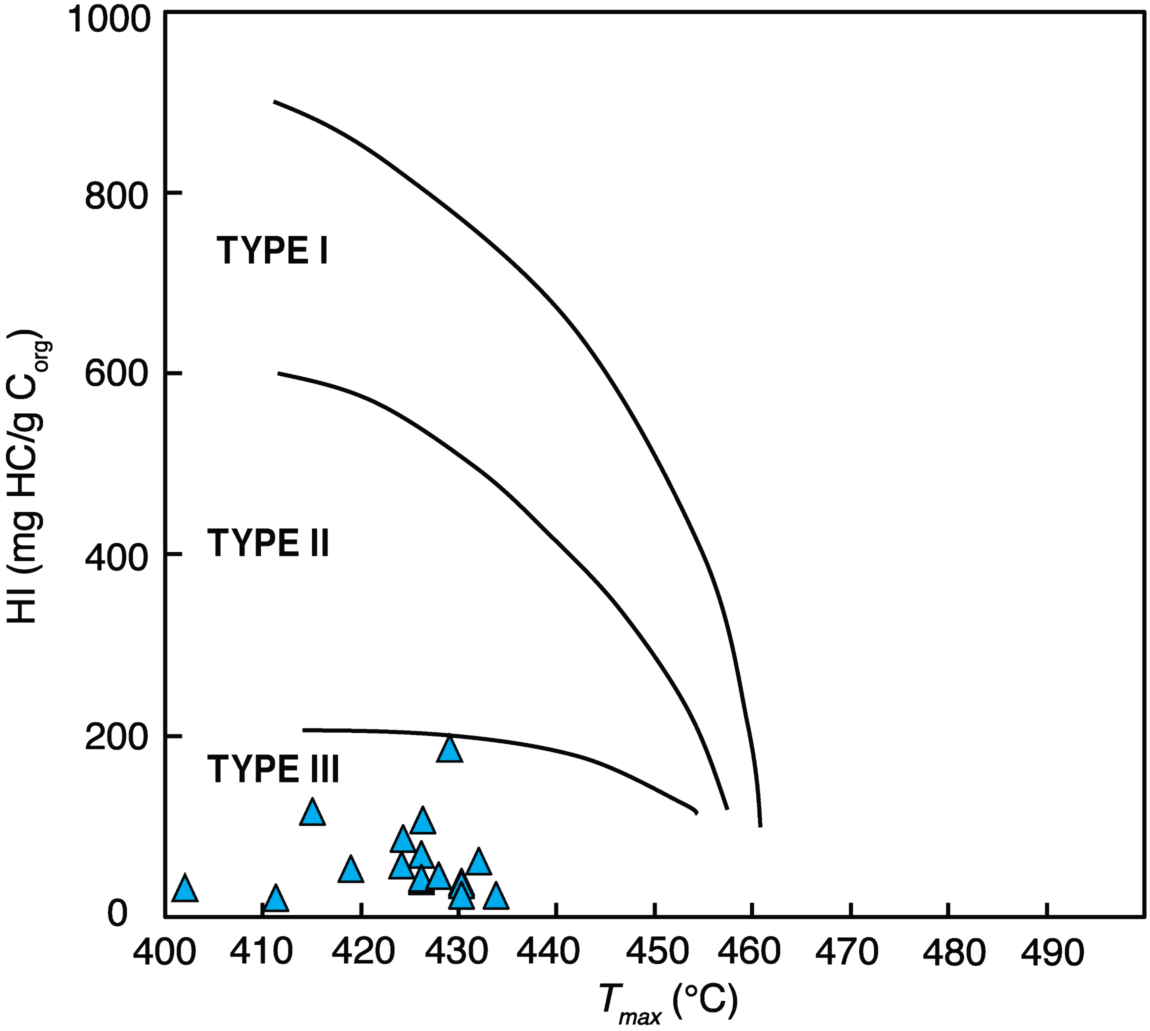

Figure 2.13. Rock Eval pyrolysis HI vs T*max* plot for the Wombat bulk sediment samples (after Espitalié et al., 1984).

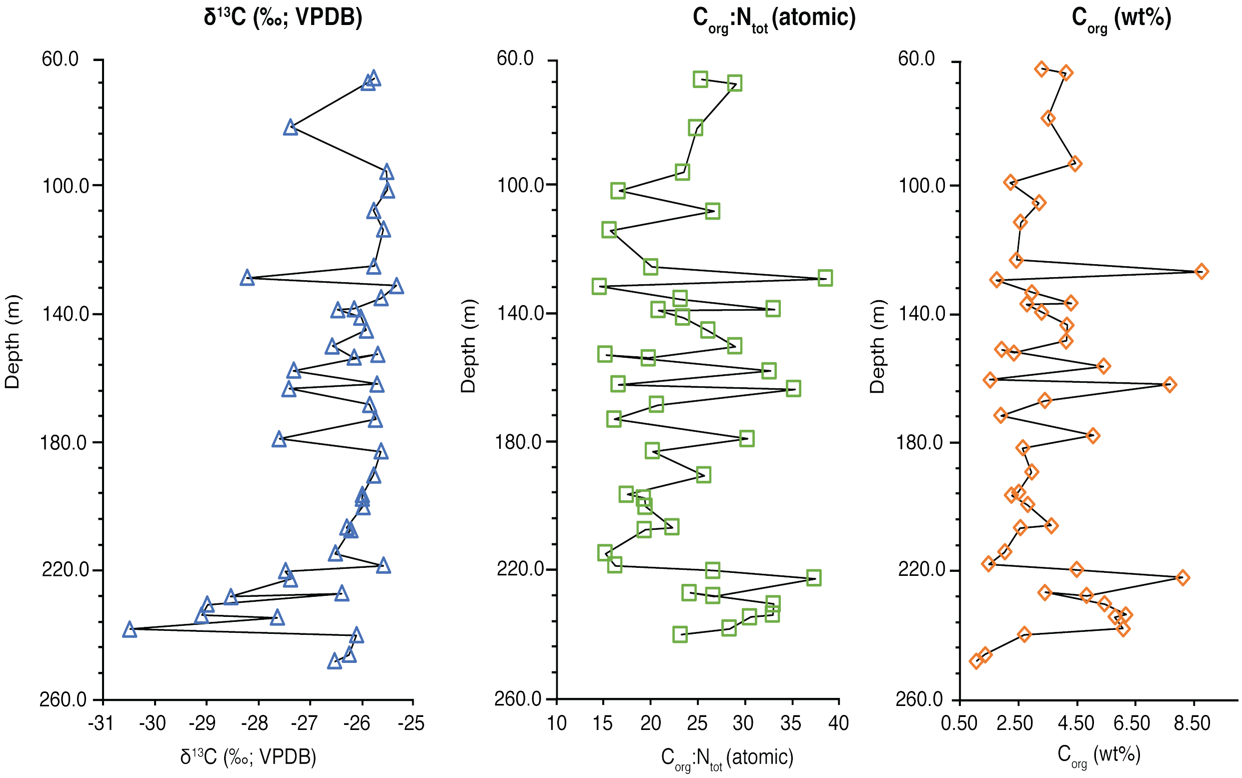

Figure 2.14. Stratigraphic variation in δ^{13}C, atomic C_{org}:N_{tot} and C_{org} for the Wombat pipe maar sediment, plotted as he composite vertical equivalent depth profile of drill cores CH93-29 and 00-05.

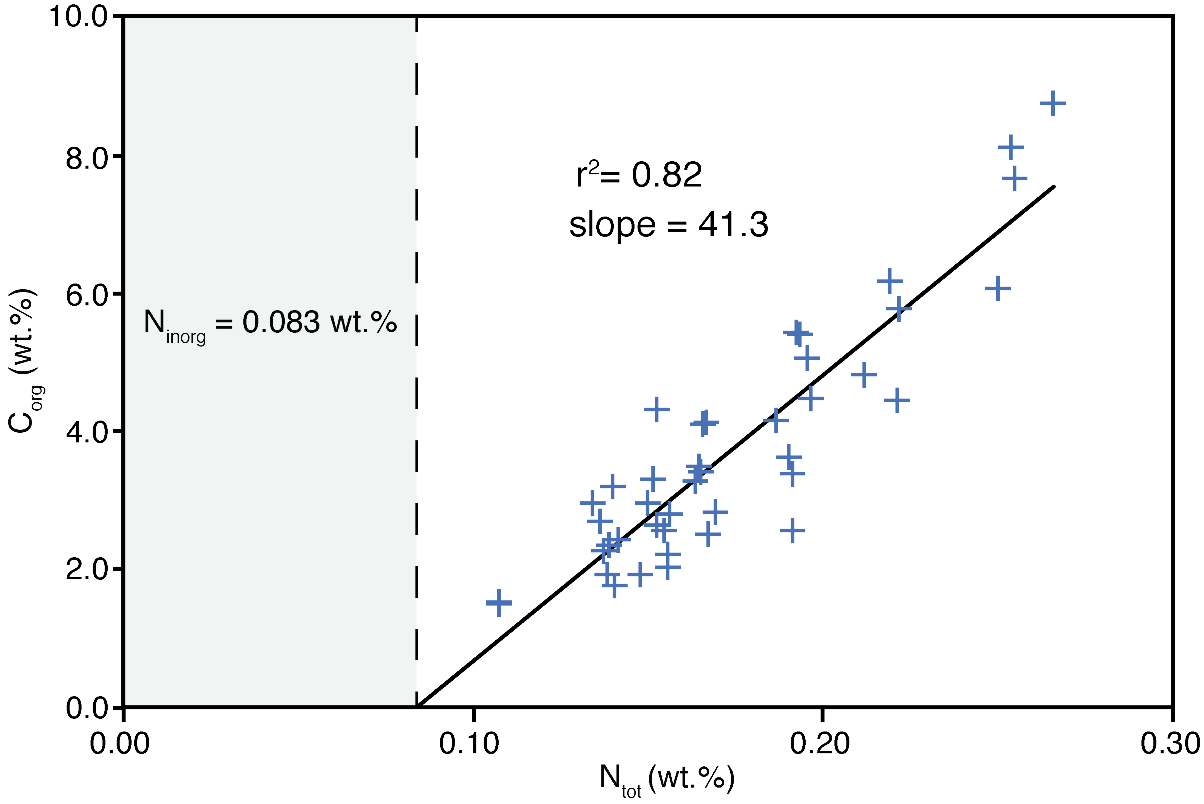

Figure 2.15. N_{tot} vs C_{org} for Wombat pipe bulk sediment. The shaded area depicts contribution of inorganic nitrogen to the total nitrogen with a positive intercept ~ 0.083 wt.%.

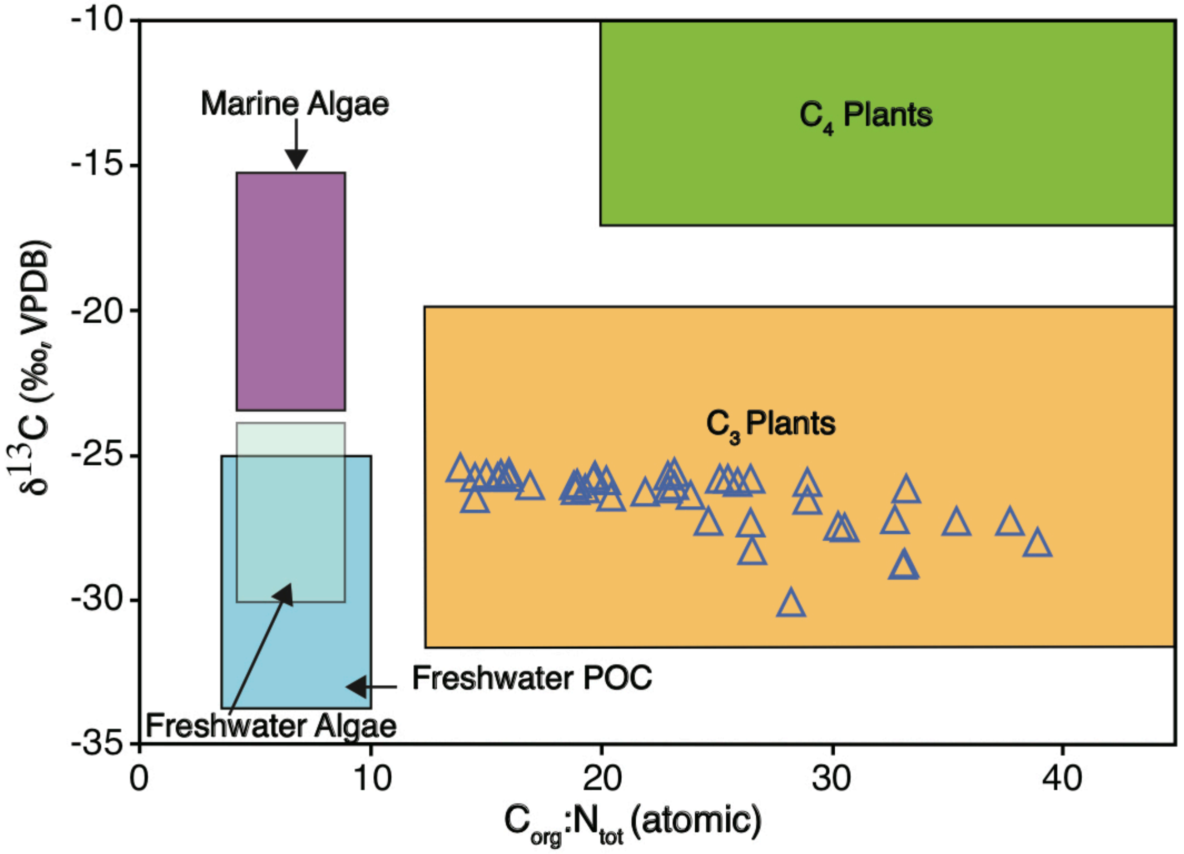

Figure 2.16. C_{org}:N_{tot} and $\delta^{13}C$ organic matter source combinations showing the Wombat samples plotting in a C_3 land plants field (after Meyers, 1994; Lamb et al., 2006).

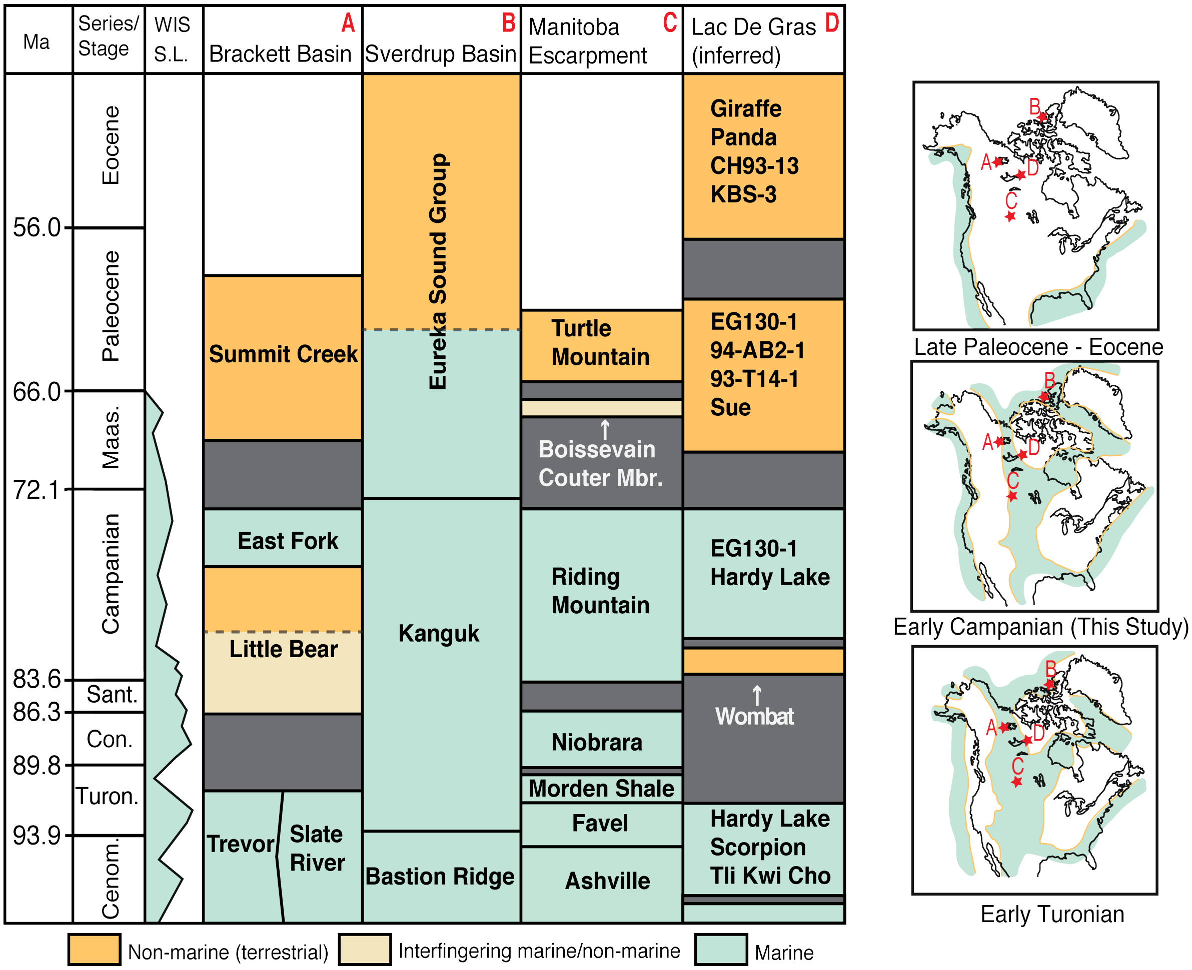

Figure 2.17. Western Interior Seaway paleogeography and schematic Cenomanian to Eocene stratigraphy for the Brackett Basin, Sverdrup Basin, Manitoba Escarpment and inferred stratigraphy for the Lac de Gras region. WIS S.L. = Western Interior Seaway sea level variation (Schröder-Adams, 2014). The stratigraphy is adapted from Sweet et al., 2003 and paleogeography of WIS is adapted from Schröder-Adams, 2014 and references therein. Additional sedimentary xenolith and maar lake sedimentary fill data from Nassichuk and McIntyre, 1995; McKinlay et al., 1998; Stasiuk et al., 2002; Stasiuk et al., 2006.

CHAPTER 3. CONCLUSION

3.1 THESIS SUMMARY

Maar lake sedimentary records from Lac de Gras kimberlites provide rare glimpses of ancient paleoenvironments in subarctic Canada. These records potentially represent the only preserved and intact evidence of now-eroded sedimentary rocks for a broad swath of northern Canada that essentially lacks any pre-Late Quaternary Phanerozoic sedimentary record.

The work presented in this thesis addressed two fundamental questions regarding a relatively unstudied sedimentary record from the Wombat kimberlite pipe, which comprises over 195 m of fine-grained, laminated post-eruptive sedimentary fill: (1) what is the age of this sediment sequence?, and (2) what is the broad paleoenvironmental context for this sediment sequence? A distal rhyolitic tephra in the Wombat maar sediments was dated by zircon U-Pb methods to 82.36 ± 0.44 Ma, providing a minimum age for emplacement of the Wombat pipe and a close constraining age for the onset of maar lake sedimentation. A major implication is that Wombat pipe is thus the only kimberlite in the Lac De Gras region that predates 80 Ma (except the Carboniferous Eddie kimberlite), which implies that other older pipes maybe present in the region. This work also demonstrates that geochronology on post-eruptive sediments may be a valuable tool for determining kimberlite emplacement ages when traditional methods on primary kimberlitic mineral phases are unsuccessful. In addition to the direct geochronology of the Wombat sediments, the tephra beds interbedded in the maar sediments are potential correlatives to distal tephras in other high-latitude sedimentary records.

Results of bulk sediment geochemical analyses through the Wombat post-eruptive sediment fill indicate that the maar lake setting is likely a small, monomictic or meromictic lake situated in a relatively warm terrestrial environment during Late Creatceous. Anoxic bottom water conditions in the Wombat maar lake contributed to excellent preservation of freshwater microfossils, fully articulated fish fossils, and plant detritus. This study presents the second detailed description of maar lake deposit in Canada, with the first one recovered from the middle Eocene Giraffe kimberlite maar located ~ 20 km NW of the Wombat locality. The Wombat maar sediments complement limited information on Slave Craton paleoenvironments derived from xenoliths of now-eroded Mesozoic cover rock in Lac de Gras kimberlites. When considered with the stratigraphic framework of Late Cretaceous sedimentary rocks elsewhere in midcontinent Canada, results presented here provide new insight on Lake Cretaceous and Paleogene paleogeography of a data-poor region of the Western Interior Seaway.

3.2 FUTURE WORK

From the results of this study it is clear that kimberlitic maar lake deposits have strong potential for developing paleoenvironment, tectonic, paleogeographic, and paleontological records on the Canadian Shield. However, much more work is needed to fully understand these extraordinary sedimentary archives. This study provides a first glance at the depositional setting of the Wombat maar lake. The geochronological approach used in this study can be potentially applied to all pre-Quaternary lake deposits that contain deposits of tephra or bentonite in the sedimentary sequence. However, the Wombat kimberlite still requires clarification on the age of emplacement by dating primary minerals derived from the primary kimberlite samples. This will require more scientific drilling to obtain needed kimberlite samples and additional maar sediments.

The bulk geochemical analysis of the sediment provides valuable information on the depositional environment that persisted during maar sedimentation, with the key point from this work being the excellent preservation of organic material. New pollen analyses of the Wombat maar sediments is in process, with potential for quantitative paleoclimate reconstruction based on modern analogue techniques. A related focus of future work should be analysis of biomarkers such as leaf waxes and other lipids, which have yielded independent quantitative paleoclimate estimates in the nearby Giraffe kimberlite pipe. Furthermore, due to the excellent preservation conditions of the Wombat maar sediments, there is excellent potential for paleontological research of the Late Cretaceous flora and fauna in Lac de Gras during this time. The varved nature of the sediment has potential for future sedimentological research on sedimentation rates and further geochemical analysis of annually resolved mass accumulation rates of important elements (e.g. mercury). The research provided in this thesis gives the first detailed description of the geochronology and broad paleoenvironmental reconstruction of the Wombat maar, but much more work is required to fully understand this unique sedimentary archive.

BIBLIOGRAPHY

Amiot, R., Lécuyer, C., Buffetaut, E., Fluteau, F., Legendre, S., & Martineau, F. (2004). Latitudinal temperature gradient during the Cretaceous Upper Campanian–Middle Maastrichtian: δ18O record of continental vertebrates. Earth and Planetary Science Letters, 226(1-2), 255-272.

Ault, A. K., Flowers, R. M., and Bowring, S. A., 2013, Phanerozoic surface history of the Slave craton. Tectonics, v. 32(5), p. 1066-1083, doi: 10.1002/tect.20069.

Bacon, C. R., Foster, H. L., & Smith, J. G., 1990, Rhyolitic calderas of the Yukon-Tanana Terrane, east central Alaska: Volcanic remnants of a Mid-Cretaceous magmatic arc. Journal of Geophysical Research: Solid Earth, 95(B13), 21451-21461.

Balkwill, H. R. (1978). Evolution of Sverdrup basin, arctic Canada. AAPG Bulletin, 62(6), 1004-1028.

Barron, Eric J. "A warm, equable Cretaceous: the nature of the problem." Earth-Science Reviews 19.4 (1983): 305-338.

BAS, M. L., Maitre, R. L., Streckeisen, A., Zanettin, B., & IUGS Subcommission on the Systematics of Igneous Rocks. (1986). A chemical classification of volcanic rocks based on the total alkali-silica diagram. Journal of petrology, 27(3), 745-750.

Bell, R. 1895. A great pre-glacial river in northern Canada. Scottish Geographical Magazine, 11: 368

Benson, Mary Ellen, J. Patrick Kociolek, and Bibliotheca Diatomologica. "Freshwater diatom floristics of the late Eocene Florissant Formation, Clare's Quarry site, central Colorado, USA." (2012): 1-136.

Bergman, S. C., Akinin, V. V., Decker, J., Miller, E. L., & Layer, P. (2006, May). North Alaska Upper Cretaceous tephra: Eurasian or North American source calderas. In 102nd Annual Meeting of the Cordilleran Section, GSA, 81st Annual Meeting of the Pacific Section, AAPG, and the Western Regional Meeting of the Alaska Section, SPE (pp. 8-10).

Bono, R., Tarduno, J., & Singer, B. (2013, April). Cretaceous magmatism in the High Canadian Arctic: implications for the nature and age of Alpha Ridge. In EGU General Assembly Conference Abstracts (Vol. 15).

Bowring, S. A., and Williams, I. S., 1999, Priscoan (4.00–4.03 Ga) orthogneisses from northwestern Canada: Contributions to Mineralogy and Petrology, v. 134(1), p. 3-16, doi:10.1007/s004100050465.

Büchel, G. (1993). Maars of the Westeifel, Germany. In Paleolimnology of European maar lakes (pp. 1-13). Springer, Berlin, Heidelberg.

Carlson, J.A., Kirkley, M.B., Thomas, E.M. and Hillier, W.D., 1998. Recent major kimberlite discoveries in Canada. In Extended Abstracts, Seventh International Kimberlite Conference, p. 127-131.

Cecil, M. R., Gehrels, G., Ducea, M. N., & Patchett, P. J. (2011). U-Pb-Hf characterization of the central Coast Mountains batholith: Implications for petrogenesis and crustal architecture. Lithosphere, 3(4), 247-260.

Chacón-Baca, E., Beraldi-Campesi, H., Cevallos-Ferriz, S. R. S., Knoll, A. H., & Golubic, S. (2002). 70 Ma nonmarine diatoms from northern Mexico. *Geology*, *30*(3), 279-281.

Counts B.A., 1996, Geochemical, Geophysical and Drill Hole Report of the A, B, C, D, E, F, M, T, W, AM, ED, FH and GO Claims Mackenzie, Report 083707.

Colinvaux, P. A. (1964). The environment of the Bering land bridge. Ecological Monographs, 34(3), 297-329.

Cookenboo, H. O., Orchard, M. J., and Daoud, D. K., 1998, Remnants of Paleozoic cover on the Archean Canadian Shield: limestone xenoliths from kimberlite in the central Slave craton: Geology, v. 26(5), p. 391-394, doi:10.1130/00917613(1998)026<0391:ROPCOT>2.3.CO;2.

Creaser, R. A., Grütter, H., Carlson, J., and Crawford, B., 2004, Macrocrystal phlogopite Rb–Sr dates for the Ekati property kimberlites, Slave Province, Canada: evidence for multiple intrusive episodes in the Paleocene and Eocene: Lithos, v. 76(1-4), p. 399-414, doi: 10.1016/j.lithos.2004.03.039.

Davis, W. J., Schroeder-Adams, C. J., Galloway, J. M., Herrle, J. O., & Pugh, A. T. (2017). U–Pb geochronology of bentonites from the Upper Cretaceous Kanguk Formation, Sverdrup Basin, Arctic Canada: constraints on sedimentation rates, biostratigraphic correlations and the late magmatic history of the High Arctic Large Igneous Province. Geological Magazine, 154(4), 757-776.

Deines, P. (1980). The isotopic composition of reduced organic carbon. Handbook of environmental isotope geochemistry.

Dixon, J. (1996). Geological atlas of the Beaufort-Mackenzie area; Geological Survey of Canada. Miscellaneous report.

Dixon, J. 1999. Mesozoic-Cenozoic stratigraphy of the northern interior plains and plateaux, Northwest Territories. Geological Survey of Canada Bulletin, 536, 56 p.

Duk-Rodkin, A., & Hughes, O. L. (1994). Tertiary-Quaternary drainage of the pre-glacial Mackenzie Basin. Quaternary International, 22, 221-241.

Embry, A., & Beauchamp, B. (2019). Sverdrup basin. In The sedimentary basins of the United States and Canada (pp. 559-592). Elsevier.

Estrada S and Henjes-Kunst F (2004) Volcanism in the Canadian High Arctic related to the opening of the Arctic Ocean. Zeitschrift der Deutschen Geologischen Gesellschaft 154, 579–603.

Estrada S and Henjes-Kunst F (2013) 40Ar–39Ar and U–Pb dating of Cretaceous continental rift-related magmatism on the northeast Canadian Arctic margin. Zeitschrift der Deutschen Gesellschaft für Geowissenschaften 164, 107–30.

Espitalié, J., Marquis, F., & Barsony, I. (1984). Geochemical logging. In Analytical pyrolysis (pp. 276-304). Butterworth-Heinemann.

Farooqui, A., Aggarwal, N., Jha, N., & Phartiyal, B. (2015). Oldest record of freshwater diatom frustules in tests of Permian thecamoebians: faithfulness of sedimentary record. International Journal of Current Microbiology and Applied Sciences, 4, 472-485.

Field, M. And Scott Smith, B.H., 1998. Contrasting geology and near-surface emplacement of kimberlite pipes in southern Africa and Canada. In Proceedings of the Seventh

International Kimberlite Conference, I.J. Gurney, J.L. Gurney, M.D. Pascoe and S.H. Richardson (eds.), Capetown, v. 1, p. 214-237.

Freudenthal, T., Wagner, T., Wenzhöfer, F., Zabel, M., & Wefer, G. (2001). Early diagenesis of organic matter from sediments of the eastern subtropical Atlantic: evidence from stable nitrogen and carbon isotopes. Geochimica et Cosmochimica Acta, 65(11), 1795-1808.

Frey, D. G. (1988). What is paleolimnology?. Journal of Paleolimnology, 1(1), 5-8.

Gaschnig, Richard M., et al., "Migrating magmatism in the northern US Cordillera: in situ U–Pb geochronology of the Idaho batholith." Contributions to Mineralogy and Petrology 159.6 (2010): 863-883.

Gaschnig RM, Vervoort JD, Lewis RS and McClelland WC (2010) Migrating magmatism in the northern US Cordillera: in situ U–Pb geochronology of the Idaho batholith. Contributions to Mineralogy and Petrology 159, 863–83.

Goolaerts, A., Mattielli, N., de Jong, J., Weis, D., & Scoates, J. S., 2004, Hf and Lu isotopic reference values for the zircon standard 91500 by MC-ICP-MS. Chemical Geology, 206 (1-2), 1-9.

Hamblin, A. P., Stasiuk, L. D., Sweet, A. R., Lockhart, G. D., Dyck, D. R., Jagger, K., & Snowdon, L. R. (2003, June). Post-kimberlite Eocene strata within a crater basin, Lac de Gras, Northwest Territories, Canada. In International Kimberlite Conference: Extended Abstracts (Vol. 8).

Hamblin, A.P., 2015. An Eocene post-kimberlite maar lake: lacustrine oil-shale crater-fill deposits, Lac de Gras 1129 area, Northwest Territories, Canada; Geological Survey of Canada, Open File 7809, 26 p. 1130 doi:10.4095/296430

Harwood, D. M., Nikolaev, V. A., & Winter, D. M. (2007). Cretaceous records of diatom evolution, radiation, and expansion. The Paleontological Society Papers, 13, 33-59.

Hay, W. W. (1995). Paleoceanography of marine organic-carbon-rich sediments.

Heaman, L. M., Kjarsgaard, B. A., and Creaser, R. A., 2004, The temporal evolution of North American kimberlites: Lithos, v. 76(1-4), p. 377-397, doi: 10.1016/j.lithos.2004.03.047.

Herendeen, P. S., & Jacobs, B. F. (2000). Fossil legumes from the middle Eocene (46.0 Ma) Mahenge flora of Singida, Tanzania. American Journal of Botany, 87(9), 1358-1366.

Hollander, D. J., & Smith, M. A. (2001). Microbially mediated carbon cycling as a control on the δ13C of sedimentary carbon in eutrophic Lake Mendota (USA): new models for interpreting isotopic excursions in the sedimentary record. Geochimica et Cosmochimica Acta, 65(23), 4321-4337.

Hu, S., Hickey, L., Siver, P. A., and Wolfe, A. P., 2011, Palynology and age of post–eruptive lake sediments from the Wombat kimberlite locality, Northwest Territories, Canada: Geological Society of America Abstracts with Programs, v. 43, no. 5, p. 157.

Kjarsgaard, B. A., 2001 Lac de Gras Kimberlite Field, Slave Province, 1: 250,000 geology map and descriptive notes: Geological Survey of Canada, Open-File Report 3238.

Kjarsgaard, B.A., Wilkinson, L. and Armstrong, J., 2002., Geology, Lac de Gras

Kimberlite Field, central Slave Province, Northwest Territories – Nunavut: Geological Survey of Canada, Open File Report 3238, 1 CD.

Kemp, K. M. (1994). Tephrostratigraphy of the Late Cretaceous Kanguk Formation, Banks Island, Arctic Canada (Northwest Territories).

Klepeis, K. A., Crawford, M. L., & Gehrels, G. (1998). Structural history of the crustal-scale Coast shear zone north of Portland Canal, southeast Alaska and British Columbia. Journal of Structural Geology, 20(7), 883-904.

Lamb, A. L., Wilson, G. P., & Leng, M. J. (2006). A review of coastal palaeoclimate and relative sea-level reconstructions using δ13C and C/N ratios in organic material. Earth-Science Reviews, 75(1-4), 29-57.

LeCheminant, A. N., and Van Breemen, O., 1994, U–Pb ages of Proterozoic dyke swarms, Lac de Gras area, NWT: evidence for progressive break-up of an Archean supercontinent: Geological Association of Canada/Mineralogical Association of Canada, Program with Abstracts, v. 19, p. A62.

Leckie, D. A., Potocki, D. J., & Visser, K. (1991). The Lower Cretaceous Chinkeh Formation: A Frontier-Type Play in the Liard Basin of Western Canada (1). AAPG Bulletin, 75(8), 1324-1352.

Lehmann, M.F., Bernasconi, S.M., Barbieri, A., McKenzie, J.A. (2002) Preservation of organic matter and alteration of its carbon and nitrogen isotope composition during simulated and in situ early sedimentary diagenesis. Geochimica et Cosmochimica Acta, 66(20), 3573-3584.

Mahon, K. I. (1996). The New “York” regression: Application of an improved statistical method to geochemistry. International Geology Review, 38(4), 293-303.

McKinlay, F. T., Smith, B. S., de Gasparis, S., & Kong, J. (1998, April). Geology of the recently discovered Hardy Lake kimberlites, NWT. In International Kimberlite Conference: Extended Abstracts (Vol. 7, No. 1, pp. 564-566

Meyers, P. A., & Ishiwatari, R. (1993). Lacustrine organic geochemistry—an overview of indicators of organic matter sources and diagenesis in lake sediments. Organic geochemistry, 20(7), 867-900.

Meyers, P. A. (1994). Preservation of elemental and isotopic source identification of sedimentary organic matter. Chemical geology, 114(3-4), 289-302.

Miller, E. L., Gelman, M., Parfenov, L., Hourigan, J., Grantz, A., & Klemperer, S. L. (2002). Tectonic setting of Mesozoic magmatism: A comparison between northeastern Russia and the North American Cordillera. Special Papers-Geological Society of America, 313-332. M.Sc. thesis, Dalhousie University, Nova Scotia, Canada. Published thesis.

Molenaar, C. M., Bird, K. J., & Kirk, A. R. (1987). Cretaceous and Tertiary stratigraphy of northeastern Alaska.

Moll-Stalcup, E. J., Plafker, G., & Berg, H. C. (1994). Latest Cretaceous and Cenozoic magmatism in mainland Alaska. The geology of Alaska, 1, 589-619.

Nassichuk, W. W., & McIntyre, D. J. (1995). Cretaceous and Tertiary fossils discovered in kimberlites at Lac de Gras in the Slave Province, Northwest Territories. Geological Survey of Canada Current Research, 1995, 109-114.

Nassichuk, W. W., and McIntyre, D. J., 1996, Fossils from diamondiferous kimberlites at Lac de Gras, NWT: Age and paleogeography. Searching for diamonds in Canada: Geological Survey of Canada, Open-File Report 3228, p. 43-46, doi:10.4095/210938.

Nowicki, T., Crawford, B., Dyck, D., Carlson, J., McElroy, R., Oshust, P., and Helmstaedt, H., 2004, The geology of kimberlite pipes of the Ekati property, Northwest Territories, Canada: Lithos, v. 76(1-4), p. 1-27, doi: 10.1016/j.lithos.2004.03.020.

O'Connell, David W., et al. "Vivianite formation and its role in phosphorus retention in Lake Ørn, Denmark." *Chemical geology* 409 (2015): 42-53.

Parsons, M. (1993). Geochemistry and petrogenesis of late Cretaceous bentonites from the Kanguk Formation, Axel Heiberg and Ellesmere islands, Canadian High Arctic, B.Sc. thesis, Dalhousie University, Nova Scotia, Canada. Published thesis.

Pearce, J. A., Harris, N. B., & Tindle, A. G. (1984). Trace element discrimination diagrams for the tectonic interpretation of granitic rocks. Journal of petrology, 25(4), 956-983.

Pease, V., Miller, E., Wyld, S. J., Sokolov, S., Akinin, V., & Wright, J. E. (2018). U–Pb zircon geochronology of Cretaceous arc magmatism in eastern Chukotka, NE Russia, with implications for Pacific plate subduction and the opening of the Amerasia Basin. Geological Society, London, Special Publications, 460(1), 159-182.

Pell, J. A. (1997). Kimberlites in the Slave Craton, northwest territories, Canada. Geoscience Canada, 24(2).

Phillips, R. L., Pickthorn, L. G., Rearic, D. M., Galloway, J. P., & Hamilton, T. D. (1988). Late Cretaceous sediments from the northeast Chukchi Sea. US Geological Survey Circular, 1016, 187-189.

Pirrung, M., Buchel, G., & Jacoby, W. (2001). The Tertiary volcanic basins of Eckfeld, Enspel and Messel (Germany). Zeitschrift-Deutschen Geologischen Gesellschaft, 152(1), 27-60

Pirrung, M., Fischer, C., Büchel, G., Gaupp, R., Lutz, H., & Neuffer, F. O. (2003). Lithofacies succession of maar crater deposits in the Eifel area (Germany). Terra Nova, 15(2), 125-132.

Pointon, M. A., Flowerdew, M. J., Hülse, P., Schneider, S., & Whitehouse, M. J. (2019). Mixed local and ultra-distal volcanic ash deposition within the Upper Cretaceous Kanguk Formation, Sverdrup Basin, Canadian Arctic Islands. Geological Magazine, 1-18.

R Core Team, 2013, R foundation for statistical computing: v. 3.0

Ricketts, B. D., & Stephenson, R. A. (1994). The demise of Sverdrup Basin; Late Cretaceous-Paleogene sequence stratigraphy and forward modeling. Journal of Sedimentary Research, 64(4b), 516-530.

Sabel, M., Bechtel, A., Püttmann, W., & Hoernes, S. (2005). Palaeoenvironment of the Eocene Eckfeld Maar lake (Germany): implications from geochemical analysis of the oil shale sequence. Organic Geochemistry, 36(6), 873-891.

Sarkar, C., Heaman, L. M., and Pearson, D. G., 2015, Duration and periodicity of kimberlite volcanic activity in the Lac de Gras kimberlite field, Canada and some recommendations for kimberlite geochronology: Lithos, v. 218, p. 155-166, doi:10.1016/j.lithos.2015.01.017.

Schandl, E. S., & Gorton, M. P. (2002). Application of high field strength elements to discriminate tectonic settings in VMS environments. Economic geology, 97(3), 629-642.

Schröder-Adams, C. J., Cumbaa, S. L., Bloch, J., Leckie, D. A., Craig, J., El-Dein, S. A. S., ... & Kenig, F. (2001). Late Cretaceous (Cenomanian to Campanian) paleoenvironmental history of the Eastern Canadian margin of the Western Interior Seaway: bonebeds and anoxic events. Palaeogeography, Palaeoclimatology, Palaeoecology, 170(3-4), 261-289.

Schröder-Adams, C. (2014). The Cretaceous Polar and Western Interior seas: paleoenvironmental history and paleoceanographic linkages. Sedimentary Geology, 301, 26-40.

Shulmeister, J., Nobes, D. C., & Striewski, B. (2008, May). Paleoclimate Records from New Zealand Maar Lakes, Insights into ENSO Teleconnections and Climatic Events in the South (West) Pacific. In AGU Spring Meeting Abstracts.

Sims, P. A., Mann, D. G., & Medlin, L. K. (2006). Evolution of the diatoms: insights from fossil, biological and molecular data. Phycologia, 45(4), 361-402.

Singh, R. S., Stoermer, E. F., & Kar, R. (2006). Earliest freshwater diatoms from the Deccan Intertrappean (Maastrichtian) sediments of India. Micropaleontology, 52(6), 545-551.

Siver, P. A., Wolfe, A. P., & Edlund, M. B. (2010). Taxonomic descriptions and evolutionary implications of Middle Eocene pennate diatoms representing the extant genera Oxyneis, Actinella and Nupela (Bacillariophyceae). Plant Ecology and Evolution, 143(3), 340-351.

Siver, P. A., Wolfe, A. P., and Edlund, M. B., 2016, Fideliacyclus wombatiensis gen. et sp. nov. a Paleocene non-marine centric diatom from northern Canada with complex frustule architecture: Diatom Research, v. 31(4), p. 397-408, doi:10.1080/0269249X.2016.1256351.

Siver, P. A., Velez, M., Cliveti, M., & Binda, P. (2018). Early Freshwater Diatoms from the Upper Cretaceous Battle Formation in Western Canada. Palaios, 33(12), 525-534

Spicer, R. A., & Herman, A. B. (2010). The Late Cretaceous environment of the Arctic: a quantitative reassessment based on plant fossils. Palaeogeography, Palaeoclimatology, Palaeoecology, 295(3-4), 423-442.

Slattery, Joshua S., et al. "Early Cretaceous to Paleocene paleogeography of the Western Interior Seaway: the interaction of eustasy and tectonism." Wyoming Geological Association Guidebook 2015 (2015): 22-60.

Smith, R. M. H. (1986). Sedimentation and palaeoenvironments of Late Cretaceous crater-lake deposits in Bushmanland, South Africa. Sedimentology, 33(3), 369-386

Stasiuk, L. D., Sweet, A. R., and Issler, D. R., 2002, Organic petrology, organic geochemistry, palynology and petrophysics data from Lac de Gras kimberlites and associated sedimentary rocks and xenoliths: Geological Survey of Canada, Open-File Report 4272.

Stasiuk, L. D., Sweet, A. R., and Issler, D. R., 2006, Reconstruction of burial history of eroded Mesozoic strata using kimberlite shale xenoliths, volcaniclastic and crater facies, Northwest Territories, Canada: International Journal of Coal Geology, v. 65(1-2), p. 129-145, doi: 10.1016/j.coal.2005.04.011.

Sun, S. S., & McDonough, W. F. (1989). Chemical and isotopic systematics of oceanic basalts: implications for mantle composition and processes. Geological Society, London, Special Publications, 42(1), 313-345.

Sweet, A.R., Ricketts, B.D., Cameron, A.R. and Norris, D.K. 1989. An integrated analysis of the Brackett Coal Basin, Northwest Territories. In: Current Research, Part G, Geological Survey of Canada, Paper 89-1G, p. 85-99.

Sweet, A. R., Stasiuk, L. D., Nassichuk, W. W., Catunneau, O., and McIntyre, D. J., 2003, Paleontology and diamonds: geological environments associated with kimberlite emplacement, Lac de Gras, Northwest Territories, Canada: International Kimberlite Conference: Extended Abstracts, v. 8, doi: 10.29173/ikc3040.

Talbot, M. R., & Livingstone, D. A. (1989). Hydrogen index and carbon isotopes of lacustrine organic matter as lake level indicators. Palaeogeography, Palaeoclimatology, Palaeoecology, 70(1-3), 121-137.

Talbot, M. R. (2002). Nitrogen isotopes in palaeolimnology. In Tracking environmental change using lake sediments (pp. 401-439). Springer, Dordrecht.

Tieszen, Larry L., et al., “The distribution of C 3 and C 4 grasses and carbon isotope discrimination along an altitudinal and moisture gradient in Kenya." Oecologia 37.3 (1979): 337-350.

Tikhomirov PL, Kalinina EA, Moriguti T, Makishima A, Kobayashi K, Cherepanova IY and Nakamura E (2012) The Cretaceous Okhotsk–Chukotka Volcanic Belt (NE Russia): geology, geochronology, magma output rates, and implications on the genesis of silicic LIPs. Journal of Volcanology and Geothermal Research 221–222, 14–32.

Trettin, H. P., & Parrish, R. (1987). Late Cretaceous bimodal magmatism, northern Ellesmere Island: isotopic age and origin. Canadian Journal of Earth Sciences, 24(2), 257-265.

Trop, J. M., Hampton, B., Ridgway, K., & Gehrels, G. E. (2005, October). Latest Cretaceous sedimentary record of forearcarc-retroarc relationships in south-central Alaska. In Geological Society of America Annual Meeting, Salt Lake City, p. Paper (No. 31-14).

Trop, J. M., Ridgway, K. D., Glen, J. M. G., & O'Neill, J. M. (2007). Mesozoic and Cenozoic tectonic growth of southern Alaska: A sedimentary basin perspective. SPECIAL PAPERS-GEOLOGICAL SOCIETY OF AMERICA, 431, 55.

Van Mooy, B. A., Keil, R. G., & Devol, A. H. (2002). Impact of suboxia on sinking particulate organic carbon: Enhanced carbon flux and preferential degradation of amino acids via denitrification. Geochimica et Cosmochimica Acta, 66(3), 457-465.

Vermeesch, P., 2018, IsoplotR: A free and open toolbox for geochronology: Geoscience Frontiers, v. 9, p. 1479-1493.

Whiticar, M. J. (1999). Carbon and hydrogen isotope systematics of bacterial formation and oxidation of methane. Chemical Geology, 161(1-3), 291-314.

Williams, I.S., 1998, U–Th–Pb geochronology by ion microprobe. In: McKibben, M.A., Shanks III, W.C., Ridley,W.I. (Eds.), Applications of Microanalytical Techniques to Understanding Mineralizing Processes. Reviews in Economic Geology 7, pp. 1–35.

Williams, C. J., LePage, B. A., Johnson, A. H., & Vann, D. R. (2009). Structure, biomass, and productivity of a late Paleocene arctic forest. Proceedings of the Academy of Natural Sciences of Philadelphia, 158(1), 107-128.

Williamson, C. E., Saros, J. E., Vincent, W. F., & Smol, J. P. (2009). Lakes and reservoirs as sentinels, integrators, and regulators of climate change. Limnology and Oceanography, 54(6part2), 2273-2282.

Wolfe, A. P., & Siver, P. A. (2009). Three extant genera of freshwater thalassiosiroid diatoms from Middle Eocene sediments in northern Canada. American Journal of Botany, 96(2), 487-497.

Wolfe, A. P., Csank, A. Z., Reyes, A. V., McKellar, R. C., Tappert, R., & Muehlenbachs, K. (2012). Pristine Early Eocene wood buried deeply in kimberlite from northern Canada. PLoS One, 7(9), e45537.

Wolfe, A. P., Reyes, A. V., Royer, D. L., Greenwood, D. R., Doria, G., Gagen, M. H., ... & Westgate, J. A. (2017). Middle Eocene CO2 and climate reconstructed from the sediment fill of a subarctic kimberlite maar. Geology, 45(7), 619-622.

Yorath, C. J. and Cook, D.G. 1981. Cretaceous and Tertiary stratigraphy and paleogeography, Northern Interior Plains, District of Mackenzie. Geological Survey of Canada Memoir 398, 1-76.

APPENDIX A

METHODS A.1 ZIRCON AND VOLCANIC GLASS SEPARATION TECHNIQUES

Samples UA3134 (40-2-110) and UA3135 (39-3-39) were collected from the Wombat core 00-05 in April, 2018 at the Northwest Territories Geological Survey core facility. All zircon and volcanic glass separations and analysis were conducted at the University of Alberta. First, the samples were disintegrated using ultrasonic bath to separate clays from the minerals and glass and then treated with hydrogen peroxide to remove the organics. The bulk tephra samples were wet sieved into discrete grain size fractions using 250 μm, 149 μm, 75 μm and 45 μm mash sieves. The 149 μm - 75 μm fraction was used for further separation, due to the predominance < 45 μm material. A handheld magnet was used to remove magnetite and then the non-magnetic fraction was further concentrated by magnetic separation at 0.2, 0.4, 0.6 amps using a Frantz LB1 magnetic separator. The remaining non-magnetic fraction was then density separated using tetrabromoethane (TBE) at a density of 2.8 g/cm^3 and again purified using methylene iodide (MI) at a density of 3.3 g/cm^3. Zircon grains were hand picked from a heavy mineral-rich fraction under a binocular microscope and mounted in a standard 1" epoxy puck. The grains were polished to remove adhered glass and to expose the grains centers. Imaging under petrographic microscope combined with cathodoluminescence and electron backscatter imaging on a Zeiss EVO LS15 EP-SEM was used to identify internal zircon textures, inclusions and morphology. ImageJ software was used to characterize individual zircon shape and size. Similarly, the light, glass rich fraction was epoxy mounted in acrylic puck, polished and carbon coated. Images of volcanic glass were obtained by petrographic microscope. Cathodoluminescence and electron backscatter imaging on the volcanic glass shards was not performed.

METHODS A.2 ZIRCON U-Pb DATING BY LA-ICP-MS

Zircon U-Pb isotope data were collected using a NewWave 213 nm laser system coupled with a NuPlasma I Multi-Collector ICP Mass Spectrometer (MC-ICPMS) at University of Alberta. The analytical procedure involved using a 30 µm beam diameter, 4 Hz repetition rate, ˜3 J/cm^2 energy density and 30 s ablation time. A standard-sample-standard method was used to correct instrumental drift, U-Pb fractionation and reproducibility by analyzing GJ-1(^{206}Pb/^{238}U$_{age}$ = 600.7 ± 1.1 Ma; Jackson et al., 2004) primary standard reference zircon grains along with Plešovice (^{206}Pb/^{238}U$_{age}$ = 337.13 ± 0.37 Ma; Sláma et al., 2008) and 94-35 (^{206}Pb/^{238}U$_{age}$ = 55.5 ± 1.5 Ma; Klepeis et al., 1998) as a secondary zircon standards after each set of 10 unknowns. The reported ^{206}Pb/^{238}U ages of the standard reference zircon grains agree within uncertainty with those published in the literature, with weighted means of ages for Plešovice zircon standard at ^{206}Pb/^{238}U$_{age}$ = 338.59 ± 3.23 Ma (n = 7, MSWD = 0.56) and the 94-35 zircon standard at ^{206}Pb/^{238}U$_{age}$ = 55.67 ± 0.71 (n = 5, MWD = 1.64). The quadratic addition was used to propagate external uncertainties and the 2σ analytical reproducibility estimated from GJ-1 primary standard for ^{206}Pb/^{238}U ~ 1.9 % . ^{235}U was calculated from ^{238}U assuming ^{238}U/^{235}U = 137.818 (Hiess et al., 2012) and U-Pb ages were calculated using the decay constants from Jaffey et al., (1971).

All zircon analyses were corrected for common lead using the "207 method" and an initial Pb composition taken from Stacey and Kramers (1975). This method is ideal for samples that are expected to be concordant and for applications requiring $^{206}\mathrm{Pb}/^{238}\mathrm{U}$ to be determined as accurately as possible. The fraction of the common lead is calculated from the theoretical $^{207}\mathrm{Pb}/^{206}\mathrm{Pb}_t$, estimated initial common $^{207}\mathrm{Pb}/^{206}\mathrm{Pb}_c$ and measured $^{207}\mathrm{Pb}/^{206}\mathrm{Pb}_m$ using:

$$f = (^{207}\mathrm{Pb}/^{206}\mathrm{Pb}_c - {}^{207}\mathrm{Pb}/^{206}\mathrm{Pb}_m) / (^{207}\mathrm{Pb}/^{206}\mathrm{Pb}_c - {}^{207}\mathrm{Pb}/^{206}\mathrm{Pb}_t)$$

The radiogenic $^{206}\mathrm{Pb}^*/^{238}\mathrm{U}$ can then be calculated from the measured $^{206}\mathrm{Pb}/^{238}\mathrm{U}_m$ using:

$$^{206}\mathrm{Pb}^*/^{238}\mathrm{U} = f \text{ x } (^{206}\mathrm{Pb}/^{238}\mathrm{U}_m)$$

The percent of common Pb in $^{206}\mathrm{Pb}/^{238}\mathrm{U}$ is calculated by using:

$$^{206}\mathrm{Pb}_c = f \text{ x } 100$$

The $^{206}\mathrm{Pb}^*/^{238}\mathrm{U}$ is used for the zircon age calculation, due to the difficulty in measuring $^{207}\mathrm{Pb}$ in young samples resulting in larger $^{207}\mathrm{Pb}/^{206}\mathrm{Pb}$ uncertainty and because the range in radiogenic $^{207}\mathrm{Pb}/^{206}\mathrm{Pb}$ throughout the Phanerozoic (0.0461 – 0.0584) is too small to provide a sensitive measure of the age. The uncorrected data were first plotted on a Wetherill diagram using IsoplotR software to illustrate the effects of common Pb and Pb loss in U-Pb isotopic analysis of the zircon grains (Wetherill, 1956; R Core Team, 2013; Vermeesch, 2018). The final age for the tephra zircon crystallization was calculated using the weighted mean of the common Pb corrected $^{206}\mathrm{Pb}/^{238}\mathrm{U}$ ages for the youngest group of zircon analysis overlapping within 2σ uncertainty.

METHODS A.3 $\delta^{13}C$, C_{org}:N_{tot}, C_{org}

Forty-three of the Wombat core samples were ground with a mortar and pestle and weighted. The carbonates were removed by treating samples with 1 N HCl over 24 hours. The decalcifed samples were washed, freeze-dried, weighted (2-5 mg) on a microscale, and loaded into a tin capsules. The capsules were then combusted in excess oxygen using a FLASH HT Plus Elemental Analyzer with residual nitrous oxides reduced by reaction with Cu. Total organic carbon (C_{org}) and total nitrogen (N_{tot}) were determined with Thermal Conductivity Detector (TCD) and Thermo Fisher Delta V Plus isotope-ratio mass spectrometer was used to determine carbon isotope composition. The IRMS soil standard were placed through each run of samples at a range of weights, the standards used include: High Organic Content Sediment IRMS Standard ($C_{org} = 7.45 \pm 0.14$ wt.%; $N_{tot} = 0.52 \pm 0.02$ wt.%; $\delta^{13}C$ -28.85 ± 0.20 ‰, VPDB) and Low Organic Content Sediment IRMS Standard ($C_{org} = 1.61 \pm 0.09$ wt.%; $N_{tot} = 0.133 \pm 0.023$ wt.%; $\delta^{13}C = -26.66 \pm 0.24$ ‰, VPDB).

Stable isotope results are expressed in delta (δ) notation and are measured in per mil (‰) difference between the $^{13}C/^{12}C$ isotope ratio of the sample and that of the international standard. The carbon isotope ($\delta^{13}C$) values were determined by calibration of $^{13}C/^{12}C$ isotope ratio against the Vienna Pee Dee Belemnite (VPDB; Craig, 1957) standard using:

$$\delta^{13}C = [(^{13}C/^{12}C)_{sample} / ((^{13}C/^{12}C)_{VPDB})] - 1 \quad X\ 1000$$

The difference between the certified $\delta^{13}C$ value and the linearity-corrected raw $\delta^{13}C$ of the IRMS standards was used to derive C correction factor which was then added to the linearity corrected $\delta^{13}C$ values of the unknowns. The analytical reproducibility of 0.2 ‰ (2σ) for $\delta^{13}C$

was based on replicate analysis of IRMS soil standards. The weight percentage ratio between total organic carbon (C_{org}) and total nitrogen (N_{tot}) was used to derive C_{org}:N_{tot}, which can be multiplied by 1.167 (the ratio of atomic weights of carbon and nitrogen) to provide atomic C_{org}:N_{tot} ratios (Leng and Lewis, 2017).

METHODS A.4 GLASS MAJOR AND TRACE ELEMENT GEOCHEMISTRY

The major element compositions were examined using bivariate plots to identify outliers and examine the effect of alteration and mobility of the elements. The outliers analysis are defined as points lying beyond 2σ uncertainty of the main oxide geochemical population and were attributed mainly to the accidental analysis of the mineral microcrysts in the glass matrix.

The rare earth element (REE) compositions were normalized to that of chondrite following Sun and McDonough (1989). The light REE (LREE) were compared to heavy REE (HREE) using $(La/Yb)_N$ as a proxy for a degree of fractionation (where “N” indicates that the ratio of La and Yb is normalized to the abundances in chondrite). La is a LRRE and is highly incompatible in spinel and garnet, while Yb is a HREE is incompatible in spinel, but not garnet.

The Eu and Ce anomalies were calculated as:

$$Eu/Eu^*_N = (Eu)_N / [(Sm)_N \times (Gd)_N]^{0.5}$$ (Taylor and McLennan, 1985)

and

$$Ce/Ce^*_N = 3(Ce)_N / [2(La)_N + (Nd)_N]$$ (Sholkovitz, 1995)

The “N” depicts the chondrite normalized values. The Eu/Eu^*_N and Ce/Ce^*_N values of 1 indicate that elements are not fractionated relative to the crustal composition, values less than 1 indicate negative anomaly and more than 1 indicate a positive anomaly.

The degree of chemical alteration of the glass is estimated using the chemical index of alteration (CIA):

$$CIA= [Al_2O_3 / (Al_2O_3+CaO+Na_2O+K_2O)] \times 100$$ (Nesbitt and Young, 1984)

For example, the low (< 50) CIA of tephra deposits 2suggests the absence of chemical weathering due to the conservation of mobile cations Ca^{2+}, Na^+ and K^+ relative to the immobile Al.

APPENDICES REFERENCES CITED

Goolaerts, A., Mattielli, N., de Jong, J., Weis, D., & Scoates, J. S., 2004, Hf and Lu isotopic reference values for the zircon standard 91500 by MC-ICP-MS. Chemical Geology, 206 (1-2), 1-9.

Craig, H. (1957). Isotopic standards for carbon and oxygen and correction factors for mass-spectrometric analysis of carbon dioxide. Geochimica et cosmochimica acta, 12(1-2), 133-149.

Hiess, J., Condon, D. J., McLean, N., & Noble, S. R. (2012). 238U/235U systematics in terrestrial uranium-bearing minerals. Science, 335(6076), 1610-1614.

Jackson, S. E., Pearson, N. J., Griffin, W. L., & Belousova, E. A. (2004). The application of laser ablation-inductively coupled plasma-mass spectrometry to in situ U–Pb zircon geochronology. Chemical geology, 211(1-2), 47-69.

Jaffey, A. H., Flynn, K. F., Glendenin, L. E., Bentley, W. T., & Essling, A. M. (1971). Precision measurement of half-lives and specific activities of U 235 and U 238. Physical review C, 4(5), 1889.

Klepeis, K. A., Crawford, M. L., & Gehrels, G. (1998). Structural history of the crustal-scale Coast shear zone north of Portland Canal, southeast Alaska and British Columbia. Journal of Structural Geology, 20(7), 883-904.

Leng, M. J., & Lewis, J. P. (2017). C/N ratios and carbon isotope composition of organic matter in estuarine environments. In *Applications of Paleoenvironmental Techniques in Estuarine Studies* (pp. 213-237). Springer, Dordrecht.

Nesbitt, H. W., & Young, G. M. (1982). Early Proterozoic climates and plate motions inferred from major element chemistry of lutites. Nature, 299(5885), 715.

R Core Team, 2013, R foundation for statistical computing: v. 3.0

Sholkovitz, E. R. (1995). The aquatic chemistry of rare earth elements in rivers and estuaries. Aquatic Geochemistry, 1(1), 1-34.

Stacey, J. T., & Kramers, 1., 1975, Approximation of terrestrial lead isotope evolution by a two-stage model. Earth and planetary science letters, 26(2), 207-221.

Sláma, J., et al., 2008, Plešovice zircon — A new natural reference material for U–Pb and Hf isotopic microanalysis: Chemical Geology, v. 249, p. 1-35.

Sun, S. S., & McDonough, W. F. (1989). Chemical and isotopic systematics of oceanic basalts: implications for mantle composition and processes. Geological Society, London, Special Publications, 42(1), 313-345.

Taylor, S. R., & McLennan, S. M. (1985). The continental crust: its composition and evolution.

Vermeesch, P., 2018, IsoplotR: A free and open toolbox for geochronology: Geoscience Frontiers, v. 9, p. 1479-1493.

Wetherill, G. W. (1956). Discordant uranium-lead ages, I. Eos, Transactions American Geophysical Union, 37(3), 320-326.

Williams, I.S., 1998, U–Th–Pb geochronology by ion microprobe. In: McKibben, M.A., Shanks III, W.C., Ridley,W.I. (Eds.), Applications of Microanalytical Techniques to Understanding Mineralizing Processes. Reviews in Economic Geology 7, pp. 1–35.

Table A.1 LA-ICP-MS operating conditions

Laboratory Name	Canadian Center for isotopic Microanalysis, Dept. of Earth & Atmos.Sci., University of Alberta
sample type	zircon
imaging	Cathodoluminescense, BSE
Laser system	ESI/New Wave Research UP213 Nd YAG
ablation cell	New Wave/ESI standard cell, 33cm3 volume
laser wavelength	213nm
pulse width	<4 ns
fluence	~2-3J/cm2
repetition rate	4 Hz
ablation duration	30s
ablation pit depth	~10-15um
spot diameter	30um
sampling mode	spot ablation
carrier gas	100% ultrapure Helium
cell carrier gas flow	0.5L/min
ICPMS	NuPlasma I Multi-Collector ICP-MS
sample introduction	Ablation aerosol
RF power	1550W
make up gas flow	~0.55 L/min Ar + 4 mls/min N_2 ; Makeup gas and ablated aerosol mixed in 30cc syringe mixer volume
detection system	collector array consisting of 12 Faraday buckets and three ion counters
masses measured	238, 235, 208-204
dwell times	238 20ms, 235, 208-206 30ms, 204 40ms total sweep time 200 ms
deadtime	40 ns
data processing	Offline, internal spreadhsheet
gas blank	25 second on peak zero subtratction
calibration strategy	GJ-1 used as primary reference material, Pleosvice and 94-35 used for secondary validation
data processing	U-Pb fractionation and normalization, uncertainty propagation in external spreadsheet
mass discrimination	normalized to GJ-1
common Pb correction	207 method
Uncertainty level/propagation	Uncertainties are 2 sigma ablsolute. External unctertainties propagted by quadratic addition.

APPENDIX B.

Table B.1 Summary of U-Pb standard reference zircon analysis

Sample number	^{206}Pb (cps)	^{204}Pb (cps)	^{207}Pb/^{206}Pb	2σ	^{207}Pb/^{235}U	2σ	^{206}Pb/^{238}U	2σ	ρ	^{206}Pb$_c$ ^{a} (%)	^{206}Pb/^{238}U ^{b}	Age (Ma) ^{206}Pb/^{238}U ^{b}	Age (Ma) 2σ
gj1-1	183911	65	0.06059	0.00072	0.80247	0.02024	0.09606	0.00214	0.883	0.1	0.09598	590.8	12.56
gj1-2	192628	77	0.06001	0.00072	0.82881	0.01913	0.10017	0.00197	0.854	0.0	0.100152	615.3	11.56
gj1-3	197028	69	0.05975	0.00068	0.80881	0.01981	0.09818	0.00213	0.887	0.0	0.0982	603.8	12.50
gj1-4	198597	74	0.06004	0.00069	0.81988	0.01980	0.09904	0.00211	0.881	0.0	0.099025	608.7	12.34
gj1-5	197228	78	0.06077	0.00075	0.81269	0.01879	0.09700	0.00190	0.848	0.1	0.096893	596.2	11.15
gj1-6	196872	38	0.06020	0.00069	0.81556	0.01903	0.09826	0.00200	0.873	0.0	0.098221	604.0	11.73
gj1-7	185539	60	0.06008	0.00070	0.81772	0.01961	0.09872	0.00207	0.876	0.0	0.098698	606.8	12.15
plesovice-1	239610	80	0.05324	0.00063	0.39922	0.00950	0.05439	0.00112	0.868	0.1	0.054325	341.0	6.9
plesovice-2	233595	78	0.05297	0.00065	0.39520	0.00968	0.05411	0.00115	0.868	0.1	0.054072	339.5	7.0
plesovice-3	243276	75	0.05290	0.00063	0.39843	0.00956	0.05462	0.00114	0.867	0.1	0.054585	342.6	6.9
plesovice-4	235323	75	0.05304	0.00065	0.39092	0.00982	0.05345	0.00117	0.874	0.1	0.053404	335.4	7.2
plesovice-5	229607	59	0.05326	0.00064	0.39396	0.00964	0.05365	0.00114	0.871	0.1	0.053585	336.5	7.0
plesovice-6	216188	34	0.05324	0.00064	0.39422	0.00962	0.05370	0.00114	0.869	0.1	0.053643	336.8	7.0
plesovice-7	207873	19	0.05354	0.00067	0.39804	0.00971	0.05392	0.00113	0.859	0.2	0.053835	338.0	6.9
9435-1	3784	48	0.05677	0.00553	0.06856	0.00681	0.00876	0.00017	0.193	1.2	0.008652	55.5	1.1
9435-2	3581	52	0.06216	0.00641	0.07463	0.00785	0.00871	0.00018	0.196	1.9	0.008543	54.8	1.1
9435-3	3595	36	0.05630	0.00325	0.06788	0.00414	0.00874	0.00017	0.319	1.2	0.008643	55.5	1.1
9435-4	3683	37	0.05633	0.00337	0.06852	0.00434	0.00882	0.00018	0.326	1.2	0.00872	56.0	1.2
9435-5	3191	46	0.07080	0.00959	0.08903	0.01220	0.00912	0.00019	0.151	3.0	0.008848	56.8	1.2

Note*: Correction for common Pb made using ^{207}Pb (Williams, 1998).

^{a} ^{206}Pb$_c$, percentage of ^{206}Pb that is common Pb.

^{b} Radiogenic ^{206}Pb/^{238}U.

Table B.2 Sample UA3135 (39-3-39) LA-ICP-MS U-Pb Zircon Results

													Age (Ma)	
Sample number	^{206}Pb (cps)	^{204}Pb (cps)	^{207}Pb/^{206}Pb	2σ	^{207}Pb/^{235}U	2σ	^{206}Pb/^{238}U	2σ	ρ	^{206}Pb$_c$ ^{a} (%)	^{206}Pb/^{238}U ^{b}	2σ	^{206}Pb/^{238}U ^{b}	2σ
33-3-39-12	44331	65	0.06150	0.00128	0.09814	0.00288	0.01157	0.00024	0.705	1.7	0.01137266	0.000234	72.9	1.5
39-3-39-15	**11570**	**26**	**0.04964**	**0.00137**	**0.08572**	**0.00330**	**0.01252**	**0.00034**	**0.699**	**0.2**	**0.012494107**	**0.000334**	**80.0**	**2.1**
39-3-39-23	**13792**	**47**	**0.05328**	**0.00156**	**0.09282**	**0.00337**	**0.01264**	**0.00027**	**0.591**	**0.7**	**0.012546412**	**0.000267**	**80.4**	**1.7**
39-3-39-29	**16577**	**7**	**0.05242**	**0.00216**	**0.09231**	**0.00429**	**0.01277**	**0.00027**	**0.457**	**0.6**	**0.012695463**	**0.000269**	**81.3**	**1.7**
39-3-39-22	**7603**	**31**	**0.05004**	**0.00248**	**0.08818**	**0.00472**	**0.01278**	**0.00026**	**0.376**	**0.3**	**0.012742147**	**0.000254**	**81.6**	**1.6**
39-3-39-24	**10386**	**36**	**0.05071**	**0.00197**	**0.08978**	**0.00390**	**0.01284**	**0.00025**	**0.451**	**0.4**	**0.012791301**	**0.00025**	**81.9**	**1.6**
39-3-39-32	**11887**	**51**	**0.05279**	**0.00194**	**0.09393**	**0.00397**	**0.01291**	**0.00027**	**0.493**	**0.6**	**0.012823206**	**0.000265**	**82.1**	**1.7**
39-3-39-14	**8637**	**24**	**0.05644**	**0.00399**	**0.10092**	**0.00740**	**0.01297**	**0.00025**	**0.262**	**1.1**	**0.012826173**	**0.000245**	**82.2**	**1.6**
39-3-39-19	**15293**	**41**	**0.04986**	**0.00108**	**0.08845**	**0.00302**	**0.01287**	**0.00034**	**0.772**	**0.3**	**0.012830248**	**0.000336**	**82.2**	**2.2**
39-3-39-5	**9069**	**35**	**0.05020**	**0.00230**	**0.08922**	**0.00455**	**0.01289**	**0.00029**	**0.437**	**0.3**	**0.0128488**	**0.000284**	**82.3**	**1.8**
39-3-39-9	**13888**	**48**	**0.04803**	**0.00120**	**0.08524**	**0.00277**	**0.01287**	**0.00027**	**0.640**	**0.0**	**0.0128647**	**0.000265**	**82.4**	**1.7**
39-3-39-25	**9770**	**32**	**0.04944**	**0.00174**	**0.08806**	**0.00360**	**0.01292**	**0.00027**	**0.513**	**0.2**	**0.012888687**	**0.000269**	**82.6**	**1.7**
39-3-39-4	**8455**	**46**	**0.05524**	**0.00485**	**0.09970**	**0.00899**	**0.01309**	**0.00027**	**0.228**	**1.0**	**0.012965241**	**0.000265**	**83.0**	**1.7**
39-3-39-6	**17432**	**50**	**0.06059**	**0.00412**	**0.11041**	**0.00780**	**0.01322**	**0.00025**	**0.268**	**1.6**	**0.013002331**	**0.000245**	**83.3**	**1.6**
39-3-39-2	**19110**	**38**	**0.04950**	**0.00116**	**0.08903**	**0.00324**	**0.01304**	**0.00036**	**0.766**	**0.2**	**0.013013582**	**0.000361**	**83.3**	**2.3**
39-3-39-26	**25027**	**352**	**0.24935**	**0.02375**	**0.60268**	**0.06100**	**0.01753**	**0.00060**	**0.338**	**25.4**	**0.013074044**	**0.000445**	**83.7**	**2.9**
39-3-39-10	**5724**	**40**	**0.05199**	**0.00238**	**0.09437**	**0.00473**	**0.01316**	**0.00027**	**0.411**	**0.5**	**0.013092126**	**0.000269**	**83.8**	**1.7**
39-3-39-7	**7608**	**44**	**0.05355**	**0.00239**	**0.09772**	**0.00483**	**0.01323**	**0.00028**	**0.428**	**0.7**	**0.013136422**	**0.000276**	**84.1**	**1.8**
39-3-39-8	9064	50	0.05382	0.00264	0.09877	0.00524	0.01331	0.00027	0.382	0.8	0.01320787	0.000265	84.6	1.7
39-3-39-21	7838	29	0.04982	0.00177	0.09137	0.00387	0.01330	0.00030	0.541	0.3	0.01326647	0.000301	85.0	1.9
39-3-39-16	14743	60	0.06220	0.00305	0.11602	0.00623	0.01353	0.00029	0.403	1.8	0.013280629	0.000286	85.0	1.8
39-3-39-27	6514	19	0.06376	0.00230	0.11930	0.00509	0.01357	0.00031	0.534	2.0	0.013295481	0.000301	85.1	1.9
39-3-39-1	11258	37	0.04914	0.00132	0.09095	0.00323	0.01342	0.00031	0.657	0.2	0.01340028	0.000311	85.8	2.0
39-3-39-20	23639	33	0.04924	0.00086	0.09137	0.00252	0.01346	0.00029	0.772	0.2	0.013432336	0.000284	86.0	1.8
39-3-39-31	28369	109	0.08940	0.00994	0.17619	0.01990	0.01429	0.00028	0.174	5.3	0.013543057	0.000264	86.7	1.7
39-3-39-18	12098	39	0.05664	0.00463	0.10697	0.00905	0.01370	0.00030	0.260	1.1	0.013543384	0.000295	86.7	1.9
39-3-39-13	9198	81	0.10405	0.01601	0.21004	0.03270	0.01464	0.00035	0.154	7.1	0.013601062	0.000323	87.1	2.1
39-3-39-28	**13244**	**229**	**0.29837**	**0.04455**	**0.82530**	**0.13791**	**0.02006**	**0.00151**	**0.449**	**31.6**	**0.013722559**	**0.001016**	**87.9**	**6.51**
39-3-39-11	19257	71	0.06682	0.00525	0.12965	0.01099	0.01407	0.00045	0.375	2.4	0.013733293	0.000433	87.9	2.8
39-3-39-33	16879	45	0.05546	0.00222	0.10630	0.00491	0.01390	0.00032	0.498	1.0	0.01376556	0.000314	88.1	2.0
39-3-39-30	40006	57	0.06512	0.00885	0.12799	0.01756	0.01425	0.00027	0.139	2.2	0.013940447	0.000264	89.2	1.7
39-3-39-17	7858	261	0.39815	0.03994	1.48947	0.20035	0.02713	0.00243	0.666	44.2	0.015146306	0.001336	96.9	8.6
39-3-39-3	19504	38	0.04946	0.00117	0.10589	0.00365	0.01553	0.00039	0.729	0.2	0.015494637	0.000385	99.1	2.5
39-3-39-34	3574	116	0.20722	0.02444	0.49672	0.06088	0.01739	0.00058	0.272	20.1	0.013889183	0.000458	88.9	2.9

Note*: Data in bold is used for the weighted mean calculation

[a] ^{206}Pb$_c$, percentage of ^{206}Pb that is common Pb.

[b] Radiogenic ^{206}Pb/^{238}U.

Table B.3 Sample UA3134 (40-2-110) LA-ICP-MS U-Pb Zircon Results

													Age (Ma)	
Sample number	^{206}Pb (cps)	^{204}Pb (cps)	^{207}Pb/^{206}Pb	2σ	^{207}Pb/^{235}U	2σ	^{206}Pb/^{238}U	2σ	ρ	^{206}Pb$_c$ ^{a} (%)	^{206}Pb/^{238}U ^{b}	2σ	^{206}Pb/^{238}U ^{b}	2σ
40-2-110-1-1	29061	41	0.050068	0.000819	0.211399	0.005813	0.030623	0.000677	0.803686	0.0	0.030616	0.000666	194.4	4.3
40-2-110-1-2	29716	64	0.056198	0.000866	0.239663	0.006212	0.030930	0.000645	0.804240	0.8	0.030685	0.00063	194.8	4.1
40-2-110-2-3	27297	18	0.050670	0.000913	0.214154	0.006229	0.030653	0.000700	0.784920	0.1	0.030623	0.000689	194.4	4.4
40-2-110-2-4	28575	31	0.050576	0.000746	0.215959	0.005967	0.030969	0.000724	0.845652	0.1	0.030943	0.000712	196.4	4.6
40-2-110-5	368120	393	0.106747	0.003252	3.539717	0.244991	0.240498	0.014947	0.897944	2.1	0.23545	0.013112	1363.0	84.0

Note*: Correction for common Pb made using ^{207}Pb (Williams, 1998).

[a] ^{206}Pb$_c$, percentage of ^{206}Pb that is common Pb.

[b] Radiogenic ^{206}Pb/^{238}U.

Table B.4 Major-element Glass Analysis for Standard Reference Glass Samples

Sample name	SiO_2	TiO_2	Al_2O_3	FeOt [a]	MnO	MgO	CaO	Na_2O	K_2O	Cl	Total (%)	H_2Od [b] (%)
Lipari obsidian (ID 3506)												
ID3506_001	74.94	0.11	13.19	1.52	0.08	0.04	0.70	3.96	5.21	0.33	100.00	0.79
ID3506_002	74.86	0.05	13.20	1.53	0.04	0.07	0.75	4.13	5.12	0.33	100.00	0.88
ID3506_003	74.71	0.06	13.23	1.54	0.07	0.06	0.73	4.06	5.25	0.37	100.00	1.28
ID3506_004	74.94	0.06	13.20	1.58	0.06	0.02	0.75	3.99	5.16	0.31	100.00	1.18
ID3506_005	74.90	0.12	13.04	1.67	0.06	0.05	0.74	3.95	5.21	0.32	100.00	0.77
ID3506_006	74.83	0.07	13.35	1.48	0.09	0.05	0.71	4.19	5.01	0.28	100.00	0.54
ID3506_007	74.75	0.10	13.33	1.52	0.05	0.05	0.69	4.09	5.17	0.33	100.00	1.02
ID3506_008	75.01	0.03	13.11	1.51	0.09	0.06	0.72	3.95	5.21	0.37	100.00	0.69
ID3506_009	74.90	0.10	13.19	1.60	0.06	0.02	0.72	4.06	5.09	0.34	100.00	0.25
ID3506_010	74.80	0.10	13.31	1.45	0.09	0.05	0.73	4.07	5.16	0.30	100.00	0.72
ID3506_011	74.95	0.11	13.11	1.54	0.05	0.05	0.76	4.02	5.14	0.34	100.00	0.82
ID3506_012	74.70	0.07	13.17	1.58	0.08	0.06	0.75	3.99	5.31	0.37	100.00	0.95
ID3506_013	74.80	0.04	13.18	1.47	0.03	0.04	0.71	4.23	5.26	0.30	100.00	0.24
ID3506_014	74.60	0.04	13.27	1.55	0.08	0.04	0.73	4.23	5.18	0.36	100.00	0.13
ID3506_015	74.54	0.10	13.34	1.65	0.11	0.02	0.73	3.98	5.26	0.34	100.00	0.61
ID3506_016	74.69	0.07	13.27	1.56	0.06	0.05	0.75	4.04	5.22	0.37	100.00	0.83
ID3506_017	74.50	0.07	13.29	1.63	0.03	0.06	0.71	4.15	5.27	0.37	100.00	0.54
ID3506_018	74.66	0.07	13.26	1.60	0.06	0.04	0.71	4.20	5.13	0.32	100.00	0.55
ID3506_019	74.82	0.07	13.33	1.54	0.06	0.04	0.73	4.04	5.12	0.33	100.00	0.75
ID3506_020	74.84	0.08	13.25	1.53	0.08	0.04	0.72	4.12	5.11	0.32	100.00	0.69
ID3506_021	74.80	0.06	13.24	1.44	0.06	0.03	0.71	4.13	5.29	0.31	100.00	0.61
ID3506_022	74.92	0.11	13.32	1.52	0.08	0.05	0.72	3.93	5.09	0.33	100.00	0.26
Mean	74.79	0.08	13.24	1.55	0.07	0.05	0.73	4.07	5.18	0.33	100.00	0.69
StDev	0.14	0.03	0.08	0.06	0.02	0.01	0.02	0.09	0.08	0.03	0.00	0.30
ID 3506	**74.10**	**0.07**	**13.10**	**1.55**	**0.07**	**0.04**	**0.74**	**4.06**	**5.13**	**0.34**	**99.09**	**-**
assayed	0.96	0.03	0.34	0.06	0.03	0.02	0.05	0.28	0.26	0.03	-	-
Old Crow Tephra												
OldCrow_001	75.25	0.39	13.08	1.78	0.11	0.27	1.39	3.74	3.79	0.26	100.00	4.06
OldCrow_002	75.28	0.29	13.04	1.70	0.05	0.26	1.46	3.93	3.76	0.28	100.00	3.44
OldCrow_003	75.29	0.29	12.98	1.77	0.07	0.24	1.51	3.74	3.89	0.30	100.00	4.38
OldCrow_004	75.25	0.37	13.10	1.64	0.08	0.28	1.34	3.91	3.85	0.25	100.00	3.74
OldCrow_005	74.61	0.28	12.91	1.71	0.06	0.31	1.42	4.79	3.71	0.28	100.00	1.31
OldCrow_006	75.19	0.36	13.20	1.76	0.02	0.27	1.45	3.75	3.76	0.30	100.00	6.26
OldCrow_007	75.36	0.29	13.10	1.64	0.06	0.28	1.44	4.03	3.57	0.29	100.00	1.61
OldCrow_008	75.57	0.27	12.97	1.70	0.04	0.32	1.44	3.75	3.74	0.27	100.00	3.52
OldCrow_009	75.59	0.33	12.83	1.66	0.09	0.29	1.42	3.90	3.68	0.27	100.00	1.51
OldCrow_010	75.40	0.27	13.18	1.65	0.09	0.30	1.43	3.63	3.83	0.28	100.00	5.12
OldCrow_011	75.48	0.24	13.11	1.65	0.02	0.25	1.47	3.94	3.62	0.26	100.00	1.05
OldCrow_012	75.26	0.36	13.25	1.65	0.08	0.32	1.47	3.66	3.74	0.29	100.00	5.00
OldCrow_013	75.00	0.30	13.18	1.70	0.10	0.29	1.50	3.86	3.83	0.31	100.00	4.14
OldCrow_014	75.44	0.34	13.08	1.76	0.02	0.25	1.44	3.61	3.85	0.28	100.00	4.81

OldCrow_015	75.21	0.27	13.11	1.79	0.06	0.35	1.50	3.64	3.83	0.30	100.00	4.50
OldCrow_016	75.48	0.35	13.00	1.75	0.04	0.29	1.46	3.64	3.78	0.28	100.00	3.93
OldCrow_017	75.43	0.36	13.10	1.73	0.06	0.24	1.42	3.54	3.86	0.32	100.00	2.13
OldCrow_018	74.71	0.26	13.25	1.69	0.05	0.26	1.40	4.36	3.79	0.31	100.00	3.54
OldCrow_019	75.28	0.35	13.19	1.66	0.09	0.31	1.45	3.65	3.82	0.27	100.00	3.38
OldCrow_020	74.58	0.30	13.03	1.70	0.07	0.31	1.49	4.38	3.91	0.30	100.00	4.66
OldCrow_021	75.37	0.34	13.11	1.73	0.10	0.22	1.43	3.84	3.70	0.22	100.00	4.22
OldCrow_022	75.35	0.28	13.11	1.78	0.07	0.28	1.40	3.69	3.85	0.24	100.00	5.07
Mean	75.24	0.31	13.09	1.71	0.07	0.28	1.44	3.86	3.78	0.28	100.00	3.70
StDev	0.28	0.04	0.11	0.05	0.03	0.03	0.04	0.30	0.09	0.03	0.00	1.39
Old Crow	**75.15**	**0.31**	**13.14**	**1.70**	**0.05**	**0.29**	**1.48**	**3.84**	**3.72**	**0.28**	**100.00**	**4.12**
assayed	1.00	0.05	0.34	0.14	0.03	0.03	0.05	0.26	0.26	0.05	-	-

Note: All data are normalized to 100%. XXX. All data are in wt% unless otherwise noted.

[a] FeOt - Total Fe as FeO.

[b] H_2Od - water content by difference (100 - analytical total).

Table B.5 Major-element Glass Analysis for UA3134 (40-2-110)

Sample name	SiO_2	TiO_2	Al_2O_3	FeOt [a]	MnO	MgO	CaO	Na_2O	K_2O	Cl	Total (%)	H_2Od [b] (%)	Comment
<u>UA3134 (40-2-110)</u>													
UA3134_025	73.10	0.48	14.32	2.77	0.10	0.44	1.82	4.06	2.82	0.13	100.00	6.99	-
UA3134_021	73.50	0.35	14.06	2.57	0.11	0.40	1.73	3.91	3.27	0.14	100.00	7.09	-
UA3134_028	73.53	0.45	14.07	2.69	0.12	0.42	1.85	3.35	3.39	0.17	100.00	7.77	-
UA3134_029	73.58	0.35	13.88	2.60	0.10	0.37	1.71	4.20	3.08	0.17	100.00	7.17	-
UA3134_030	73.63	0.43	14.04	2.48	0.09	0.39	1.74	4.28	2.80	0.15	100.00	7.43	-
UA3134_002	73.65	0.43	13.87	2.63	0.08	0.37	1.80	3.27	3.77	0.18	100.00	8.40	-
UA3134_019	73.83	0.45	13.92	2.65	0.11	0.38	1.71	3.80	3.03	0.18	100.00	6.97	-
UA3134_006	73.84	0.41	14.09	2.59	0.07	0.40	1.69	3.93	2.88	0.14	100.00	7.38	-
UA3134_020	73.87	0.40	13.96	2.53	0.11	0.36	1.80	3.19	3.64	0.18	100.00	7.64	-
UA3134_015	73.92	0.48	13.94	2.62	0.10	0.42	1.72	3.51	3.16	0.15	100.00	7.56	-
UA3134_024	73.94	0.36	13.97	2.72	0.13	0.44	1.79	2.59	3.94	0.15	100.00	8.34	-
UA3134_022	73.94	0.44	14.13	2.63	0.09	0.38	1.73	3.08	3.47	0.14	100.00	7.01	-
UA3134_014	74.01	0.40	13.98	2.65	0.07	0.40	1.71	3.49	3.21	0.12	100.00	6.61	-
UA3134_009	74.03	0.43	13.96	2.63	0.11	0.40	1.67	2.81	3.80	0.18	100.00	7.36	-
UA3134_003	74.13	0.46	14.06	2.76	0.09	0.41	1.77	1.68	4.52	0.17	100.00	9.15	-
UA3134_012	74.23	0.44	14.10	2.65	0.12	0.40	1.81	2.53	3.59	0.17	100.00	8.25	-
UA3134_027	74.27	0.43	13.81	2.68	0.08	0.39	1.82	2.05	4.36	0.14	100.00	8.15	-
UA3134_017	74.29	0.37	13.98	2.64	0.13	0.38	1.71	2.68	3.71	0.15	100.00	7.95	-
UA3134_018	74.33	0.45	13.96	2.48	0.09	0.39	1.71	2.55	3.90	0.16	100.00	8.02	-
UA3134_016	74.36	0.39	13.92	2.63	0.12	0.44	1.68	3.24	3.13	0.13	100.00	7.29	-
UA3134_013	74.41	0.48	14.09	2.61	0.10	0.39	1.77	1.84	4.22	0.12	100.00	8.42	-
UA3134_026	74.42	0.46	13.78	2.58	0.10	0.38	1.76	2.29	4.10	0.16	100.00	8.04	-
UA3134_001	74.43	0.44	13.84	2.47	0.11	0.42	1.82	2.31	4.04	0.16	100.00	8.55	-
UA3134_005	74.45	0.49	13.90	2.67	0.13	0.44	1.89	1.95	3.99	0.12	100.00	8.91	-
UA3134_023	74.49	0.42	13.79	2.71	0.10	0.37	1.72	2.31	4.00	0.13	100.00	8.04	-
UA3134_011	74.54	0.40	13.90	2.47	0.13	0.40	1.54	1.77	4.66	0.24	100.00	15.81	-
UA3134_008	74.54	0.49	13.78	2.63	0.10	0.41	1.68	1.75	4.47	0.19	100.00	11.03	-
UA3134_010	74.68	0.41	13.78	2.61	0.07	0.43	1.71	1.70	4.50	0.12	100.00	8.44	-
UA3134_007	74.89	0.47	13.82	2.78	0.07	0.41	1.80	1.66	3.94	0.22	100.00	13.23	-
UA3134_004	75.33	0.25	12.58	2.17	0.00	0.18	1.18	1.85	6.35	0.17	100.00	6.71	-
Mean	74.14	0.42	13.91	2.61	0.10	0.39	1.73	2.79	3.79	0.16	100.00	8.32	-
StDev	0.46	0.05	0.28	0.12	0.03	0.05	0.12	0.85	0.72	0.03	0.00	1.93	-

Note: All data are normalized to 100%. XXX. All data are in wt% unless otherwise noted.

[a] FeOt - Total Fe as FeO.

[b] H_2Od - water content by difference (100 - analytical total).

Table B.6 Major-element Glass Analysis for UA3135 (39-3-39)

Sample name	SiO_2	TiO_2	Al_2O_3	FeOt [a]	MnO	MgO	CaO	Na_2O	K_2O	Cl	Total (%)	H_2Od [b] (%)	Comment
UA3135 (39-3-39)													
UA3135_006	51.66	0.04	30.44	0.72	0.00	0.08	13.23	3.70	0.09	0.04	100.00	1.34	Plagioclase
UA3135_005	52.89	0.02	28.87	1.06	0.02	0.11	12.17	4.59	0.25	0.01	100.00	1.14	Plagioclase
UA3135_007	53.14	0.09	28.70	1.20	0.01	0.18	12.07	4.48	0.11	0.02	100.00	-0.04	Plagioclase
UA3135_004	54.92	0.10	27.62	1.04	0.00	0.13	10.93	5.01	0.26	0.01	100.00	0.90	Plagioclase
UA3135_001	72.86	0.62	15.62	2.81	0.13	0.73	1.81	0.84	4.45	0.18	100.00	15.16	-
UA3135_002	73.01	0.59	15.55	2.59	0.14	0.62	1.75	0.98	4.66	0.12	100.00	11.54	-
UA3135_009	73.42	0.64	15.50	2.54	0.15	0.62	1.72	0.66	4.62	0.15	100.00	11.94	-
UA3135_003	73.78	0.58	15.66	2.44	0.13	0.68	1.77	1.14	3.71	0.13	100.00	10.40	-
UA3135_015	73.80	0.63	15.67	2.56	0.17	0.63	1.74	1.82	2.89	0.13	100.00	11.01	-
UA3135_012	73.96	0.55	15.67	2.59	0.19	0.65	1.88	1.25	3.14	0.15	100.00	12.82	-
UA3135_008	74.05	0.63	15.66	2.52	0.09	0.68	1.72	1.19	3.34	0.15	100.00	10.78	-
UA3135_013	74.05	0.58	15.65	2.53	0.14	0.60	1.79	0.87	3.69	0.13	100.00	12.14	-
UA3135_014	74.67	0.47	15.37	2.27	0.16	0.53	1.58	1.87	2.99	0.12	100.00	10.80	-
UA3135_011	76.03	0.52	12.34	1.97	0.11	0.25	0.56	0.88	7.23	0.14	100.00	8.05	-
UA3135_010	76.41	0.52	12.74	2.06	0.09	0.27	0.61	0.96	6.23	0.14	100.00	8.72	-
Mean	74.19	0.57	15.04	2.44	0.14	0.57	1.54	1.13	4.27	0.14	100.00	11.22	-
StDev	1.13	0.05	1.24	0.25	0.03	0.16	0.48	0.39	1.39	0.02	0.00	1.92	-

Note: All data are normalized to 100%. XXX. All data are in wt% unless otherwise noted.

[a] FeOt - Total Fe as FeO.

[b] H_2Od - water content by difference (100 - analytical total).

Table B.7 Trace-element Glass Analysis for Standard Reference Glass Samples

Sample name	^{29}Si (cps)	^{43}Ca	^{44}Ca	^{47}Ti	^{49}Ti	^{69}Ga	^{71}Ga	^{85}Rb	^{88}Sr	^{89}Y	^{90}Zr	^{91}Zr	^{93}Nb	^{133}Cs	^{137}Ba	^{139}La
<u>NIST612 (primary standard reference material)</u>																
NIST612	1410000	85500	84500	13	36	36.7	37.9	31.7	78.5	38.4	37.0	37.8	39.0	42.3	37.8	35.9
NIST612_1	1400000	85700	85200	51	48	37.8	36.5	30.2	78.4	38.2	39.2	38.8	39.3	43.6	41.3	36.3
NIST612_2	1420000	84400	85300	49	39	36.0	36.5	32.6	77.4	38.1	38.0	35.5	39.0	42.1	38.9	35.6
NIST612_3	1370000	84700	85000	49	50	36.8	37.2	30.8	78.3	38.4	38.7	38.3	38.5	43.2	40.0	36.1
NIST612_4	1410000	86900	85100	25	40	37.0	37.3	32.5	78.6	38.8	37.9	36.7	39.0	43.3	41.0	36.5
NIST612_5	1390000	84500	85400	59	49	37.5	37.0	31.6	79.7	38.1	38.9	40.6	38.8	42.3	38.7	36.2
NIST612_6	1450000	83600	85100	51	43	36.1	36.3	32.0	77.5	38.4	37.3	37.8	38.8	42.1	37.9	35.1
NIST612_7	1410000	85200	84700	42	44	36.8	36.1	31.4	78.4	38.0	38.1	38.1	38.5	43.2	40.1	36.5
NIST612_8	1400000	86100	85100	36	42	37.4	38.1	30.5	77.8	38.4	37.7	36.2	39.8	42.1	38.4	35.5
<u>NIST610 and ATHo-G (secondary standard reference material)</u>																
NIST610	1470000	81200	81900	542	506	433.4	443.9	419.0	501.0	454.0	443.0	436.0	460.0	370.5	443.0	430.0
NIST610_1	1480000	77700	81800	554	506	431.8	437.1	410.6	502.0	454.0	441.0	423.0	456.5	373.8	446.0	429.0
NIST610_2	1470000	83400	82200	548	526	444.2	443.6	420.6	512.0	457.0	445.0	450.0	465.6	370.8	437.0	433.8
NIST610_3	1430000	81400	80800	538	531	435.1	443.5	416.7	502.0	451.3	431.3	442.0	462.7	367.6	455.0	437.0
NIST610_4	1480000	82000	80500	519	531	435.8	451.2	414.1	516.0	454.0	439.0	443.0	470.9	374.5	459.0	437.7
NIST610_5	1500000	83000	80900	506	496	432.7	449.8	411.4	510.7	453.0	435.2	429.0	462.8	369.9	455.0	431.5
NIST610_6	1460000	80400	81600	499	527	432.0	446.0	420.2	516.0	443.0	431.0	424.0	469.1	364.3	462.0	435.0
NIST610_7	1460000	82000	81800	469	550	432.5	446.7	425.1	517.0	441.0	435.0	422.0	471.7	360.9	456.0	435.9
NIST610_8	1450000	81500	81700	470	573	431.1	444.6	424.3	513.5	445.7	432.7	421.0	472.7	369.5	453.0	435.9
ATHO-G	1190000	11230	11480	1637	1554	36.4	24.4	63.3	88.2	87.6	467.0	448.0	55.3	1.1	509.0	52.1
ATHO-G_1	1190000	11340	11290	1629	1591	36.2	24.0	63.6	89.2	87.1	472.0	458.0	52.7	1.1	510.0	51.3
ATHO-G_2	1180000	11500	11370	1602	1572	34.9	22.4	62.2	88.4	85.0	460.0	469.0	52.4	0.9	506.0	52.4
ATHO-G_3	1180000	11140	11500	1632	1530	33.4	23.2	60.1	88.8	85.9	469.0	454.0	54.6	0.9	522.0	51.9
ATHO-G_4	1220000	11850	11110	1509	1570	36.3	21.0	60.8	87.3	84.3	458.0	461.0	53.3	0.9	515.0	50.2
ATHO-G_5	1170000	11800	11360	1502	1613	35.9	24.3	60.6	87.4	88.4	463.0	450.0	55.5	0.8	530.0	51.4
NIST610	1470000	81200	81900	542	506	433.4	443.9	419.0	501.0	454.0	443.0	436.0	460.0	370.5	443.0	430.0
NIST610_1	1480000	77700	81800	554	506	431.8	437.1	410.6	502.0	454.0	441.0	423.0	456.5	373.8	446.0	429.0
NIST610_2	1470000	83400	82200	548	526	444.2	443.6	420.6	512.0	457.0	445.0	450.0	465.6	370.8	437.0	433.8
NIST610_3	1430000	81400	80800	538	531	435.1	443.5	416.7	502.0	451.3	431.3	442.0	462.7	367.6	455.0	437.0
NIST610_4	1480000	82000	80500	519	531	435.8	451.2	414.1	516.0	454.0	439.0	443.0	470.9	374.5	459.0	437.7
NIST610_5	1500000	83000	80900	506	496	432.7	449.8	411.4	510.7	453.0	435.2	429.0	462.8	369.9	455.0	431.5
NIST610_6	1480000	81100	82100	497	536	432.2	447.9	421.0	521.0	454.0	436.0	427.0	471.0	365.3	464.0	440.0
NIST610_7	1460000	82000	81800	469	550	432.5	446.7	425.1	517.0	441.0	435.0	422.0	471.7	360.9	456.0	435.9
NIST610_8	1470000	81800	82400	470	568	431.6	446.0	424.4	515.9	451.0	437.2	425.0	474.4	370.1	457.0	440.0

Note: All data in ppm unless otherwise noted.

(Continued)

Sample name	^{140}Ce	^{141}Pr	^{146}Nd	^{147}Sm	^{153}Eu	^{157}Gd	^{159}Tb	^{163}Dy	^{165}Ho	^{166}Er	^{169}Tm	^{172}Yb	^{175}Lu	^{178}Hf	^{181}Ta	^{208}Pb	^{232}Th	^{238}U
NIST612 (primary standard reference material)																		
NIST612	38.6	38.4	36.0	37.6	35.1	37.6	37.7	35.4	38.2	38.0	36.3	39.7	37.0	35.7	37.5	38.2	37.7	37.1
NIST612_1	38.0	37.9	34.6	38.0	35.6	36.2	37.9	34.8	38.8	37.7	37.3	39.5	37.2	37.1	37.9	38.9	38.4	37.8
NIST612_2	38.6	37.6	36.0	37.3	35.6	37.9	36.5	34.9	37.6	37.9	36.5	38.9	36.5	36.2	37.1	38.2	37.2	37.2
NIST612_3	39.1	37.8	34.5	37.2	35.5	38.0	37.7	36.3	38.6	37.8	36.9	39.0	37.2	37.6	37.9	39.0	37.9	37.2
NIST612_4	39.7	38.3	36.2	37.8	36.8	37.7	38.7	36.9	38.0	38.5	37.7	37.9	37.5	37.2	37.5	38.9	38.1	37.7
NIST612_5	37.7	37.8	37.5	38.5	36.0	36.9	38.0	35.3	38.5	38.7	36.6	39.6	36.6	35.4	37.7	37.9	38.0	37.6
NIST612_6	38.5	37.8	33.2	36.6	35.4	38.8	37.5	34.5	38.4	37.6	36.9	40.3	37.4	36.8	37.3	38.4	37.8	37.4
NIST612_7	37.8	37.7	37.0	37.6	35.7	35.4	37.7	36.2	38.1	38.5	36.4	38.2	36.7	35.8	37.8	38.5	37.5	37.4
NIST612_8	38.4	38.6	35.1	38.2	35.0	38.5	36.7	34.2	38.4	36.9	36.5	39.7	37.0	37.2	37.6	38.8	37.9	37.2
NIST610 and ATHo-G (secondary standard reference material)																		
NIST610	451.0	449.0	428.0	453.0	447.4	438.0	439.0	419.0	452.0	452.0	424.0	444.0	442.0	421.0	451.0	417.5	455.0	450.5
NIST610_1	447.0	447.0	424.0	448.0	442.0	435.0	433.0	414.0	447.0	452.0	421.0	447.0	430.0	419.0	446.0	412.5	455.0	451.6
NIST610_2	448.2	446.7	434.0	446.0	447.0	444.0	435.0	425.0	447.0	451.0	424.0	453.0	435.0	422.0	446.2	413.9	452.0	449.4
NIST610_3	456.9	451.9	433.0	460.0	443.1	414.0	433.8	417.4	447.9	444.0	431.0	458.8	430.3	420.0	439.5	414.3	457.0	452.3
NIST610_4	458.0	448.0	443.0	467.0	446.9	422.0	440.0	429.0	452.0	433.0	425.0	456.0	436.0	436.0	442.3	420.5	461.0	452.5
NIST610_5	447.7	443.7	439.0	459.0	444.7	413.6	433.5	422.1	449.7	441.0	421.0	453.0	437.1	425.0	441.3	414.4	453.0	448.4
NIST610_6	447.0	445.0	429.0	453.0	438.0	426.0	431.0	418.0	445.0	440.0	427.0	451.0	432.0	423.0	447.3	418.3	447.0	447.4
NIST610_7	445.8	450.1	428.0	451.0	434.0	437.0	434.0	420.0	442.0	444.0	425.0	456.0	433.5	425.5	446.0	419.4	437.8	452.8
NIST610_8	451.1	444.2	427.0	442.0	442.3	445.0	435.0	421.4	445.3	446.2	422.0	457.4	436.0	434.0	441.7	426.9	447.3	454.5
ATHO-G	113.9	14.1	55.2	13.6	2.7	13.8	2.2	14.2	3.3	9.8	1.5	9.9	1.5	12.2	3.5	5.3	6.7	2.2
ATHO-G_1	114.0	14.4	58.5	14.6	2.6	14.1	2.2	15.2	3.2	9.3	1.4	9.7	1.5	13.3	3.2	4.5	6.8	2.3
ATHO-G_2	111.9	14.3	56.3	13.8	2.5	13.2	2.6	14.5	3.2	9.5	1.3	10.4	1.4	13.0	3.3	5.2	6.9	2.1
ATHO-G_3	113.5	13.9	57.3	12.8	2.7	13.5	2.4	15.1	3.3	9.8	1.4	10.1	1.5	13.1	3.0	5.1	7.0	2.1
ATHO-G_4	112.7	13.3	55.6	14.3	2.4	13.0	2.3	15.0	3.2	8.9	1.5	9.6	1.3	12.7	3.2	4.8	6.7	2.1
ATHO-G_5	113.3	13.3	57.3	13.7	2.8	12.0	2.3	16.2	3.4	9.1	1.4	10.2	1.4	12.8	3.2	5.2	7.0	2.2
NIST610	451.0	449.0	428.0	453.0	447.4	438.0	439.0	419.0	452.0	452.0	424.0	444.0	442.0	421.0	451.0	417.5	455.0	450.5
NIST610_1	447.0	447.0	424.0	448.0	442.0	435.0	433.0	414.0	447.0	452.0	421.0	447.0	430.0	419.0	446.0	412.5	455.0	451.6
NIST610_2	448.2	446.7	434.0	446.0	447.0	444.0	435.0	425.0	447.0	451.0	424.0	453.0	435.0	422.0	446.2	413.9	452.0	449.4
NIST610_3	456.9	451.9	433.0	460.0	443.1	414.0	433.8	417.4	447.9	444.0	431.0	458.8	430.3	420.0	439.5	414.3	457.0	452.3
NIST610_4	458.0	448.0	443.0	467.0	446.9	422.0	440.0	429.0	452.0	433.0	425.0	456.0	436.0	436.0	442.3	420.5	461.0	452.5
NIST610_5	447.7	443.7	439.0	459.0	444.7	413.6	433.5	422.1	449.7	441.0	421.0	453.0	437.1	425.0	441.3	414.4	453.0	448.4
NIST610_6	452.0	450.0	435.0	459.0	444.0	428.0	437.0	425.0	452.0	447.0	432.0	459.0	440.0	430.0	449.0	416.2	448.0	454.0
NIST610_7	445.8	450.1	428.0	451.0	434.0	437.0	434.0	420.0	442.0	444.0	425.0	456.0	433.5	425.5	446.0	419.4	437.8	452.8
NIST610_8	452.5	447.7	431.0	446.0	447.0	452.0	440.0	427.0	446.9	451.0	427.0	458.2	439.0	438.0	444.9	428.2	449.8	455.5

Note: All data in ppm unless otherwise noted.

Table B.8 Trace-element Glass Analysis for UA3134 (40-2-110) and UA3135 (39-3-39)

Sample name	^{29}Si (cps)	^{43}Ca	^{44}Ca	^{47}Ti	^{49}Ti	^{69}Ga	^{71}Ga	^{85}Rb	^{88}Sr	^{89}Y	^{90}Zr	^{91}Zr	^{93}Nb	^{133}Cs	^{137}Ba	^{139}La	^{140}Ce
UA3134 (40-2-110)																	
UA3134	880000	7570	8690	1215	1245	42.6	11.2	93.6	103.0	23.2	127.5	130.5	4.4	8.1	1055.0	13.7	27.3
UA3134_1	740000	9100	8700	1202	1170	44.0	11.1	91.2	109.0	23.6	125.0	116.0	3.8	8.6	1035.0	14.1	27.3
UA3134_2	1010000	8660	9110	1189	1311	42.0	12.1	93.0	109.1	22.3	130.0	132.6	3.8	7.9	1074.0	13.8	28.6
UA3134_3	890000	9000	8690	1191	1327	44.0	13.2	94.3	103.9	21.7	121.8	123.0	3.3	8.1	1075.0	13.3	26.2
UA3134_4	997000	8220	9410	1103	1199	42.2	11.3	91.5	106.9	23.1	127.4	129.9	3.7	7.9	1044.0	13.7	27.7
UA3134_6	870000	10400	8770	1250	1350	46.9	12.0	96.3	110.9	21.0	124.0	121.0	3.6	7.9	1010.0	12.8	27.8
UA3134_7	1120000	8650	8920	1116	1163	41.8	11.7	88.5	105.6	22.5	127.8	128.1	3.2	7.6	1024.0	14.2	27.8
UA3134_8	855000	9140	8830	1166	1237	43.5	10.7	95.2	107.0	22.8	127.1	126.1	3.8	8.0	1077.0	14.3	28.1
UA3134_9	965000	10100	8990	1187	1286	43.0	12.8	92.9	106.7	22.8	121.9	121.6	3.8	7.9	1040.0	14.1	27.1
Mean	925222	8982	8901	1180	1254	43.3	11.8	92.9	106.9	22.6	125.8	125.4	3.7	8.0	1048.2	13.8	27.5
StDev	110359	872	240	46	69	1.6	0.8	2.3	2.5	0.8	2.8	5.4	0.4	0.3	23.9	0.5	0.7
UA3135 (39-3-39)																	
UA3135	905000	9420	8500	1439	1540	43.3	13.1	101.6	107.0	21.7	127.9	119.3	4.4	8.5	1005.0	14.9	29.5
UA3135_3	981000	9160	8730	1095	1197	42.6	12.0	89.0	108.1	22.8	123.7	127.3	3.4	7.6	1034.0	14.2	27.2
UA3135_4	870000	9330	9230	1171	1243	44.4	11.3	94.5	112.2	23.8	132.0	131.5	3.9	8.5	1092.0	14.7	28.3
UA3135_6	830000	10400	8790	1260	1320	44.8	11.8	94.8	109.5	23.5	127.7	128.8	3.7	8.4	1036.0	15.4	27.3
Mean	896500	9578	8813	1241	1325	43.8	12.1	95.0	109.2	23.0	127.8	126.7	3.8	8.2	1041.8	14.8	28.1
StDev	64127	559	305	148	152	1.0	0.8	5.2	2.2	0.9	3.4	5.2	0.4	0.4	36.4	0.5	1.1

Note: All data in ppm unless otherwise noted.

(Continued)

Sample name	^{141}Pr	^{146}Nd	^{147}Sm	^{153}Eu	^{157}Gd	^{159}Tb	^{163}Dy	^{165}Ho	^{166}Er	^{169}Tm	^{172}Yb	^{175}Lu	^{178}Hf	^{181}Ta	^{208}Pb	^{232}Th	^{238}U
UA3134 (40-2-110)																	
UA3134	2.8	11.8	2.9	0.6	3.2	0.5	2.9	0.8	2.2	0.4	2.1	0.5	3.7	0.3	21.6	6.8	2.3
UA3134_1	3.5	10.6	3.3	0.6	1.7	0.5	3.7	0.9	2.4	0.4	2.2	0.4	3.2	0.4	20.9	6.3	2.0
UA3134_2	3.1	13.1	3.1	0.4	2.8	0.6	3.0	0.9	2.8	0.4	2.9	0.4	3.4	0.4	22.3	6.6	2.3
UA3134_3	3.1	9.7	4.0	0.5	1.8	0.7	3.6	0.7	2.7	0.5	3.3	0.4	4.4	0.3	21.5	6.4	2.3
UA3134_4	2.9	12.7	2.8	0.6	2.6	0.5	2.7	1.0	2.5	0.4	2.8	0.5	3.8	0.2	21.5	6.5	2.2
UA3134_6	3.4	10.8	2.8	0.6	2.3	0.3	2.8	0.7	2.2	0.3	3.3	0.5	3.6	0.3	19.0	6.6	1.9
UA3134_7	3.2	11.7	3.3	0.6	2.9	0.5	4.0	0.9	2.5	0.5	2.8	0.6	3.3	0.3	22.8	7.0	2.2
UA3134_8	3.3	11.5	2.4	0.5	2.6	0.5	3.4	0.8	2.4	0.5	3.0	0.5	3.4	0.3	22.0	6.5	2.2
UA3134_9	2.9	11.8	2.5	0.6	2.8	0.6	3.6	0.8	2.4	0.4	3.7	0.4	3.5	0.4	21.8	6.6	2.3
Mean	3.1	11.5	3.0	0.6	2.5	0.5	3.3	0.8	2.4	0.4	2.9	0.5	3.6	0.3	21.5	6.6	2.2
StDev	0.2	1.0	0.5	0.1	0.5	0.1	0.5	0.1	0.2	0.1	0.5	0.1	0.4	0.1	1.1	0.2	0.2
UA3135 (39-3-39)																	
UA3135	3.2	13.1	3.1	0.7	2.3	0.6	3.8	0.8	2.9	0.4	3.0	0.4	4.0	0.2	21.3	7.0	2.3
UA3135_3	3.0	12.7	3.5	0.6	2.5	0.5	3.8	0.7	2.7	0.4	2.7	0.4	4.0	0.3	21.2	6.6	2.1
UA3135_4	3.3	13.1	2.3	0.6	2.7	0.5	4.1	0.9	2.7	0.3	2.6	0.5	4.0	0.2	22.2	7.0	2.0
UA3135_6	3.0	11.7	2.4	0.7	1.6	0.5	3.7	0.8	2.6	0.3	2.6	0.4	3.3	0.2	20.2	6.9	2.2
Mean	3.1	12.7	2.8	0.6	2.3	0.5	3.8	0.8	2.7	0.4	2.7	0.4	3.8	0.2	21.2	6.9	2.2
StDev	0.1	0.7	0.6	0.0	0.5	0.0	0.2	0.1	0.1	0.1	0.2	0.1	0.3	0.0	0.8	0.2	0.1

Note: All data in ppm unless otherwise noted.

Table B.9 δ^{13}C, atomic C_{org}:N_{tot}, C_{org} and N_{tot} Analysis for the Wombat Samples

Sample number	Depth (m)	Core	C_{org}[a] (wt%)	N_{tot}[b] (wt%)	C_{org}:N_{tot}[c] (atomic)	δ^{13}C (‰ vs. PDB)	2σ (‰ vs. PDB)
6-3-17	66.4	DDH 00-05	3.3	0.15	25.3	-26.0	0.2
7-1-24	67.7	DDH 00-05	4.1	0.17	28.9	-26.1	0.2
9-1-26	81.6	DDH 00-05	3.5	0.16	24.8	-27.5	0.2
10-3-79	95.4	DDH 00-05	4.4	0.22	23.4	-25.7	0.3
11-2-85	101.3	DDH 00-05	2.2	0.16	16.6	-25.3	0.4
12-3-55	107.6	DDH 00-05	3.2	0.14	26.6	-25.9	0.3
13-3-35	113.6	DDH 00-05	2.6	0.19	15.7	-25.9	0.3
15-4-13	125.0	DDH 00-05	2.4	0.14	20.1	-26.1	0.2
44-1-12	128.6	CH93-29	8.8	0.27	38.4	-28.3	0.4
16-2-140	131.1	DDH 00-05	1.7	0.14	14.6	-25.6	0.3
17-3-10	135.0	DDH 00-05	3.0	0.15	23.1	-25.8	0.3
18-2-30	138.3	DDH 00-05	4.3	0.15	33.0	-26.3	0.3
45-1-95	138.6	CH93-29	2.8	0.16	20.8	-27.0	0.4
19-1-2	140.9	DDH 00-05	3.3	0.16	23.4	-26.4	0.4
20-1-54	144.9	DDH 00-05	4.2	0.19	26.0	-26.0	0.4
47-2-16	149.9	CH93-29	4.1	0.17	28.9	-26.8	0.2
48-1-60	153.5	CH93-29	2.3	0.14	19.8	-26.5	0.2
21-1-90	152.5	DDH 00-05	1.9	0.15	15.2	-26.0	0.2
49-1-73	157.6	CH93-29	5.4	0.19	32.5	-27.4	0.2
23-3-5	161.8	DDH 00-05	1.5	0.11	16.6	-26.0	0.2
50-2-73	163.2	CH93-29	7.7	0.25	35.1	-27.4	0.2
24-3-3	168.1	DDH 00-05	3.4	0.19	20.6	-25.8	0.2
52-1-147	172.7	CH93-29	1.9	0.14	16.1	-26.0	0.3
26-3-75	178.8	DDH 00-05	5.1	0.20	30.2	-27.7	0.3
54-3-8	182.7	CH93-29	2.6	0.15	20.2	-25.8	0.2
56-1-46	190.1	CH93-29	2.9	0.13	25.6	-26.0	0.3
57-2-140	196.2	CH93-29	2.5	0.17	17.5	-26.2	0.3
30-2-44	197.2	DDH 00-05	2.3	0.14	19.3	-26.2	0.3
31-1-45	200.0	DDH 00-05	2.8	0.17	19.4	-25.9	0.2
33-1-30	206.5	DDH 00-05	3.6	0.19	22.2	-26.1	0.2
60-1-125	207.1	CH93-29	2.6	0.15	19.3	-26.3	0.2
61-3-108	214.5	CH93-29	2.0	0.16	15.2	-26.5	0.2
35-3-77	218.3	DDH 00-05	1.5	0.11	16.2	-25.8	0.3
62-4-120	219.9	CH93-29	4.5	0.20	26.6	-27.6	0.3
63-2-142	222.4	CH93-29	8.1	0.25	37.3	-27.1	0.2
64-2-17_18	227.9	CH93-29	4.8	0.21	26.6	-28.4	0.2
38-1-21	226.9	DDH 00-05	3.4	0.16	24.1	-26.6	0.3
64-4-70	230.4	CH93-29	5.4	0.19	32.9	-28.8	0.2
65-1-15	233.7	CH93-29	6.2	0.22	32.9	-28.9	0.2
40-1-60	234.4	DDH 00-05	5.8	0.22	30.5	-27.4	0.2
66-1-80	238.0	CH93-29	6.1	0.25	28.3	-30.2	0.2
66-3-43	239.9	CH93-29	2.7	0.14	23.2	-26.0	0.2
67-2-88_90	246.0	CH93-29	1.4	N.D.	N.D.	-26.5	0.3
67-4-64	248.0	CH93-29	1.1	N.D.	N.D.	-26.7	0.2

[a] Organic carbon content.

[b] Total nitrogen content.

[c] C_{org} and N_{tot} atomic weight ratio.

Table B.10 The Rock Eval II and LECO Results for The Wombat Samples

Sample number	Depth (m)	Core	S_1 (mg HC/g)	S_2 (mg HC/g)	S_3 (mg CO_2/g)	C_{org} [a] (wt%)	C_{inorg} [b] (wt%)	HI [c] (mg HC/g C_{org})	*Tmax* [d] (°C)
6-3-17	66.4	DDH 00-05	0.18	1.06	1.29	2.3	5.6	47.1	430
9-1-26	81.6	DDH 00-05	0.28	1.75	1.46	2.9	5.8	59.9	426
11-2-85	101.3	DDH 00-05	0.18	0.70	1.05	1.8	5.9	38.9	432
13-3-35	113.6	DDH 00-05	0.19	0.89	1.48	1.8	8.2	50.6	427
15-4-13	125.0	DDH 00-05	0.30	1.89	1.60	2.9	9.4	65.6	427
44-1-126*	128.6	CH93-29	1.47	16.46	5.32	9.6	18.0	172.0	424
44-1-126	128.6	CH93-29	1.23	19.15	6.36	10.3	11.1	185.9	429
47-2-11	149.9	CH93-29	0.22	1.40	1.68	2.2	6.0	62.8	431
52-1-147	172.7	CH93-29	0.14	1.25	1.87	2.4	7.8	51.9	427
57-2-140	196.2	CH93-29	0.39	3.38	2.32	3.6	5.3	92.9	427
60-1-125	207.1	CH93-29	0.11	0.98	3.29	2.1	13.1	46.0	430
61-3-108	214.5	CH93-29	0.12	0.67	1.41	1.7	6.5	39.2	430
62-2-102	217.7	CH93-29	0.28	2.05	7.54	2.5	23.1	80.7	426
62-4-120	219.9	CH93-29	0.28	2.73	4.52	5.2	12.8	53.0	428
63-2-31	221.6	CH93-29	0.21	0.97	6.77	5.4	22.7	18.1	411
64-2-17_18	227.9	CH93-29	0.41	7.57	5.83	6.5	16.6	116.5	415
65-1-15*	233.7	CH93-29	0.41	5.06	3.53	4.7	20.5	108.6	417
65-1-15	233.7	CH93-29	0.23	2.32	5.63	4.3	22.8	53.6	419
66-1-80	238.0	CH93-29	0.46	1.83	4.35	5.7	39.1	32.0	402
67-2-88_90	246.0	CH93-29	0.05	0.13	0.54	0.9	31.2	14.3	N.D.

[a] Organic carbon content.

[b] Inorganic carbon content.

[c] HI, hydrogen index.

[d] T_{max}, temperature of maximum pyrolysis yield.

* Duplicate analysis

Table B.11 The Wombat Drill Core Description for DDH 00-05

Depth (VE, m)	Lithology Description	Structures Descrition	Inclusion Description	Fossils Description	Comments
55.4 - 58.9	Biotite, Muscovite Granite	Massive	N/A	N/A	Good preservation.
58.9 - 104.5	Borwnish-grey silty mudstone.	Massive with local fine lamiation 1-3 mm. Small scale falttened clay lenses.	Siderite and vivianite 1-5 mm. Oxidized inclusions of pyrite? Counry rock fragments	Fine carbonized wood and plant fragments	Poor preservation .
104.5 - 155.3	Light grey silty mudstone with intervals of muddy mudstone. In places mudstone becomes siltier upward. Friable texture.	Locally uniform and massive, with alterations of dark and light laminae on a mm-scale. Local cm-scale bedding.	Oxidized nodules mm-scale.	Carbonized woody fragments.	Locally poor preservation.
155.3 - 173.4	Light grey silty mudstone to muddy siltstone.	Uniform mm- to cm-scale laminations.	Oxidized nodules mm-scale.	N/A	Locally poor preservation.
173.4 - 231.0	Very uniform, consolidated, light brownish - grey silty mudstone. Friable texture dominant. 173.4 - 173.9 m heterogenous section of massive, dark - grey mudstone with abundant clay, country rock clasts.	Uniform mm- to cm-scale laminations, with alterations of dark and light laminae. Local occurences of contorted lamination and convolute bedding.	Vivianite and siderite nodules mm-scale. Country rock fragments.	Very fine carbonized woody fragments, plant detritus.	Good preservation.
231.0 - 248.1	Light grey to dark brown muddy siltstone. Heterogenous sections with abundant plant fragments, diopside, garnet and country rock fragments. Common oxidation surfaces. Two light grey tephra layers identified at 233.9 m and 236.8 m respectively. Bentonite layer at 232.1 m.	Uniform mm- to cm-scale laminations, with alterations of dark and light laminae. Local occurences of contorted lamination.	Siderite nodules mm-scale. Country rock fragments.	Leaf fossils and abundant carbonized wood fragments. Fully articulated fish fossil recovered at 237.5 m.	Good preservation, lower most section is missing. Strong reaction to HCl.

Table B.12 The Wombat Drill Core Description for CH93-29

Depth (VE, m)	Lithology Description	Structures Descrition	Inclusion Description	Fossils Description	Comments
156.8 - 161.0	Biotite, Muscovite Granite	Massive	N/A	N/A	Good preservation.
161.0 - 178.2	Dark grey silty mudstone. Friable texture	Mostly massive with local fine lamiations 1-5 mm. Contorted laminations present locally. Small scale falttened clay lenses.	N/A	N/A	Good preservation.
178.2 - 191.8	Light grey to dark brown silty mudstone. Abundant sedimentary rock clasts in heterogenous sections.	Mostly mm- to cm-scale laminations with local massive regions. Contorted laminations and overloading structures are present. Abundant clay lenses and deformed mudstone clasts.	N/A	Carbonized plant detritus mm-scale.	Good preservation.
191.8 - 221.0	Light grey brownish grey silty mudstone, mostly well consolidated. Locally oxidized surfaces.	Uniform mm- to cm-scale laminations, with alterations of dark and light laminae. Contorted laminations and water escape structures. Potential turbidite layer at 216.0 m.	Oxidized nodules mm-scale.	Carbonized plant detritus mm-scale.	Good preservation.
221.0 - 224.3	Dark Grey mudstone. Mostly unconsolidated. Friable texture.	Mostly massive, homogeneous and without clear structures. Locally preserved mm-scale laminations.	N/A	N/A	Poor preservation. Poor core recovery?
224.3 - 245.0	Light grey to dark brown muddy siltstone. Friable texture. Some oxidation surfaces.	Uniform mm- to cm-scale laminations, with alterations of dark and light laminae.	N/A	Carbonized woody material. Fully articualted fish fossil recovered at 242.7 m.	Good preservation.
245.0 - 277.4	Grey mudstone and greenish-gold muddy siltstone. Surfical oxidation is common. Heaviliy altered tephra layer recovered at 264.1 m and 267.5 m.	mm-scale laminations commonly contorted. Brecciated regions. Possible overloading structures.	Carbonate nodules in the heavily oxidzed regions. Minor kimberlitic component present.	Carbonized woody fragments and plant detritus.	Good preservation. Moderate reaction with HCl.